Synthesis and tribocorrosion study of tungsten nitride thin films

Tania Berenice Garcia Ramos

To cite this version:

Tania Berenice Garcia Ramos. Synthesis and tribocorrosion study of tungsten nitride thin films. Condensed Matter [cond-mat]. Université de Picardie Jules Verne, 2021. English. NNT : 2021AMIE0061 . tel-03881113

HAL Id: tel-03881113
https://theses.hal.science/tel-03881113

Submitted on 1 Dec 2022

Thèse de Doctorat

Mention Physique
Spécialité Physique Matière Condensée

présentée à ***l'Ecole Doctorale en Sciences, Technologie et Sante***

de l'Université de Picardie Jules Verne

par

Tania Berenice GARCIA RAMOS

pour obtenir le grade de Docteur de l'Université de Picardie Jules Verne

Elaboration et évaluation par tribocorrosion de couches minces de nitride de tungstène

Soutenue le 14 septembre 2021, après avis des rapporteurs, devant le jury d'examen :

M. Maxence Bigerelle. Professeur des Universités, UPHF	**Rapporteur**
M. Ivan Campos, Professeur des Universités, ESIME-IPN	**Rapporteur**
M^{me} Claire Meyer, Maître de Conférences HDR, UPJV	**Examinatrice**
M. Laurent Lahoche, Professeur des Universités, IUT-UPJV,	**Président du jury**
M. A. Zeinert, Professeur des Universités, UPJV	**Directeur de thèse**
M. S. Muhl, Professeur des Universités, UNAM	**Co-encadrant**

CONACYT

LPMC
Laboratoire de Physique
de la Matière Condensée

Acknowledgements

Countless people supported me on this journey and this project would not have been possible without them.

I would first like to thank my supervisors, Andreas Zeinert and Stephen Muhl, for their valuable guidance. Your insightful feedback pushed me to sharpen my thinking and brought my work to a successful end.

I acknowledge the generous financial support from the 'Consejo Nacional de Ciencia y Tecnología' through their international funding system (270930/439637) and PAPIIT through the project IG 101220.

Professors Maxence Bigerelle and Iván Campos for accepting to judge the present work and the invaluable feedback provided. Also, thanks to my jury members for the time and kind words. To my committee members, Pierre Ponthiaux and Nathalie Lemée, who offered guidance and support, thank you for everything.

My gratitude and acknowledgement to everyone from IIM– UNAM, LPMC - UPJV, LRCS-UPJV and IUTA-UPJV that somehow helped to the successful development of this project.

It is hard to find words to express my gratitude to Alejandro, Dali, Daniela, Diego, Mariem, … for all the support, time, and love. You are the best!

Lastly, my family deserves endless gratitude: my parents and siblings that were with me every step of the way ¡Gracias, los amo! My extended family for being so caring and helping me. Eddy, thank you for everything!

after 1802 days I can say…

Bada Bing, Bada bang, Bada boom!

Contents

List of Figures

List of Tables

Introduction

This text presents the comprehensive result of my Ph.D. research. This project deals with the various factors that can influence the tribocorrosion process and how to reduce the surface damage produced by the combined effect of mechanical wear and corrosion. A wide variety of sectors from industry, transportation, construction, and even health, can be affected by tribocorrosion. The produced damage diminishes the lifetime of mechanical systems which can lead to major security problems and economical losses. For the purpose of this work materials used for the construction of food processing machines were studied. Moreover, a protective thin film was proposed and its tribocorrosion process was studied.

The experimental work was performed at the "Laboratoire de Physique de la Matière Condensée" (LPMC) from the "Université de Picardie Jules Verne" (UPJV) and the "Instituto de Investigaciones en Materiales" (IIM) at the "Universidad Nacional Autónoma de México" (UNAM).

The manuscript is divided in an introduction and six chapters.

Chapter 1 presents the state of the art in tribocorrosion along with the description of different experimental methods applied in this research.

Chapter 2 presents the apparatus utilized for the tribocorrosion study and the thin film obtention, along with a detailed description of the changes and adaptations carried out. Such adaptations were needed for specific tasks in this project.

A comprehensive study of the substrates is presented in Chapter 3. The mechanical and corrosive behavior of both AISI D2 steel and AISI 431 steel are presented. The combined effect of corrosion and mechanical wear was explored in order to establish the performance of each steel under the desired conditions. The performed tests were carried out in view of the tribocorrosion characterization.

The thin films synthesis by rf magnetron sputtering and the characterization of the obtained thin films are presented in chapter 4. The mechanical, corrosion and tribocorrosion behavior of the thin films are reported in chapter 5.

Finally, chapter 6 presents the general conclusions and perspectives of this work.

Food Industry and construction materials

During the last decades, the food industry has changed and grown along with the consumer markets, this evolution has produced development in the wide range of steps that comprise the process from preparation to packing and shipping food [Heldman 2013; Shan 2016; Moore 2017; Moerman and Partington 2014].

In general, the materials that are used for the manufacture of the machines employed in this process are not controlled by the standards and guidelines created by the worldwide legislative and standardization bodies. Nevertheless, such materials are regularly selected to prevent the contamination of food by microorganisms, dirt, and chemical substances. However, the materials must be durable and mechanically stable, easy to machine, compatible with other materials used for the construction, chemically resistant and temperature resistant (hot and/or cold)[Moerman and Partington 2014].

Due to this large number of requirements, to select the best materials of construction the manufacturers must know about the physical, chemical and thermal behavior, and at the same time, they must respond to laws, regulations, standards, and applicable guidelines. In the European Union, the legislation is given by the European Commission Regulation (EC), the general regulation is the EC No. 1935/2004 for materials intended to be in contact with food, but there are specific regulations for specific types of materials[Ekaterina Karamfilova 2016]. The materials used for food processing equipment can be classified as metals and alloys, plastics, elastomers, composites, films, and others such as glass, ceramics, wood, etc.[Aguilera and Lillford 2008; Moerman and Partington 2014]. In the present work, the interest is focused on metals and thin films.

The current European regulation, the "Resolution CM/Res(2013) on metals and alloys used in food contact materials", recommends the use of aluminum, chromium, copper, gold, iron, manganese, magnesium, molybdenum, nickel, platinum, silicon, silver, titanium, zinc, cobalt, vanadium and carbon. The most common metallic alloys used in the food industry, are cast iron, steel (mild, galvanized, and stainless), nickel, copper (brass and bronze), and titanium alloys.

Since these materials can be exposed to extreme conditions where they are supposed to perform well for an extended lifetime, some improvements, such as surface thin films, have been developed. The desired properties of a thin film depend on the specific application, but in a broad sense of this work, thin films are intended to protect the equipment from an aggressive environment, reduce friction between two surfaces in contact and improve the chemical, and mechanical properties of the coated surface.

According to the European legislation, the general principles of regulation which need to be respected are: ‘thin films, if used, shall be free from surface delamination, pitting, flaking, spalling, blistering and distortion when exposed to the conditions encountered in the environment of intended use, and to cleaning, bactericidal treatment or sterilization’[Moerman and Partington 2014].

Among the different options, ceramic coatings are resistant to temperature, abrasion, high-temperature corrosion, and erosion-corrosion resistant. To use them as construction materials for food machinery they must be[Moerman and Partington 2014]:

- Inert.
- Nonporous and non-absorbent.
- Smooth, unbroken surfaces, entirely free of crazing, i.e., small hairline cracks
- Resistant to scratching, scoring, and distortion when exposed to the conditions encountered in the environment of intended use
- Nontoxic, free of leachable lead, cadmium, and other potentially toxic heavy metals.

Canned food systems

Canning was invented in France in 1810 as a way to preserve food at room temperature for the military, originally the containers were corked glass, handmade canisters[Yam 2009]. This invention has evolved to become a common way to preserve food within a multi-billionaire industry. For example, since the 1980s, more than 45 million tons of canned food have been produced, of which more than half are tinned fruits and vegetables[Shan 2016]. Only in the U.S. canned food represented a business of 15.8 billion dollars in 2016 [Grand View Research 2018].

During the canning process, different machines and equipment are used. The common sequence of the full canning process is, first, to prepare the product to be canned, then to fill and seal the containers (cans) and finally to sterilize them, regularly by pasteurization.

During the hermetically sealing step, there are two key points to consider. One is that a proper vacuum must be achieved so that the container is sealed while the food is near or at boiling point. The most common method of producing an internal vacuum is by displacing the air in the can with steam [Yam 2009]. The other key point is to guarantee the correct closure of the can since this will assure a long shelf life and prevent microbiological spoilage. This step is made using a seaming machine[Featherstone and Featherstone 2015; Shan 2016] composed of pressure heads (to prevent cans from shifting while they are being sealed), trays (to transport the cans), chucks, and rolls (round-shaped pieces to fold and seam the cans)[Yam 2009; Shan 2016].

Figure 1 shows an illustration of the seaming system based on chucks and rolls for closing cans. In it, one can see how the chuck will keep the can lid in position while the chuck presses the lid to the can body. To close the can there are two possibilities, (1) the can does not move while the roller pushes and turns, or (2) the can turns while the roller just applies pressure. The turning speed is regularly measured in terms of cans per minute, and this can go from 25 up to 275 in a range of can diameters from 200 mm to 603 mm.

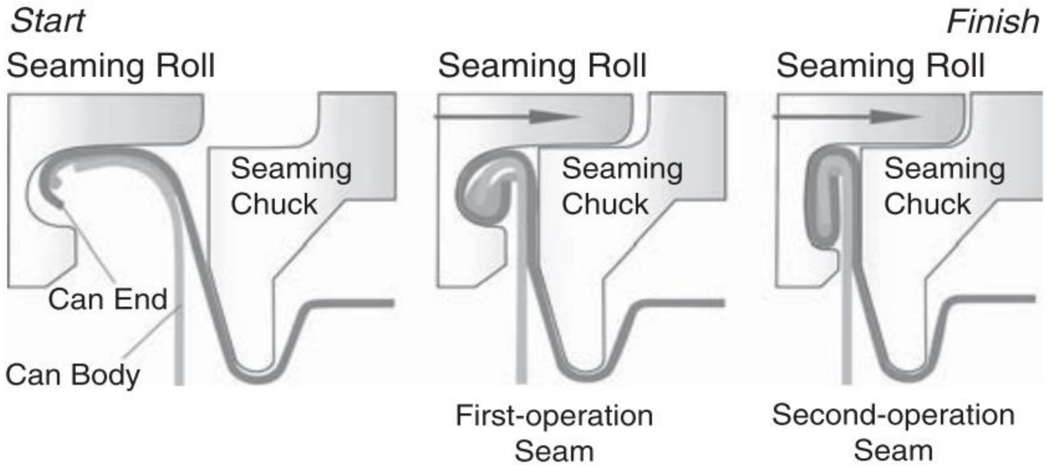

Figure 1 Scheme of a can seaming system [Yam 2009].

Construction materials for seaming rolls

The rollers are normally manufactured of hard and wear resistance materials steel like AISI D2 steel since they shouldn’t be in contact with lubricant oil, metal debris, sewage, and other pollutants[Yam 2009]. To improve the performance and make the parts last longer, it is possible to find rolls with metal nitrides or carbides films, which due to the metallic character of their chemical bonds, are well known for good electrical and thermal conductivities, metallic lustre and mechanical hardness, wear resistance and very low chemical reactivity.

Commercially it is possible to find AISI D2 steel rollers uncoated and coated with titanium nitride and titanium carbide thin films. Both have been extensively studied, and it has been shown that they exhibit good corrosion resistance[Chen et al. 1999; Fenker, Balzer, and Kappl 2006; Kral et al. 1998; Igual Muoz and Espallargas 2011], as well as an excellent wear resistance under a variety of conditions[Henry et al. 2013; Samano et al. 2010; Ching et al. 2014]. A summary of the hardness and common thickness values of coatings on rollers is presented in Table 1.

Table.1 Hardness values and coatings thickness of common materials for the manufacture of rolls for can seaming systems.

Material	Hardness (GPa) [Puchi-Cabrera 2002; Chen et al. 1999]	Thickness (μm) [Imeta Srl 2018]
Titanium Nitride (TiN)	23	6-8
Titanium Carbide (TiC)	31	6-8
AISI D2	7	---

Transition metals nitrides as thin films for construction materials in the food industry

The transition metal nitrides commonly have crystalline structures where the atoms of nitrogen occupy interstitial sites in the metal lattice. This kind of arrangement and type of bonding can confer these compounds with excellent chemical, physical and mechanical properties such as resistance to deformation, abrasive wear and corrosion along with high melting points, metallic, lustre, and even superconductivity.

Due to their properties, these nitrides can be used for different applications as structural, electronic, magnetic, optical, and catalytic materials. Elements that belong to the same group and present similar behavior and properties, such as molybdenum and tungsten and the nitrides of these elements can present similar performance and properties as chromium nitride.

Often, to obtain wear–resistance nitride thin films, methods such as Chemical Vapor Deposition (CVD) and Physical Vapor Deposition (PVD) are employed. In general, the mechanical and electrochemical properties of different nitride thin films have been reported, but there are almost no publications about their tribocorrosion properties.

Tungsten nitride as a protective film

As we mentioned before, among the nitride compounds tungsten nitride presents a range of useful properties, such as excellent hardness, chemical stability and thermal stability [Gonohe 2002; Samano et al. 2010; Addonizio et al. 2012; Polcar, Parreira, and Cavaleiro 2007b; 2008; Nakajima, Kudo, and Mizuno 1999; Wen et al. 2010]. Because of that, different efforts to produce this nitride as a thin film have been carried out. Some of the reported methods are reactive magnetron sputtering[Peter Hones et al. 2003; P. Hones et al. 2000; Addonizio et al. 2012; Prakash, Jayaganthan, and Kaur 2016; Baker and Shah 2002; Polcar, Parreira, and Cavaleiro 2007b; 2008; Shen and Mai 2000; Wen et al. 2010], pulsed laser deposition[Soto et al. 2003], atomic layer deposition, and chemical vapor deposition[Gonohe 2002].

Due to its properties, one can consider that tungsten nitride might be a suitable protective thin film to be used on construction materials for the food industry. The present study aims for an industrial application, and one of the most suitable synthesis methods is reactive sputtering, as sputtering is already industrially used to produce thin films at industrial level. Some of the advantages of this method are that precursor materials are often not hazardous[Beitz and Kuttner 1994; Addonizio et al. 2012], high-quality films can be applied to large areas, and the film surface can have very few defects[Fenker, Balzer, and Kappl 2006].

With reactive sputtering, it is possible to obtain tungsten nitride in a range of various compositions and structures depending on the experimental settings. The stoichiometric phase W_2N has been reported as the most stable phase, which is a crystalline face centered cubic structure as shown in Figure 2. Moreover, to obtain such structure, by reactive sputtering, it is recommended to use around 12% of N_2 in the mixture of gases during the deposition process [Addonizio et al. 2012; Baker and Shah 2002].

As for the known properties of this material, hardness and Young's modulus can have values from 29 to 39 GPa and 300 to 390 GPa, respectively [Polcar, Parreira, and Cavaleiro 2007b]. Such values depend on the composition and structure of the tungsten nitride thin film. Moreover, large nitrogen contents are associated with the higher hardness while the largest Young's modulus is related to the smallest nitrogen concentration.

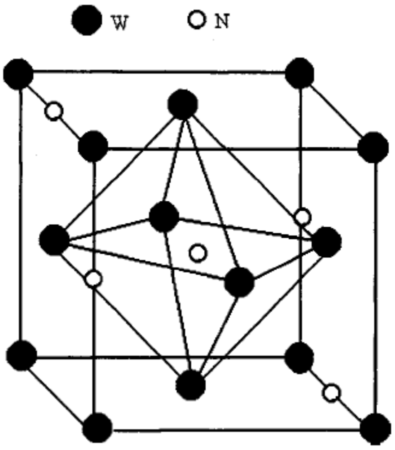

Figure 2 Representation of W_2N fcc crystalline structure [Baker and Shah 2002]

In general, the studies of tungsten nitride have been focused on its mechanical properties[Polcar, Parreira, and Cavaleiro 2007a; P. Hones et al. 2000; Wen et al. 2010; Polcar, Parreira, and Cavaleiro 2007b; 2008; Samano et al. 2010], but some people had explored other applications such as electrodes [Villaseca et al. 2015], and optical devices[Addonizio et al. 2012]. To the best of our knowledge very little literature exists about its electrochemical behavior and corrosion resistance. There are only reports about metallic tungsten [Stojadinović et al. 2009] and nitrides of other metals combined with tungsten [Prakash, Jayaganthan, and Kaur 2016; Fenker, Balzer, and Kappl 2006; Fathollahzade and Raeissi 2014]. As for the combined effect of tribocorrosion of tungsten nitride, no information has been published at the moment of drafting this thesis.

Because of its known properties, the use of tungsten nitride as a thin film to protect against tribocorrosion was explored. Such thin films were synthesized by rf magnetron sputtering under different conditions. To probe the tribocorrosion resistance a special cell was designed and constructed.

Chapter 1

State of the art and experimental techniques

1.1 Surface wastage, a tribocorrosion approach.

A physical surface is part of a solid that presents certain electronic, mechanical, and chemical properties that can influence the behavior of the bulk material. It can be broadly defined as a geometrical boundary between the solid and the contact with other solids or the environment [Menezes et al. 2013]. The study of solid surfaces, although complex, can lead to an understanding of superficial phenomena and partial or total control of the surface properties. The preparation of a material surface is fundamental for the industry when the interaction between surfaces and the environment predefines functions related to aspects such as friction, resistance to mechanical stress, wear, and corrosion resistance. The structure of a surface can be described by its roughness, waviness, lay, and flaws all of which determine its texture.

When a solid is in contact with another solid surface, several changes can happen for example, elastic and plastic deformations, chemical reactions, and material loss. In Essence, tribology has been developed to study the mechanical interactions between two surfaces in static contact or relative motion [Heldman 2013; Street 2010; Imeta Srl 2018].

1.1.1 Surface tribology and wastage

Tribology covers a broad spectrum of arrangements from micro and nanomechanical systems up to the field of traditional macroscopic tribology and to the contacts between tectonic plates [Menezes et al. 2013].

To understand the relevance of tribology, one only need to think about any phenomena whenever two solids touch each other. Here the forces of action and reaction are brought into play and surface interaction dominates. Due to this interaction, surface structure changes can occur, and matter may be transferred between surfaces, or the surfaces can break.

1.1.2 Wear generalities

Around the year 1500 Leonardo da Vinci got interested in the study of mechanics that had been abandoned after by the ancient Greeks. His research about movement gave him ideas of concepts such as inertia, momentum, efficiency, friction, and center of gravity. The fundamental laws of Leonardo da Vinci, which were re-discovered two centuries later by Amontons:

- "The friction force is proportional to the weight of the body that moves over a horizontal plane and to the normal load applied to a surface."
- "Friction is independent of the apparent contact area."
- "Friction depends on the materials and the state of their surfaces."

These laws were completed by Coulomb who described the difference between static and dynamic friction forces, by saying: "The friction force is practically independent of the sliding speed of surfaces."

These laws are now the base of tribology which comprises the study of friction, wear, and lubrication. In tribology, we study the phenomena that concern the set of contact factors that play a role in friction, ergo, mechanical stress, temperature, third body behavior, etc. These factors are the mechanical, physical, and chemical properties of the materials.

Friction is a tribology phenomenon observed in a great variety of sliding and rolling situations, and it can only be defined in a system of at least two bodies in contact. Furthermore, it can be defined as the force that acts against the relative motion between two bodies in contact. Friction can be dry or fluid; dry friction, also known as Coulomb friction, occurs under dry conditions while fluid friction occurs in lubricated conditions [Menezes et al. 2013]. Friction is often described by a dimensionless scalar value called the coefficient of friction (μ) which is defined as the ratio of the friction force F to the normal load F_N.

$$\mu = \frac{\mathrm{F}}{F_N} \qquad eq. (1.1)$$

Where the normal force is defined as the net force compressing two parallel surfaces together and the friction force is the resisting force which acts in an the opposite direction to the direction of motion[Menezes et al. 2013; Beitz and Kuttner 1994].

When there is relative motion between two surfaces, the progressive loss of material from any of these caused by mechanical influences is called wear. The material loss is regularly exhibited by the appearance of small detached particles and changes in the surfaces exposed to a normal force[Beitz and Kuttner 1994; Scharf and Prasad 2013; Godet et al. 1991; Menezes et al. 2013]. This effect is normally undesired therefore, many systems have been studied to understand how wear occurs and how to find ways to diminish the material loss[Jiang and Stack 2006; Bailey and Sayles 1991; Roberts and Williams 1992; Castillejo et al. 2014; Henry et al. 2013; Cho, Lee, and Lee 2015]

Wear is produced by the effect of physical and chemical processes which occur during the relative motion of two bodies in contact. 'Depending on the physical and mechanical processes occurring in the body surfaces it is possible to recognize different types of wear such as:

- **adhesion**, which is produced by the formation and breaking of atomic links between the surfaces in contact.
- **abrasion**, that refers to the scratching and micromachining of surfaces and by an increase in the roughness.
- **surface disruption**, this can happen when at least one of the surfaces cracks or propagates a crack in the opposing surface, with separation of particles due to alternating loads in the system.
- **tribo–chemical reactions,** this is present when there are chemical reactions of the bodies in contact, or the ambient, and the tribological reaction can then be enhanced due to the appearance of friction.'

- **lubrication** refers to the presence of a lubricant.

Lubricants are used to lower the friction between two sliding bodies and therefore reduce wear. Additionally, they can help to distribute heat, remove contaminants, and improve the efficiency of mechanical systems. In general, lubricants are classified as liquid, solid, or gaseous[Menezes et al. 2013]. Solid lubricants are commonly used when lubrication under extreme conditions is required, such as very high or low temperatures, aggressive environment, or vacuum[Beitz and Kuttner 1994].

1.1.3 Contact mechanics

In general, contact can be described by a set of external efforts, forces, and momentum applied over two surfaces. The contact of two ideal surfaces of two different bodies under the action of a normal force (F_N) will create strain and deformations over both bodies. Here the contact pressure (P) will appear over the contact area (A), in between the two surfaces. Such pressure is defined by:

$$P = \frac{F_N}{A} \qquad eq. (1.2)$$

In the region where the contact is made, there will be a certain deformation. From a mechanics point of view, deformations have two regimes, each with different properties. The nature of the contact will depend on these regimes, and therefore on its mechanical properties.

One of these regimes is the Hertzian contact, in which there are only plastic deformations, commonly found in a sphere/sphere, sphere–plane and parallel cylinders contact types. It is possible to consider a Hertzian contact if:

- The material is homogeneous and isotropic.
- The deformation is considered small.
- There is no friction between the surfaces (absence of tangential forces).
- The contact area ratio is much smaller than the curvature ratio.

In the case of contact between a sphere and a plane (Figure 1.1), it is possible to calculate the deformation and stress by applying the theory of Hertz. According to this theory, if we have a contact with a F_N different from zero, both bodies in contact will be deformed in a circular region of *radius* (*a*) given by the following expression:

$$a = \left(\frac{4}{3}\frac{R}{E'}\,F_N\right)^{1/3} \qquad eq. (1.3)$$

Where R is the radius of the sphere and E′ is the combined Young's modulus given by the Young's modulus of each material (E_1, E_2) and their Poisson ratio (ν_1, ν_2) in the following expression:

$$\frac{1}{E'} = \frac{1-\nu_1^2}{E_1} + \frac{1-\nu_2^2}{E_2} \qquad eq.\ (1.4)$$

Now it is possible to define the contact area (A) as:

$$A = \pi a^2 \qquad eq.\ (1.5)$$

With an average pressure or Hertz pressure (P_m) given by:

$$P_m = \frac{F_N}{\pi a^2} \qquad eq.\ (1.6)$$

Taking into consideration all the aspects affecting wear, it is not possible to reduce the concept to a simple material loss. One must keep in mind that this definition hides numerous different phenomena, which produce a set of geometric and physicochemical changes to the superficial layers exposed to friction.

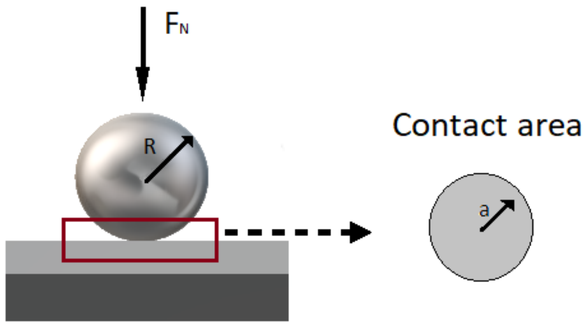

Figure 1.1 Representation of a Hertz contact between a sphere and a plane.

between a sphere and a plane.

1.1.4 Main wear mechanisms in sliding contacts

To determinate the wear mechanisms in a given sliding contact it is important to consider a set of phenomena not always easy to interpret. These phenomena are the emission of debris, mass loss, the shape of the wear track, and the physical and chemical changes in the surface in contact. For sliding contacts, four main types of wear mechanisms are recognized [Ionescu, Constantin, and Caract 2013; Cao and Mischler 2018b] and described next.

1.1.4.1 Adhesive wear

When in a sliding contact a surface loses material, the material is transferred and attached to the surface of another body so junctions of asperities might be formed. Frequently, the material transfer will occur from a soft to a hard material surface, so subsequent sliding will produce sheared and loose wear debris. This kind of wear will occur when the two surfaces experience short–range Van der Waals forces, which come into action at about 1 nm to form strong adhesive junctions. For this type of mechanism, the amount of wear depends on the location of the junctions sheared. A schematic representation of this wear mechanism is shown in Figure 1.2 c.

1.1.4.2 Abrasive wear

Abrasive wear comes from material displacement produced by hard particles or hard protuberances. When a hard material slides along a soft surface with protuberances, due to the shear strength there will be two-body abrasive wear (Figure 1.2 a), but if wear debris gets caught between two surfaces and at least one of the surfaces is abraded, then it is called third-body abrasive wear (Figure 1.2 b).

The model to describe abrasive wear assumes that the asperities will act as a sharp tool that will displace a volume of material. The surfaces damaged by abrasion present wear marks of variable depth parallel to the movement. Wear is constant in function of time while the debris volume grows linearly with the applied load and the distance.

The material lost depends on the wear and antagonist materials, the wear marks give further information about the origin of the asperities[Ionescu, Constantin, and Caract 2013]. When the wear marks of little depth and shine, the asperities of the antagonist piece correspond to oxide layers.

If the wear marks are isolated, and severely interrupted, then hard particles have been introduced in between the surfaces, hence such hard particles are found to be incrusted. Whereas, when they are interrupted and have scratched the hard surface, then the abrasive particles are embedded in the soft surface. Finally, if they are interrupted and present over the soft material, it means that the antagonist piece is very rough.

1.1.4.3 *Fatigue wear*

Surface fatigue can be observed at microscopic levels when asperities are found between sliding surfaces. The repeated loading and unloading cycles (stress cycling) may induce the formation of cracks so that a critical number of cycles will result in the breakup of the surface, leaving large pits. Unlike adhesion and abrasion, the asperities in fatigue wear make contact without adhering or abrading, but instead deforming plastically the surface and subsurface until cracks nucleate[Cao and Mischler 2018b; Menezes et al. 2013]. Once the cracks are formed, further loading will make cracks extend and propagate, a scheme of this type of wear is shown in Figures 1.2d and 1.2e.

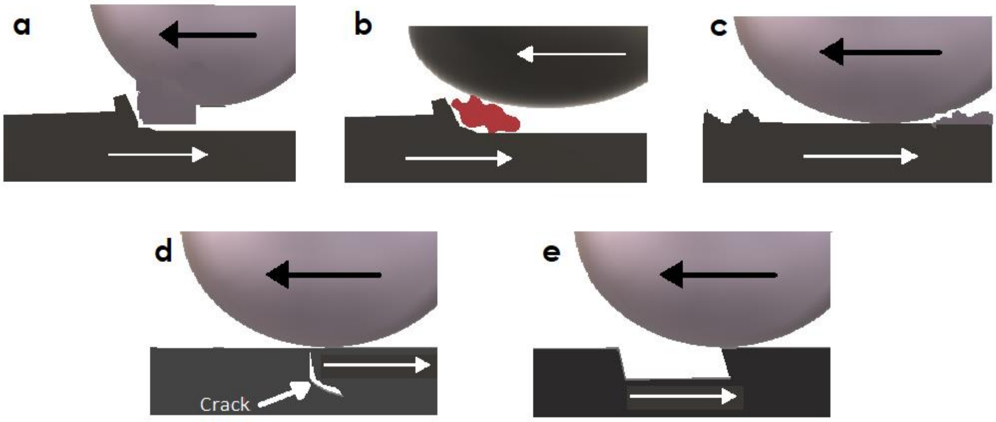

Figure 1.2 Illustrations of different wear types. (a) third body abrasive wear; (b) three bodies abrasive wear; (c) adhesive wear, (d) and (e) fatigue wear.

1.1.4.4 *Corrosive wear*

When sliding takes place in a corrosive environment, the wastage of the surface can be called corrosive wear. In such a process, a chemical or electrochemical reaction contributes to material removal. The reaction layers in the contact lead to the formation of wear debris consisting mainly of reaction products. Currently, this type of wear is studied by tribocorrosion methods[Cao and Mischler 2018b; D. Landolt, Mischler, and Stemp 2001].

1.1.5 Corrosion of materials

Corrosion occurs when a material reacts by exchanging electrons (oxidation-reduction) with the surrounding environment. When the material and the environment (electrolyte) are electrical conductors, this phenomenon occurs as electrochemical corrosion. For example, a metal immersed in a solution.

When corrosion occurs, there are modifications in the composition of the material surface, generally as a functional degradation of the material and a modification of the environment. Redox reactions can be described in a simplified way, written as follows:

$$Oxidation\ reaction: \quad M \rightarrow M^{n+} + ne^- \qquad eq. (1.7)$$

$$Reduction\ reaction: \quad H^+ + e^- \rightarrow \frac{1}{2}H_2 \qquad eq. (1.8)$$

$$2H_2O + O_2 + 4e^- \rightarrow 4OH^- \qquad eq. (1.9)$$

As wear, corrosion resistance is not an intrinsic property of the material. It depends completely on the physicochemical conditions and the environment.

1.1.5.1 *Interface solid/liquid*

When a metal is in contact with an aqueous solution, an interface is formed. This interface (commonly named electrical double layer) is constructed of different layers, as displayed in Figure 1.3. The nearest to the metal surface (inner Helmholtz layer) is where electric charges of the adsorbed ions are located. This is followed by a second layer called Helmholtz outer layer, which contains solvated ions. Finally, a "diffuse layer" is made of ions distributed in a three-dimensional region between the Helmholtz outer layer and the bulk[Fernandez-Solis et al. 2016].

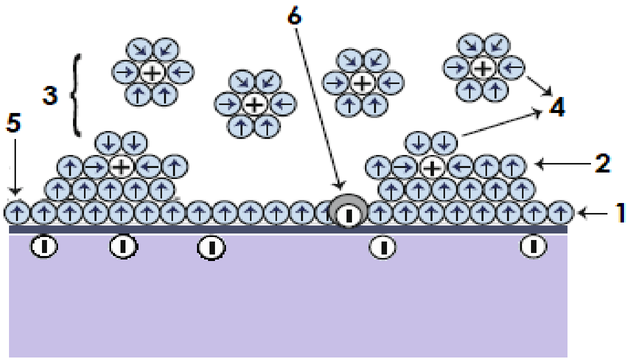

Figure 1.3 Representation of the layers at a solid/liquid interface. 1 Inner Helmholtz layer, 2 Outer Helmholtz layer, 3 Diffuse layer, 4 Solvated ions (cation), 5 Electrolyte solvent, 6 Specifically adsorbed ions. Image adapted from [Fernandez-Solis et al. 2016]

When this interface is formed an equilibrium is reached. This equilibrium has an associated potential, also known as the open circuit potential (E_{OC}/OCP), which represents an electrochemical cell when no current is flowing [Amemiya et al. 2007].

The electrochemical potential ($\bar{\mu}_i$), represents the mechanical work required to change 1 mol of ions with valency z and charge z_e from a standard state to a specific electrical potential and concentration. This electrochemical potential comes from the following expression:

$$\bar{\mu}_i = \mu_i + z_i F \Phi \qquad eq.(1.10)$$

Where μ_i represents the chemical potential of the species *i*, F is the Faraday constant and Φ the local electrostatic potential.

1.1.6 Corrosion rate determinations.

In general, the corrosion rate is defined by the corrosion mechanisms. These mechanisms are established by the atomic, molecular, or ionic transport processes that take place at the interface. The processes can occur over several steps, where the slowest of them commonly controls the rate of the overall reaction. Since it is not possible to directly observe on an atomic scale these steps, it is necessary to infer probable mechanisms from indirect measurements and observations. For example, measurements of electrical potential and current.

The corrosion rate of a material depends on both the material properties and the environment. For the study of a material, it is important to consider composition, crystallinity, grain size, and surface roughness. In the case of the environment: conductivity, pH, and corrosion products.

Corrosion rate determinations are frequently done using a cell in a three electrodes arrangement. Those electrodes are a Working Electrode (WE) that will be the analyzed sample, a Counter Electrode (CE) which will be an electrode of a material immune to the conductive environment or electrolyte and a Reference Electrode (RE). An image of this arrangement is shown in Figure 1.4.

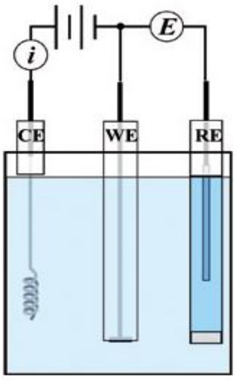

Figure 1.4 representation of a three electrodes cell [Amemiya et al. 2007]

1.1.6.1 *Potentiodynamic curves and Tafel extrapolation method*

One option to estimate the corrosion rate is to take current measurements while the working electrode is polarized from the E_{OC}. The measured data is expressed as an E (log i) curve as shown in Figure 1.5. To apply this method, the resulting polarization curve must present a linear or "Tafel region" in at least one of the branches (cathodic or anodic)[Fernandez-Solis et al. 2016]. A potential scan of around ± 100 mV about E_{corr} is required to determine whether a linear section of at least one decade of current is present so that a reasonably accurate extrapolation can be made. The linear section must be present in at least one of the redox branches. Tafel regions can be observed at some tens millivolts from the corrosion potential (E_{corr}).

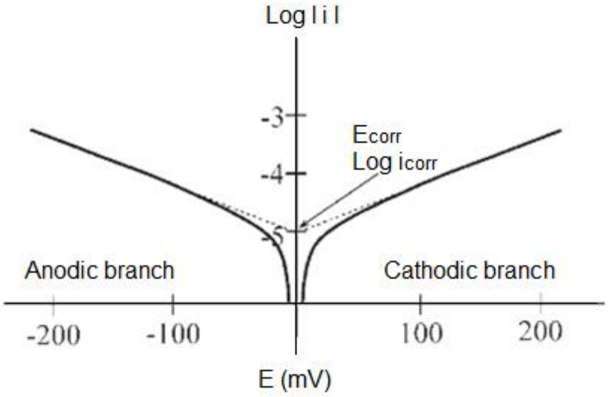

Figure 1.5 Polarization curve with Tafelian behavior where the corrosion current i_{corr} is found at the E_{corr} [Amemiya et al. 2007]

Corrosion currents can be converted into corrosion rates because the oxidation at a specific current corresponds to a particular loss of material. To transform the corrosion current to corrosion rate (CR) *eq.1.11* can be applied.

$$CR = \frac{i_{corr} * K * EW}{\rho * A} \qquad eq.(1.11)$$

Where: EW =Equivalent weight of the material, K= 3.27 x 10^{-3} mm g/μA cm year, ϱ= Material density, and A = sample area

1.1.6.2 *Electrochemical Impedance Spectroscopy (EIS).*

EIS tests consist of the application of small sinusoidal perturbations of a potential (5-10 mV), typically in a range of frequencies between 10^{-4} and 10^{6} Hz[Stansbury and Condra 2000; Fernandez-Solis et al. 2016]. Therefore, it is considered a non-destructive method for the evaluation of a wide range of materials. The response to these perturbations is the electrical current, and it can be analyzed as a sum of sinusoidal functions (Fourier series). This analysis can provide information about parameters such as corrosion rate, electrochemical reaction mechanisms, and kinetics.

The excitation signal, expressed as a time function, can be written as:

$$E_t = E_0 \ \sin(\omega t) \qquad eq.(1.12)$$

Where E_t is the potential at the time t, E_0 is the signal amplitude and, ω is the radial frequency defined as:

$$\omega = 2\pi f \qquad eq.(1.13)$$

In a linear system, the response as electrical current (I_t) is shifted in phase (φ) with a different amplitude (I_0):

$$I_t = I_o \cos(\omega t - \varphi) \qquad eq.(1.14)$$

The analysis of the electric current measurements allows to determine the complex impedance:

$$Z_{(\omega)} = \frac{|\Delta E|}{|\Delta I|} \qquad eq.(1.15)$$

Z represents the ratio between the sinusoidal electric potential and the electric current. Often a complex plane representation of the elements, that describes the impedance, is used. Here the potential can be written as:

$$E_t = E_0 \ e^{-i\omega t} \qquad eq.(1.16)$$

With $i = \sqrt{-1}$. We have,

$$I_{(t)} = I_0 e^{i(\omega t - \varphi)} \qquad eq.(1.17)$$

Which allows simplifying the radio in *eq. 1.15* as:

$$|Z| e^{i\varphi} = |Z|[\cos(\varphi) + i \sin(\varphi)] \qquad eq.(1.18)$$

To analyze EIS results the equivalent circuits method is commonly used. Regularly the Randles circuit, which describes the response as a combination of capacitors and resistors, is the starting point[Fernandez-Solis et al. 2016; Orazem and Tribollet 2008]. To have an idea of the behavior, the results are frequently displayed as Nyquist and Bode plots (Figure1.6).

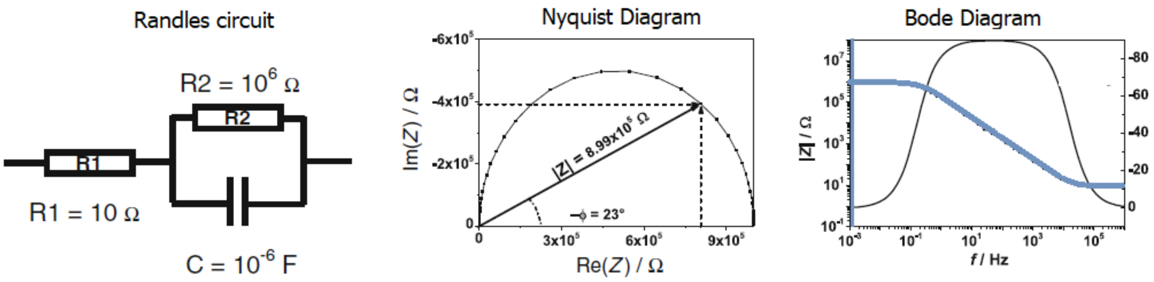

Figure 1.6 Randles circuit and it equivalent as Nyquist and Bode plots, modified from reference [Fernandez-Solis et al. 2016]

1.2 Tribocorrosion

Tribocorrosion is the research area that combines the domains of tribology and corrosion, which seeks to understand the surface degradation mechanisms when mechanical wear and electrochemical processes interact with each other[Wood 2007; Fathollahzade and Raeissi 2014; Gracia-Escosa et al. 2015; Obadele et al. 2015; Nix 1989; Arunkumar 2018]. This research area began in the late 1980s and has merged in recent years driven by the increasing demand for biomedical implants, power generation, marine, and offshore industries[Cruz Garcia, Sánchez Moragas, and Nordqvist 2014; Obadele et al. 2015; Nix 1989; Kempf, Göken, and Vehoff 1998]. This research area aims to understand and control tribocorrosion processes to improve the useful lifetime of man-made objects and machines, and to allow safe operation of machines, and devices.[Fathollahzade and Raeissi 2014; Gracia-Escosa et al. 2015; Obadele et al. 2015; Nix 1989]

The degradation of a surface by tribocorrosion depends on a wide range of parameters related to the corrosive environment and the materials in contact with it. Figure1.7 shows a scheme of such parameters. The details of the contact play a critical role in determining the effect of corrosion on the wastage rate, to understand the mixed contribution first we need to understand how each contribution works separately.

Figure 1.7 Representation of the elements parameters and system characteristics which can influence the response of tribocorrosion processes. Translated from [Richard and Geringer 2019].

Total wear is caused by friction, changes of the electrochemical state, and kinetics of the reactions that are expressed as the destruction of surface layers. The destruction of the surface layers will result in a heterogeneous surface which can provoke galvanic coupling between the slid track and the passive film.

1.2.1 Influence of sliding over corrosion resistance and influence of corrosion over sliding.

Some materials create a passive film over the surface (passivating materials). This passive film can be damaged or partially removed in a sliding system. When this happens in a corrosive environment[Richard and Geringer 2019], a redox reaction occurs. Such a reaction occurs to rebuild the passive film. In certain systems, this will also imply a parallel dissolution of material into the environment. In general, corrosion produces modifications in the surface composition, and so in the mechanical properties. Similarly, the formation of oxides or corrosion products on the surface can originate or modify a third body, and therefore the friction and the wear mechanism. In an aggressive environment, modifications in composition and surface properties can produce selective dissolution, which can be accelerated by the galvanic coupling effect[Richard and Geringer 2019].

Nevertheless, tribocorrosion can also be controlled by mechanical phenomena, where the corrosion of the surface indirectly participates in the production of abrasive particles.

1.2.2 Synergism between corrosion and wear

Simultaneous mechanical and chemical interaction can occur in a great variety of conditions. Two or three bodies in contact and relative motion put in an aggressive environment, often behave as tribocorrosion systems. The relative movement of the contact surfaces can be unidirectional or alternating.

The consequences of friction and corrosion coupling are complex to study and master. To deduce the tribocorrosion behavior of a system it is not enough to know the tribological system in absence of a corrosive environment and the performance of an electrochemical system not exposed to friction. *Friction affects the corrosion behavior as much as corrosion modifies the overall response of the tribological system*. So, it is possible to say that there is a synergy between corrosion and friction, which will affect the wear mechanisms and the total material loss.

Since tribocorrosion is an independent phenomenon, to try to estimate the details. Various groups have proposed to measure the synergism between tribology and corrosion, so the total wear (W_t) will be given by the sum of a mechanical contribution (W_m), an electrochemical one (W_c) and, a synergism term (W_S). The last term represents the amount of material loss due to the combined effect of corrosion and wear. The simplest way to express this relation is given by *eq. 1.19*.

$$W_t = W_m + W_c + W_s \qquad eq.(1.19)$$

The synergism term is defined here as the sum of the change of wear due to corrosion (W_{cm}) and the modification in corrosion due to wear (W_{mc}).

$$W_s = W_{cm} + W_{mc} \qquad eq.(1.20)$$

If we substitute 1.20 in 1.19, we get:

$$W_t = W_m + W_c + W_{cm} + W_{mc} \qquad eq.(1.21)$$

The effect of wear on corrosion is referred to as the 'additive effect'. The 'synergistic effect' is defined as the enhancement of wear due to corrosion and the 'negative synergism' or 'antagonistic effect' is the protection of the surface against further wear due to the electrochemical formation of a protective layer[Levy et al. 2006; Igual Muoz and Espallargas 2011; Dieter Landolt and Mischler 2011; Levy et al. 2016].

1.2.3 Tribocorrosion evaluation by the American Society for Testing and Materials, Standard guide for determining synergism between wear and corrosion (ASTM G119-09)

To determine the synergism effect in a tribocorrosion system, there are two frequently used ways. The first one is proposed by the ASTM in the standard guide G119-09[ASTM G119-93 1998]. This standard proposes a series of steps and tests to estimate the synergism on tribocorrosion of metals. The steps and description of the measurements are summarized below.

I. *A wear test of a sample in contact with a corrosive environment.* From this test, the volume loss per unit area will be obtained. This value represents the total material loss rate (W_t)

II. *A wear test as in I in a three-electrode configuration.* Under this configuration, a polarization resistance (Rp) and a potentiodynamic polarization curve should be performed. From these tests Rp, Tafel constants β_a y β_c are tabulated and used to calculate i_{cor} that will be converted to penetration rate following the ASTM G-102 (as corrosion rate in *eq. 1.11*), this value represents W_{cm}

III. *A wear test as in II but now the sample is polarized 1V cathodic vs E_{cor}*. Here the mass loss is measured, and it represents W_m

IV. Finally, a corrosion test, similar to II without wear is run and so the penetration rate is calculated (W_C)

The ASTM G-119 recommends reporting different augmentations factors, *eq. 1.22* to *eq. 1.24* shows how to calculate them.

Total synergism factor
$$\frac{W_t}{W_t - W_s} \qquad eq.(1.22)$$

Corrosion augmentation factor
$$\frac{W_c + W_{cm}}{W_c} \qquad eq.(1.23)$$

Wear augmentation factor
$$\frac{W_m + w_{mc}}{W_m} \qquad eq.(1.24)$$

With these results, it is possible to see if the "synergism effect" enhances the wear due to corrosion (positive synergism) or protect the surface (negative synergism). The main limitation of this method resides in the fact that under the experimental set up it is not possible to truly separate the different contributions in the total wear loss, for example in the cathodic polarization tests described in III it is possible to assume that material loss is only due to wear, even though the absence of corrosion products can affect the response of the sample tested. So, this will not correctly represent the real-life wear behavior of a surface[Celis and Ponthiaux 2012].

1.2.4 Electrochemical Impedance Spectroscopy as a tool for tribocorrosion

An alternative methodology, based on the time cyclic evolution of the wear track, has been proposed and tried by different authors[Mischler 2008; Igual Muoz and Espallargas 2011; Cao and Mischler 2018a; 2018a; D. Landolt, Mischler, and Stemp 2001; Celis and Ponthiaux 2012]. It entails electrochemical impedance spectroscopy (EIS) measurements under continuous and intermittent sliding. The combination of these experiments allows gathering information about the evolution of the surface with time as well as the identification of the mechanisms of material loss and surface degradation. This protocol is designed as a series of successive steps that provide important information about the tribocorrosion of passivating materials. Such steps are listed as follows:

I. Electrochemical tests on a passive material without sliding. These tests should be carried out in a three electrodes arrangement.

   a. Estimation of the reaction time characteristic of the system by the measurement of the open circuit potential (E_{OC}) until a steady value (±1mV/min).

   b. Polarization resistance (R_P) of the passivated material is measured by EIS and the specific polarization resistance of passive material (r_{pass}) is calculated for a sample of area A_0 applying *eq. 1.25*.

$$r_{pass} = R_p A_0 \qquad eq. (1.25)$$

   c. Calculation of the corrosion current density of the material covered by a passive film i_{pass} can be calculated with *eq. 1.26*.

$$i_{pass} = \frac{B}{r_{pass}} \qquad (1.26)$$

II. Electrochemical tests on active sliding track during sliding tests. In a three-electrode configuration, sliding tests at the desired conditions are performed while EIS measurements are made. In the case of rotation (ball or pin on disc), it is recommended to take as rotation period (t_{rot}) $t_{react}/10000$. This allows to estimate the corrosion current density of an active material.

III. Electrochemical tests on partially active sliding track during sliding tests. In a configuration as in II, EIS measurements are carried out on intermittent sliding. The time of sliding pause or latency time (t_{lat}) is recommended to be $t_{react}/100$.

Such a series of steps give unique information about the surface at different stages of the tribocorrosion process. This protocol defines the material loss at the wear track is defined by *eq. 1.27*

$$W_{tr} = W_{act}^{c} + W_{act}^{m} + W_{repass}^{c} + W_{repass}^{m} \qquad eq.(1.27)$$

Where:

W_{tr} = Material loss in the wear track

$W_{act}^{c} = Material\ loss\ due\ to\ corrosion\ of\ the\ active\ material\ in\ the\ wear\ track$

$W_{act}^{m} = Material\ loss\ due\ to\ mechanical\ wear\ of\ active\ material\ in\ the\ wear\ track$

$W_{repass}^{c} = Material\ loss\ by\ corrosion\ of\ repassivated\ material\ in\ the\ wear\ track$

W_{repass}^{m} = *Material loss by mechanical wear of the repassivated material in the wear track*

Moreover, applying *eq. 1.28* the ratio between corrosion and mechanical material losses (*K_c*) can be calculated.

$$K_c = \frac{W_{act}^{c} + W_{repass}^{c}}{W_{act}^{m} + W_{repass}^{m}} \qquad eq.(1.28)$$

In general, the K_c value can describe three behaviors; i. $K_c > 1$, the material loss is predominantly due to corrosion. The total wear is mainly controlled by the reactivity of the substrate with the environment. ii. $K_c < 1$, the material loss is predominantly caused by mechanical wear and iii. $K_c \ll 1$, the contribution due to the acceleration of corrosion induced by the destruction of the passive film is negligible compared to the total wear.

Additionally, the wear experienced by the combined effect can be evaluated to determine the electrochemical and mechanical components of the total wear by applying the following equations.

$$W^{c}_{act\;l} = \left(\frac{C_F}{Fd}\right)\, i_{act\;l} A_{act\;l} N t_{lat} \qquad eq(1.29)$$

$$W^{m}_{act\;l} = W^{m}_{Act\;1}\left(\frac{A_{act\;l}}{A_{act\;1}}\right) \qquad eq.(1.30)$$

Were:

$\mathrm{W}^{\mathrm{c}}_{\mathrm{act1}}$ = Material lost due to corrosion of the active material in the wear track during the continuous sliding test.

C_F = Sum of the ratios of the atomic weight and number of electrons involved in the reaction for each metal.

N= Number of cycles during the pin of disc test

$i_{act\;l}$= corrosion current of the active region during the latency tests.

A_{act1}= Active area during the continuous pin on disc test

W^{m}_{act1} = Material lost due to mechanical wear of the active material in the wear track during the continuous sliding test.

$W^{m}_{act\;l}$ = Material lost due to mechanical wear of the active material in the wear track during the continuous sliding test.

Furthermore, the information acquired during this test allowed evaluating of the effect of the formation of the passive film on the mechanical wear by the ratio between the specific mechanical wear on the active and passivated parts of the wear track (K_m), defined by *eq. 1.31*. Two cases can be distinguished; "i. K_m >1, the passive material protects the material against mechanical removal. ii. K_m < 1, the formation of the passive film accelerates the mechanical removal of the material.

$$K_m = \frac{W^{m}_{act\;lat}}{W^{m}_{repass\;lat}}\,\frac{A_{repass\;lat}}{A_{\;act\;lat}} \qquad eq.(1.31)$$

1.3 Characterization techniques

1.3.1 Scanning electron microscopy (SEM)

Scanning electron microscopy is widely used to examine surface topography and morphology by producing high resolution images. SEM works at high electron energies (typically, 5 – 100 keV) and it is this highly focused beam that scans the surface of a sample. Figure 1.8 presents a schematic image of the core components of a scanning electron microscope.

The electron beam arrives at the surface with an energy E_0 which generates elastic and inelastic interactions. The elastic interactions are produced by collisions "incident electron-nucleus", while the inelastic are mainly due to collisions "incident electron-material electron".

The expected interactions are divided in several groups (Figure 1.9)[Ruste 2013]:

- Primary electrons from the beam can exit the sample after the elastic and inelastic collision. This phenomenon is called backscatter electron emission.
- Secondary electron emission occurs due to an inelastic collision between an incident electron and the electron cloud of the atoms in the sample. The collision leads to the ejections of an electron from the cloud, this is known as ionization.
- Material ionization can produce a deexcitation of the atom with the emission of Auger electrons or photons (fluorescence). This is a function of the atomic composition of the sample and the geometry of the features under observation.
- For semiconductors and insulating materials, a photomagnetic emission is possible. This cathodoluminescence, most of the time, is due to the displacement of an electron from the valence band to the conduction band.

From all these interactions, an image of the surface can be spatially reconstructed on a phosphor screen (or CCD detector) from the intensity of the secondary electron emission at each point scanned by the incident beam. Because of the shallow excitation depth of low-energy electrons produced by the primary electron beam, only the secondary electrons and the backscattering electrons can escape and be detected.

The backscattered electrons come from deeper regions of the sample, while the secondary electrons originate from surface regions. Therefore, backscattered electrons and the secondary electrons carry different types of information. Images obtained from the backscattered electrons show high sensitivity to differences in atomic number; the higher the atomic number, the brighter the material appears in the image, while secondary electrons imaging can provide more detailed surface information, useful for the inspection of the topography of the sample surface.

If the SEM is equipped with an X-ray detector, it is possible to perform energy–dispersive X-ray spectroscopy (EDX/EDS).

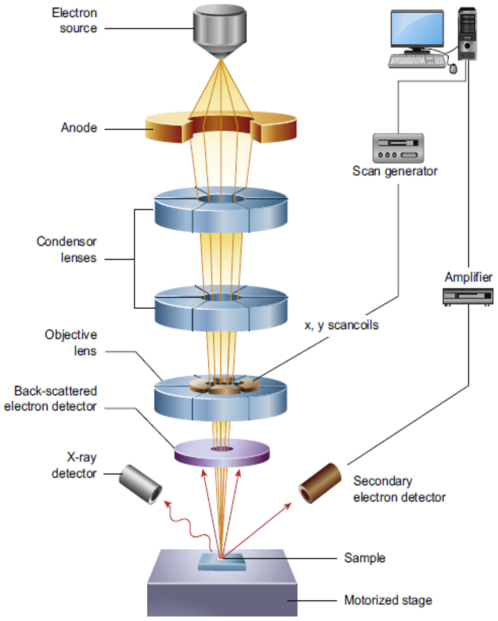

Figure 1.8 Schematic of the core components of a scanning electron microscope. Image taken from reference [Inkson 2016]

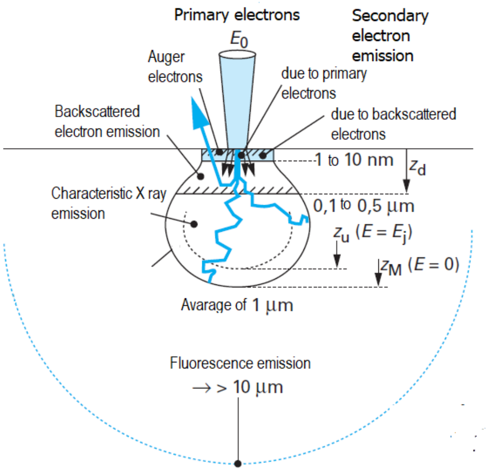

Figure 1.9 Representation of the interaction electron matter in a scanning electron microscope. Where E_j is the ionization energy, Z_d is the full diffusion depth, Z_u useful penetration depth and Z_m the total penetration depth. Adapted from reference[Ruste 2013]

1.3.2 Energy-dispersive X-ray spectroscopy (EDX)

EDX can provide the elemental composition of solids. The high-energy primary electron beam penetrates deeply into a specimen (~1-5 µm). So, the X-rays produced from the interaction of these electrons with atoms deep in the bulk of the specimen can pass through the material and be detected. Therefore, EDX cannot be considered a surface analysis method. Nevertheless, in a few seconds, a qualitative survey of the elements present in almost any sample can be made, and in only a few minutes, enough data can be collected for quantification. The most frequent application is on electric conductor materials, although nonconducting samples can be studied. However, only elements with atomic number greater than four can be detected in optimal conditions.

1.3.3 X-ray diffraction

The X-ray diffraction is used to identify the crystalline phases present in a material. This nondestructive technique relies on the fact that X-rays are a form light, with wavelengths on the order of nanometers. A sample is radiated with an X-ray beam and then the intensities and scattering angles of the X-ray that leave the material are measured.

In materials with a crystalline structure, the scattered X-ray undergoes constructive or destructive interference. In other words, if the diffracted beam is in phase with the incident beam, it can result in harmonic values of the wavelength frequency (Figure 1.10). This constructive interaction is described by Bragg's law:

$$n\lambda = 2d_{hkl}\sin\theta \qquad eq.(1.32)$$

Where: n is an integer, λ the wavelength of the x-ray, d_{hkl} is the interplanar distance and θ the incidence angle of the x-ray beam

This law indicates that a given family of planes produces constructive interference only at a certain incident angle and the interferences are detected in a specific direction.

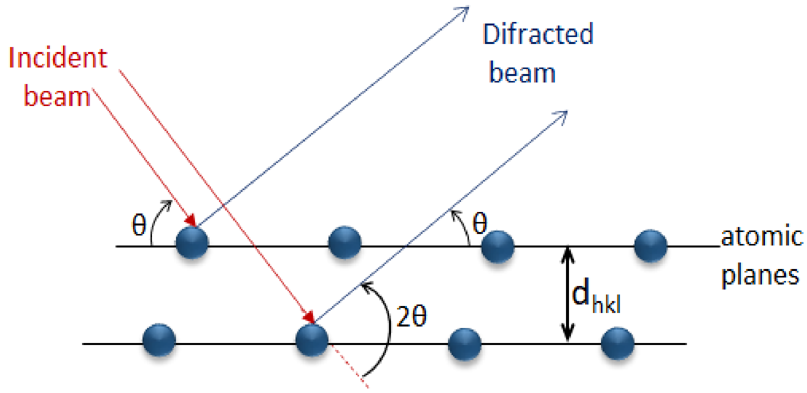

Figure 1.10 Representation of Bragg's law for constructive interferences.

Taking advantage of this law, nowadays the X–ray diffraction as a method to analyze the structure of materials. This equipment consists of an x–ray beam source (a metallic cathode or tube of Cu or Co) and an x–ray detector. In a XRD machine, the sample, the X–ray source and the ray detector are attached to motors, which allows control of the incident and the detection angles.

There are two Bragg–Brentano methods currently used. The first one is a θ–θ mode where the x–ray source and the detector moves simultaneously leaving the sample motionless. The second one is a θ–2θ mode, the source does not move, but the sample and the detector move at an angle θ and 2θ, respectively. Figure 1.11 shows a diagram of these two schemes.

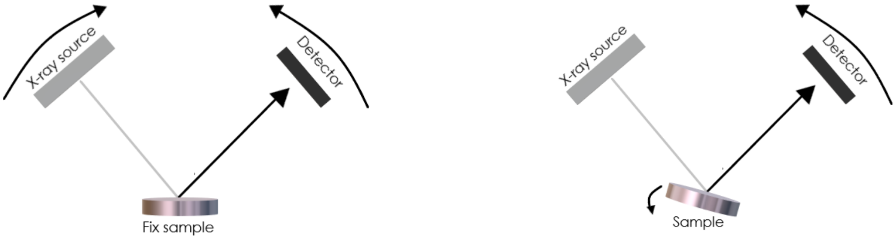

Figure 1.11 Representation of the measurement geometry for the measurements by X-ray diffraction. The image on the left represents the mode θ-θ, the image on the right the mode θ-2θ.

To characterize thin films, there is a special configuration, called razing beam. Here the x–ray beam is kept steady at a very small angle θi while the detector sweeps in θs. This configuration helps to increase the intensity of the detected signal since the volume of the layer that contributes to the diffraction is larger and constant. In the case of films, this configuration also helps to decrease the contribution of the substrate.

1.3.4 X–ray photoelectron spectroscopy (XPS)

X–ray photoelectron spectroscopy is a technique that can provide a comprehensive qualitative and quantitative overview of a surface. This method is based on the photoelectric effect. The bombardment of X-ray induces the ionization of the irradiated material. This ionization is accompanied by photoelectron emissions. These emitted electrons are core level (inner shell) electrons. The energy of these electrons is measured and their values provide information about the nature and environment of the atoms[Ratner 2007]. This process is described by the *eq. 1.34*:

$$KE = h\nu - BE - \phi_s \qquad eq.(1.33)$$

Where:

BE: energy binding the electron to an atom
KE: kinetic energy of the emitted electron
hν: energy of the photon

ϕs: spectrometer work function

The resultant spectrum is a plot of the number of detected electrons per energy interval as a function of its kinetic energy. This characterization technique can identify the elements in the first 10 nm of the surface, on the assumption that the element of interest exists at >0,05atomic %. A schematic representation of an XPS device is shown in Figure 1.12.

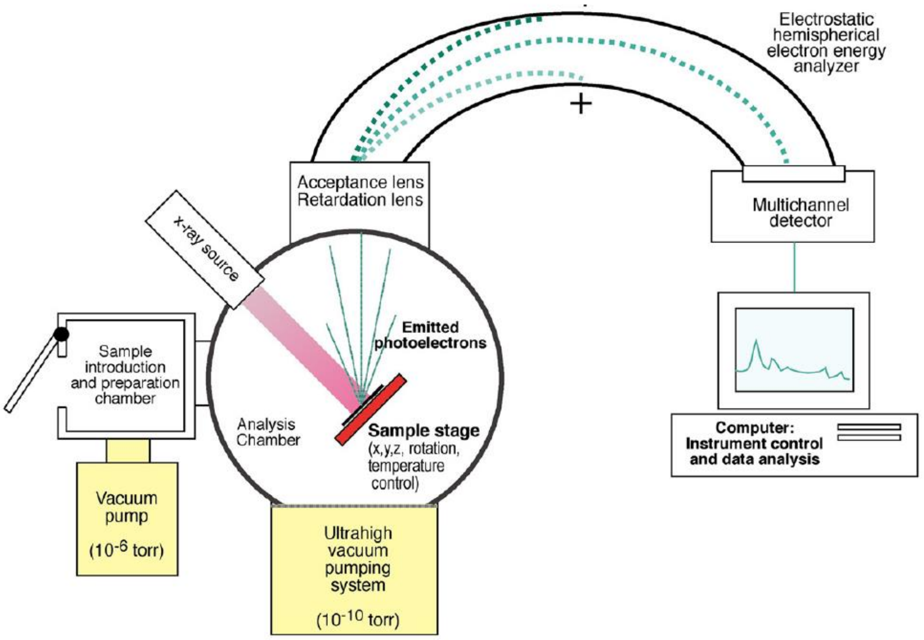

Figure 1.12 XPS device schema [Ratner 2007]

The binding energy depend on the chemical environment of the atom, the first observation of this dependance was made by [Sokolowski, Nordling, and Siegbahn 1958] where a shift of several eV was found between metallic copper and copper oxide. Using the relationship between the binding energy and the chemical environment of the atom, XPS can be used to evaluate the bonds that an atom takes part of. The threshold energy is determined by the energy difference between the core level (initial state) and the lowest energy level in the unoccupied band (the final state). The energies of the initial and final states change with the chemical environment.

1.3.5 Contact profilometry

Profilometry is used to measure the surface topography of a sample which can then be used to determine factors such as surface roughness, coating thickness, changes in volume, among others. These measurements can be made by contact and non–contact profilometry. in the current work, contact profilometry was used to make all the measurements.

Contact profilometry is performed with a diamond stylus point. The stylus takes measurements by electromechanically moving a diamond-tipped stylus over the sample surface while applying a small load. The load is big enough to assure contact with the surface but small enough to avoid damaging the surface. The stylus is linked to a Linear Variable Differential Transformer (LDVT), which produces and processes electrical signals that correspond to surface variations of the sample[Bruker 2011]. After being converted to digital format, these surface variations are stored for display as a two- or three-dimensions graph as shown in Figure1.13.

A contact profilometer can measure small surface variations in vertical stylus displacement as a function of position. A typical profilometer can measure small vertical features ranging in height from 10 nm to 1 mm. The radius the stylus ranges from 20 nm to 50 μm, and the horizontal resolution is controlled by the scan speed and data signal sampling rate. The stylus tracking force can range from less than 1 to 50 milligrams. In the present work a DektakXT stylus profilometer with up to a 4Å repeatability

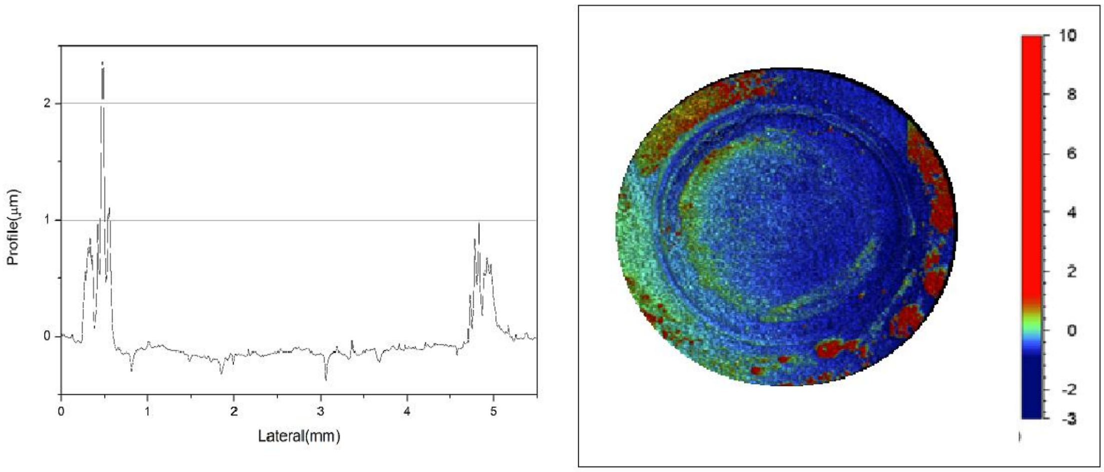

Figure 1.13 To the left a graph of a sample profile, to the right a 3D profile.

1.3.6 Hardness measurement

Hardness implies the resistance to plastic deformation as an indicator of a material’s ability against to resist deformation. To measure hardness, two main methods exist, quasi–static (indentation) and rebound or dynamic. The most widely used is the static hardness test, which can be described as a penetration process, in which the penetration resistance of defined bodies (spheres, pyramids, cones) is determined at a material surface. Depending on the test method, penetration resistance is either determined as the ratio of test force to the surface area of the impression (Brinell hardness, Vickers hardness) or as the remaining depth of penetration of the penetrating body (Rockwell hardness).

Generally speaking, indentation methods consist of a point that applies a load over (some newtons) to the material, leaving a mark on the surface. Such indentation mark is measured (depth or diameter), the size value is then used to calculate the hardness of the material.

When one works with bulk materials many of the indentation methods perform well, but when working with thin films it is better to use micro or nanoindentation methods so that the influence of the substrate can be neglected. To neglect the influence of the substrate the indentation depth should not exceed 10% of the thin film thickness. To estimate the hardness values of films by micro indentation several methods exist, such methods consider different properties of the material involved and the geometry of the indentation mark. Nowadays, nanoindentation has become a standard technique for the determination of the hardness and elastic properties of films. Nevertheless, controversy has arisen when such methods are used on coatings to measure the tribological properties since the low indentation depths only represent the hardness of the first few nanometers of the films. Such material is commonly removed at the beginning of the tribological test during the running in period. Hence, for the present work micro-indentation was the elected indentation method.

1.3.6.1 *Micro-indentation test and composite hardness*

The estimation of hardness by micro-indentation is characterized by applied loads (L) in the range of $L < 2$ N and penetrations depths (h) < 0.2 μm, depending on the hardness of the sample [Broitman 2017]. The two most employed tests in micro-indentation are Vickers and Knoop. Such indentation tests use a diamond indenter with a pyramidal shape. Figure 1.14 shows a diagram of indentation marks for Vickers and Knoop micro-indentation test. In general, the diagonal (d) corresponds to 30.5 times h for Knoop and ~7 times h for Vickers.

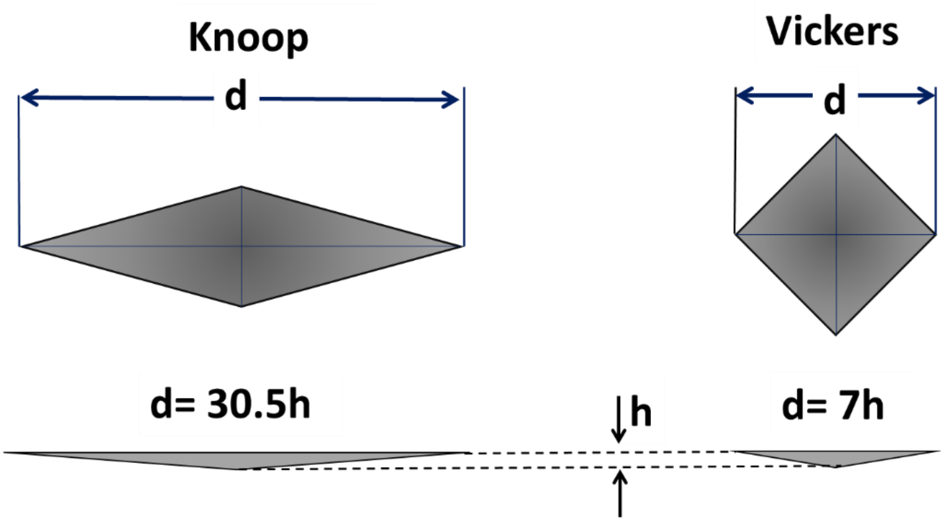

Figure 1.14 Schematic comparison of Knoop and Vickers micro-indentations [Broitman 2017]

When measuring the hardness of films by micro indentation it has been observed that the final estimated value will depend on the obtained indentation size. The larger the indentation size is, the closest it is to the substrate value. Such a phenomenon is known as the indentation size effect (ISE)[Puchi-Cabrera, Staia, and Iost 2015; Lesage et al. 2006]. Hence the observed hardness value corresponds to a composite hardness (H_C).

In general, it is considered that H_C is given by a simple law of mixtures (eq. 1.34) which involves the substrate hardness (H_S) and the film hardness (H_F).

$$H_C = H_s + \alpha(H_F - H_s) \qquad eq. 1.34$$

Where the coefficient α is associated to the contribution of the film. Such coefficient varies from author to author but Lesage et al defined it as a function of the film thickness (t)and the indentation diagonal (d). Rewriting eq. 1.34:

$$H_C = H_s + f\left(\frac{t}{d}\right)(H_F - H_s) \qquad eq. 1.35$$

Since the hardness varies with ISE, hence with the hardness. The variation of d as a function of the applied load (P), when expressed as natural algorithms of the values, presents a linear tendency. Hence, f can be defined as:

$$f = \left(\frac{t}{d}\right)^m \qquad eq. 1.36$$

Where m corresponds to the slope of the linear regression for the logarithmic graph of the indentation diagonal as a function of the applied load, ln d (ln P). Such linear regression will be expressed as:

$$\ln d = m \ln P + b \qquad eq. 1.37$$

Under these conditions H_C can be expressed by the general relation:

$$H_C = \frac{(1-f)}{\left(\frac{1}{H_s} + f\left(\frac{1}{H_F} - \frac{1}{H_S}\right)\right)} + f\left(H_s + f\left(H_f - H_s\right)\right) \qquad eq. 1.38$$

Such expression can be rewritten as a polynomial relation in terms of H_F that allows the calculation of the film hardness which corresponds to the positive root of the equation:

$$A_p H_F^2 + B_P H_F + C_P = 0,$$

$$\text{with} \begin{cases} A_P = f^2(f-1) \\ B_P = (-2f^3 + 2f^2 - 1)H_s + (1-f)H_C \\ C_P = f H_C H_S + f^2(f-1)H_S^2 \end{cases} \qquad eq. 1.39$$

1.3.7 Scratch test

The scratch test consists of a point contact with the sample where an increasing load is applied during the movement of the point over the surface of a coating (Figure1.15). This test generates increasing stress to the surface, this will show specific regions of damage (at critic loads) that can be seen with an optic microscope[Berthout, Randall, and Randall 2017]. Among the visible damage, it is possible to recognize if the film is detached from the surface or if it breaks within the film.

The specific type of damage depends on the mechanical properties of the film and the substrate. When an increasing load is applied to a film there will be elastic and plastic deformations will occur, then the substrate will also be deformed and finally at higher loads fracture of the coating and detachment can occur. Commonly a first critical load charge (Lc1) is when the first cracks are observed, a second critical load (Lc2) is when cracks are continuously observed and the third critical load, (Lc3) is when spalling or detachment of the coating is first seen. These critical loads depend on intrinsic and extrinsic parameters of the film-substrate system and the counter body used. As follow:

- Intrinsic parameters of the film

    - Substrate properties: hardness, elastic modulus, thermic expansion coefficient, and roughness are also linked to residual stress over the film.
    - Film properties: hardness, elastic modulus, residual stress, roughness, and thickness have a direct influence over the critic load.
    - The friction coefficient and friction force between the point and the film.
- Extrinsic parameters
    - Contact point area
    - Velocity of the point speed
    - Ambient temperature and relative humidity
    - Velocity of application of the load
    - Composition and form of the counter body
    - Wear of the spherical point

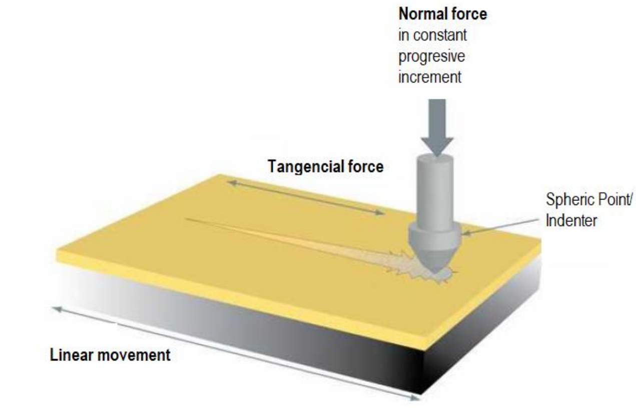

Figure 1.15 Schematic illustration of a scratch test[Berthout, Randall, and Randall 2017].

1.3.8 Coating stress by wafer curvature method.

Thin films can develop large intrinsic stress during their growth process. The magnitude of such stress can exceed the tensile strength of the bulk material. A way to estimate such intrinsic stress is by the wafer curvature method. This nondestructive method is widely used to estimate the coating stress. The principle behind the method it to measure the curvature of the substrate before and after deposition of the thin film [Abadias et al. 2018a].

To determinate the average stress in the film ($\bar{\sigma}$) the Stoney equation (*eq.1.40*) is applied. This equation relates the average stress in the film to the change in the measured curvature (κ). This equation can only be employed when the film is considerably thinner than the substrate[Clyne 2001]

$$\kappa = \frac{6\bar{\sigma}(1 - \nu_s)h}{E_s H^2} \qquad eq.(1.40)$$

Here, h is the film thickness, H the substrate thickness, E the Young's Module of the substrate in GPa and ν_s the Poisson's ratio. Multiple techniques have been developed for measuring the wafer curvature, for the present work the radius of curvature was measured, before and after coating by contact profilometry in the center and at quarter of the sample and then calculated applying the Stoney formula.

Chapter 2

Equipment adaptations

This chapter describes the changes, adaptations, and technical work carried out on the apparatus employed for the rf sputtering deposition of the thin films and the tribocorrosion tests. All the described work in the present section was primarily made by the writer of the present manuscript.

2.1 Adaptation of the sputtering machine

Most of the thin films, obtained during the present work, were deposited by rf sputtering magnetron using a MP300S by Plassys, acquired by the LPMC in 1997. Such a system has a cylindrical vacuum chamber with a capacity of three different 3 inches circular targets. Such targets can only be used one at a time.

For the present work, the equipment was powered by an eni power system OEM-6AM-1 power supply. A diagram of the exterior of the vacuum chamber is presented in Figure 2.1. Such a vacuum chamber is connected to a pre-chamber intended to charge and discharge samples into the main chamber. The samples are suspended in a sample holder attached to a rotatory feedthrough in the lid. This feedthrough is intended to move the position of the sample holder over the desired target position. Figure 2.2 shows a top view of the vacuum chamber without the lid; the drawing shows the distribution of targets inside the chamber and the shield attached to the rotatory feedthrough. The tungsten target, the one mainly used target in the present work, was mounted at the back of the chamber in the right-handed support. To ensure a good mechanical, electrical and thermal contact between the target and the target support.

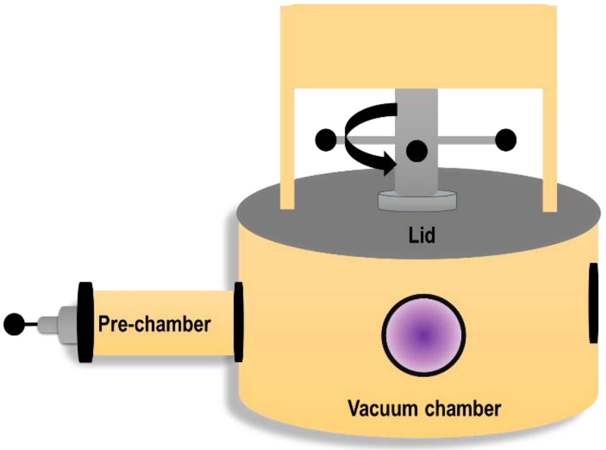

Figure 2.1 Diagram of the vacuum chamber of the Plasyss MP 300S

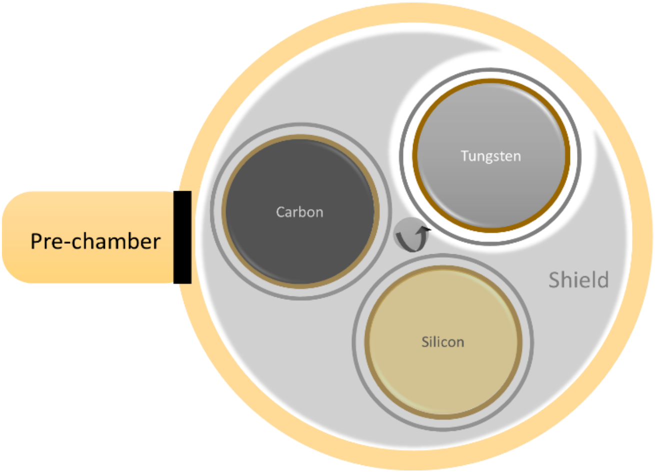

Figure 2.2 Top view of the vacuum chamber without lid

Moreover, Figure 2.3 is a diagram of a transversal view of the vacuum chamber. Originally the Plasyss MP300S was equipped with a sample heater and system to measure the substrate temperature. However, these parts were broken and had not been repaired at the beginning of the present work. Additionally, the manufacturer (Plasyss) informed us that they no longer produced the necessary parts for the system. Hence an alternative sample heater and thermocouple were installed. The choice made for the heating system was a MeiVac Inc. 2” resistive substrate heather. The heater was powered by a CPX200D supply from Aim-TTi. Finally, to measure the temperature of the sample a type k thermocouple was installed. This thermocouple was connected to an external multimeter to give the temperature value. The installation of the thermocouple was not completely satisfactory since the sample holder was attached to the lid of the chamber, and hence, the contact between the sample and the thermocouple point was difficult. Nevertheless, after several attempts, a successful installation of the thermocouple was achieved.

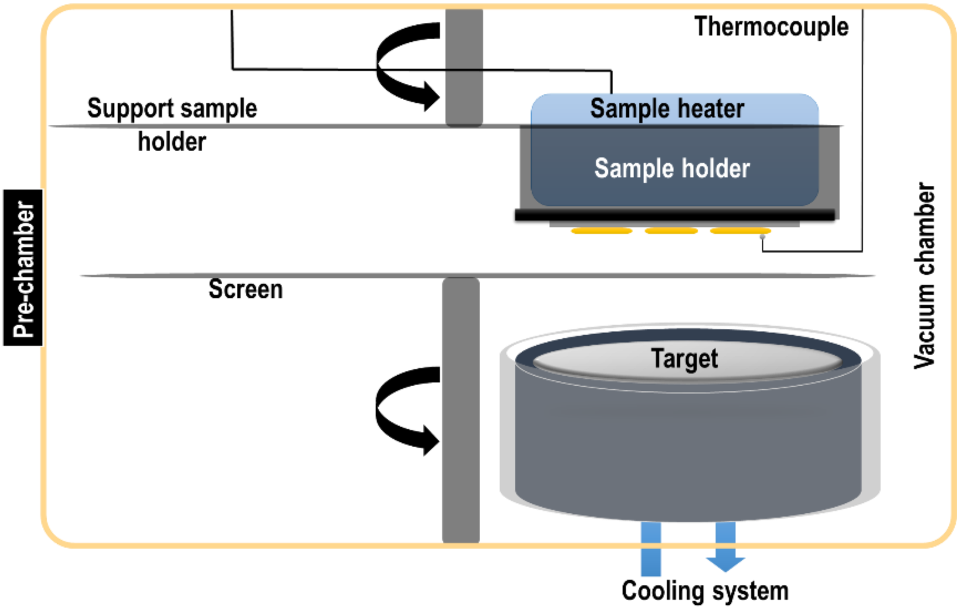

Figure 2.3 Transversal cut diagram of the vacuum chamber.

2.2 Concept, design and set up of a pin on disc tribocorrosion cell.

The tribological and tribocorrosion tests were carried out using an UMT-Tribolab by Bruker. Such systems are equipped with different modules to carry out a variety of mechanical and tribological tests. The manufacturer offers a module for tribocorrosion based on a reciprocating wear test. Nevertheless, the present work was not founded by a specific project and the acquisition of such a module was not possible. A specifical tailored cell was designed for the tribocorrosion work.

2.2.1 Tribocorrosion test apparatus

To perform a tribocorrosion test, the test equipment must allow control and monitoring of the mechanical and electrochemical parameters [Mathew et al. 2011; López-Ortega, Arana, and Bayón 2018; Mathew et al. 2009a]. An alternative to acquiring new equipment and a specific module for tribocorrosion measurements is the construction of a tailored cell. When building such a cell one needs to consider several technical aspects such as (i) geometry and construction of the corrosion cell (appropriate for installation in the existing tribometer), (ii) proper/consistent locations of electrode (iii) possible leakage of the solution/electrolyte, (iv) collection and synchronization of the data from the tribometer and potentiostat, and (v) proper electrical insulation [Mathew et al. 2009a; López-Ortega, Arana, and Bayón 2018]

For the present work, an in house designed and made testing cell, to be used in a UTM Tribolab by Bruker, was develop for discs of 2.5 or 3.0 cm diameter. Different configurations and ways to perform the tribocorrosion tests were explored. Each cell was designed and draw using Solid works. Such cell was print using a Raise 3D printer, and a PLA filament.

Three different models were conceived and tested. The first model shown in Figure 2.4 consisted of a cell with a downer cap to keep the sample in place, and two lateral supports one for the counter electrode and the other for the reference electrode. Such design allowed to be in a fix position for the electrodes and at the same time, the sample was properly isolated. Nevertheless, the type tribological test was limited to reciprocating movement and the screw base resulted in electrolyte leaks. Furthermore, different printing qualities were tested with similar results. Consequently, the cell did not close correctly, and the electrolyte leakage prevailed.

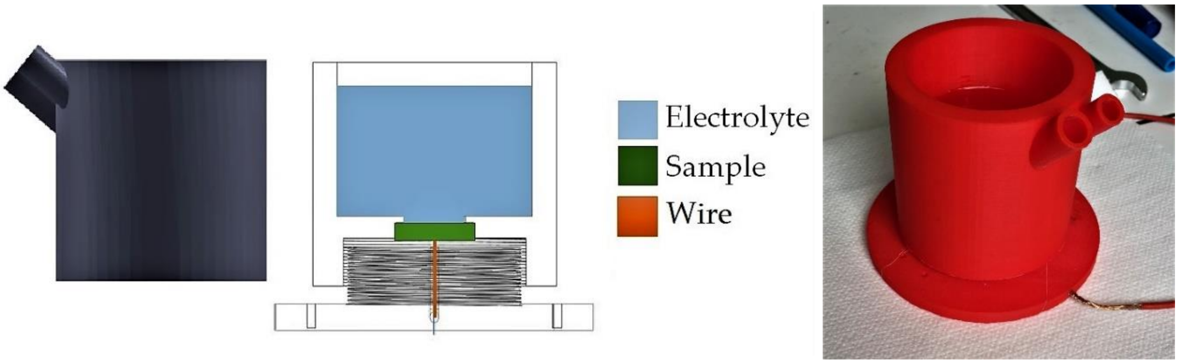

Figure 2.4 Diagram of the tribocorrosion cell for reciprocating test (left) and a picture of such a cell (right).

Another approach was to use as a base the UMT-Tribolab module (Figure2.5). Such a module was designed to be used in lubricated pin on disc tests. Such a module was intended for discs of 3 inches in diameter and the main container was metallic. Hence to be able to use samples of a smaller size and avoid the effect of the container, a cover for the sample support was designed.

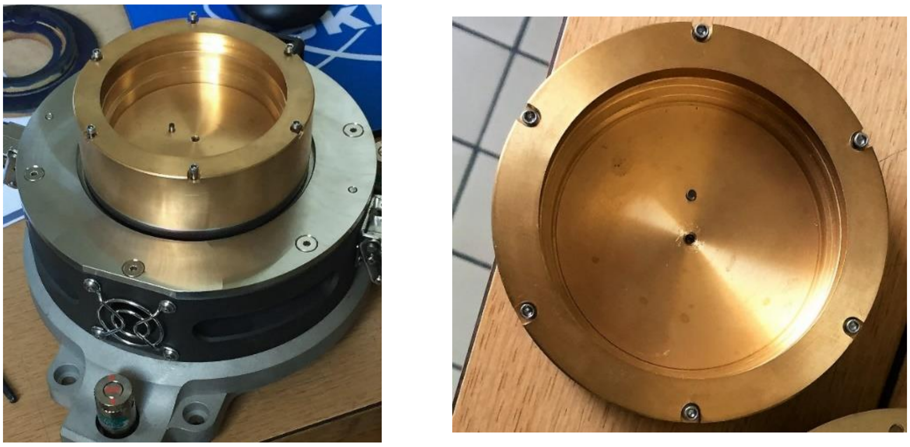

Figure 2.5 Picture of the lubricated pin on disc tests module.

Figure 2.6 shows such a piece, which was attached to the sample container using the screws used to attach the container to the base of the module. To assure that the sample was well fixed PTFE tape was added around the sample. This approach allowed the system to be used to perform pin on disc tests and the leaking problems were diminished.

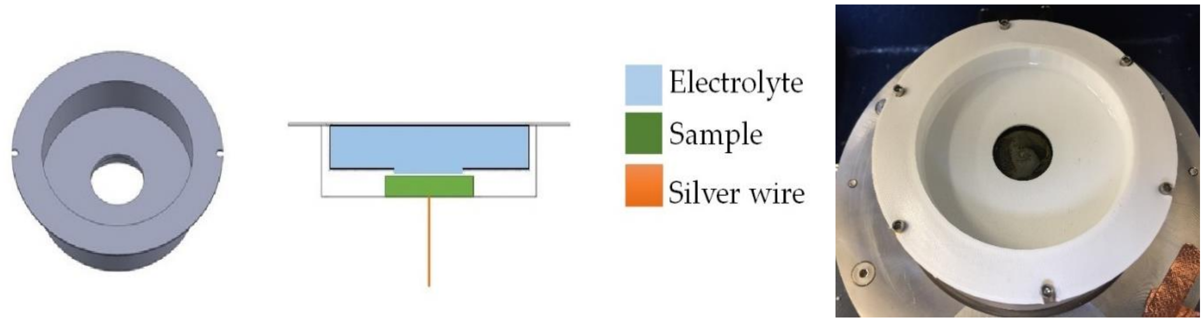

Figure 2.6 Diagram of the cover for the pin on disc UTM tribolab base (left) and a picture of the final cover (right).

With such a piece, tribocorrosion tests were attempted with the experimental setup shown in Figure 2.7. Nevertheless, it was not possible to have direct electric contact with the sample, and the electric current circulated through the entire machine. Since the electric contact was not isolated it was not possible to carried out the electrochemical measurements.

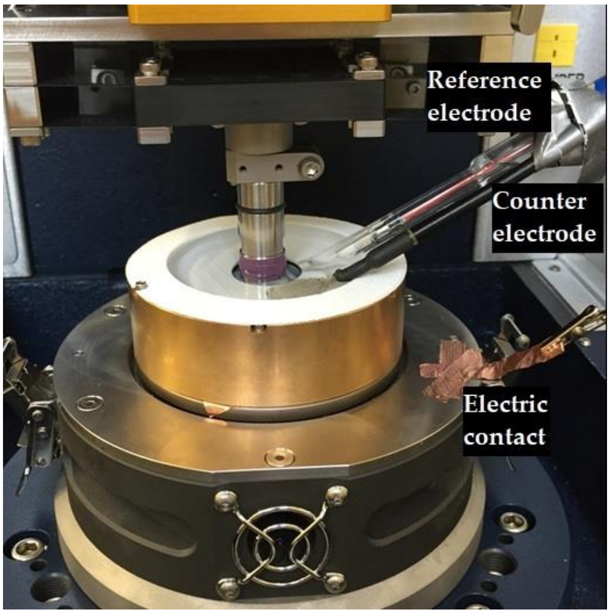

Figure 2.7 Picture of the experimental set up for the module cover.

To ensuring that the electric contact with the sample was isolated from the rest of the system and such that the electrical contact could be sustained as the sample rotated a sliding contact system was developed. To achieve these sliding contact a highly conductive electrolyte was used as a bridge between the potentiostate and the sample to be tested sample. Figure 2.8 shows the diagram of the proposed cell, which worked as a cover as the previously presented one with two levels. The bottom level was built to contain the 'bridge electrolyte" and the top level for the samples and the electrolyte for the electrochemical test. The used 'bridge electrolyte' used for the sliding contact was a 1.0 M aqueous solution of potassium chloride. The sample was attached to a silver wire, and the ends on the wire were submerged in the bridge electrolyte. To make the electrical contact between the sliding contact and the potentiostat a second silver wire was submerged in the potassium chloride and directly connected to the potentiostat.

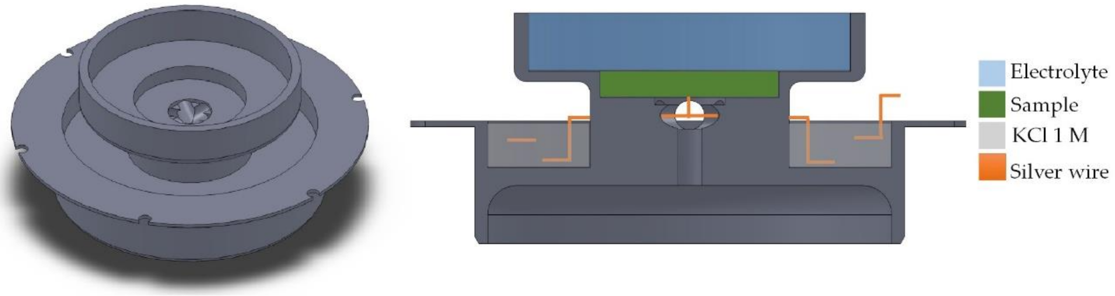

Figure 2.8 Diagram of the tailored tribocorrosion test.

Figure 2.9 shows a picture of the final cell, the counter electrode and the reference electrode were added using external supports to keep the same distance between electrodes. This cell was used during the tribocorrosion test in the experimental part of the present work.

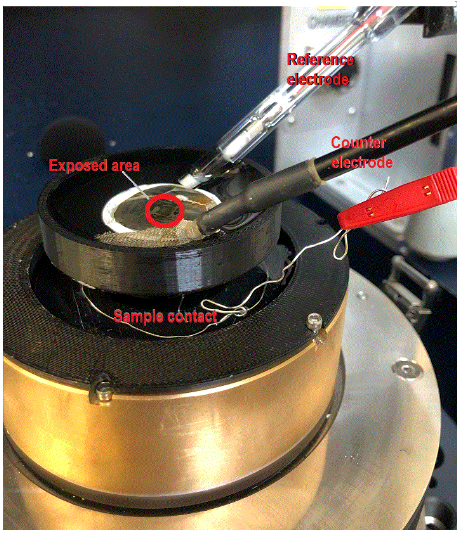

Figure 2.9 Picture of the tribocorrosion cell and the experimental set up.

Chapter 3

Evaluation of the substrates; a tribocorrosion approach

This section presents the wear behavior of AISI D2 and AISI 341 steel at room temperature and relative humidity, the type of wear and the wear rate were assessed with the support of techniques such as contact profilometry, scanning electronic microscope (SEM) and energy dispersive X-ray spectroscopy (EDX). Moreover, the evaluation of the corrosion was explored using electrochemical impedance spectroscopy (EIS). Finally, the tribocorrosion behavior of AISI 341steel was studied by the combination of a pin on disc tests and EIS. We chose the protocol proposed by [Diomidis et al. 2009] because it has been used to characterize different stainless steels uncoated and coated with protective films.

3.1 Steel generalities.

Steel is a widely used alloy and is mainly based on iron and carbon, but it can also contain manganese, sulfur, phosphorus, chromium, among other elements to adjust its chemical, mechanical and physical properties such as corrosion resistance, strength, and ductility[J. D. Verhoeven 2007]. Regularly we speak of steel when the amount of carbon in the alloy is not larger than 2%.

Along with the different compositions of the alloy, it is possible to find it with different phases and crystalline structures. The most common phases of steel are body–centered cubic (bcc) ferrite and face-centered cubic (fcc) austenite, the same as those for pure iron but it is also possible to find cementite and perlite, Figure 3.1 shows a phase diagram for the system iron-carbon, such diagram shows the possible phases of iron and metallic carbides that can be present in a steel at different carbon concentrations and temperatures.

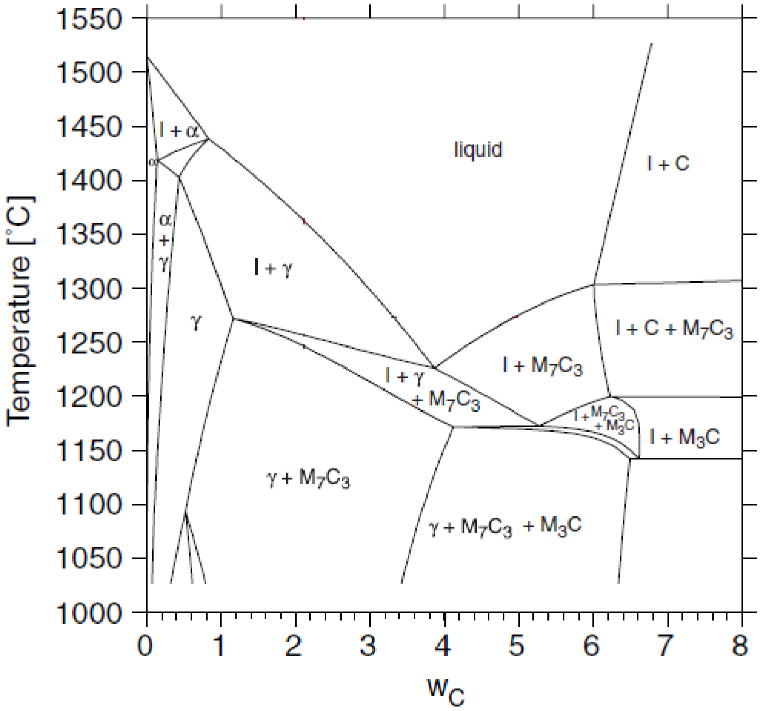

Figure 3.1 Phase diagram iron-carbon for the steel and cast iron regions[Uhlenhaut et al. 2006]

Besides iron and carbon, a wide variety of elements can be found in steel. Such elements are added to modulate its properties. Due to the complexity and variety of compositions several efforts to classify steel have been made. One of the most popular, in USA, is the one proposed by the American Iron & Steel Institute (AISI) which classifies steel in big groups of carbon steel, alloy steel, tool steel, and stainless steel. Within these groups, there are subdivisions based on specific chemical composition, physical or mechanical properties and their use [Paxton 2004; Roussak, n.d.]. The European system is a classification of materials with a sequence of numbers. This classification is given by the norm EN 10027-2. The classification is composed of five digits (X.XXXX) where the first digit indicates the group of material (1 for the group of steels), the following digit indicates if it is or not an alloy or a special type of alloy. For steel, the third digit represents the type of steel, quality, composition, or resistance, while the last two digits correspond to its place on the list. In both classifications, it is possible to find tool steels and stainless steels. Both types of steel are extensively used in a great variety of machining and manufacture operations [Murry 2020], i.e. steel is the most used material in processing material and household utensils in the food industry[Cruz Garcia, Sánchez Moragas, and Nordqvist 2014].

3.1.1 Tool steel AISI D 2/1.2379 – tool steel

Within the group of tool steels we can find high-carbon, high-chromium steels, which present excellent wear resistance, moderate hardness, but poor toughness [Hamidzadeh, Meratian, and Mohammadi Zahrani 2012; Yasavol and Ramalho 2015; Lesyk et al. 2017; Tang et al. 2013; Cho, Lee, and Lee 2015; J. D. Verhoeven 2007], due to their composition they can be considered as stainless or semi-stainless, nevertheless, their corrosion resistance is very limited since most of the chromium content tends to precipitate.

Among the 'tool steels', one can find the AISI D2 steel or 1.2379, according to the EN 10027-2. This steel is commonly used in industrial applications for the fabrication of pieces such as punches, piercing and blanking dies, spinning tools, shear blades, slitting cutters, as well as a variety of woodworking tools.[Tang et al. 2013]. Its reported composition is 1.5% carbon, up to 12.0% of chromium, 0.3% silicon, 0.8% molybdenum, 0.9% vanadium with the rest being iron. Due to its composition, such steel is found regularly as cementite in a tetragonal body-centered crystalline structure (Figure 3.2a). In general, it is heat–treated with two tempered processes to increase its hardness, this heat treatment will change the crystalline structure to a face-centered cubic structure (austenitic phase, Figure 3.2b). Moreover, depending on the heat treatment conditions metallic carbides of different sizes can be formed. In particular for the AISI D2 steel it is possible that Cr, Mo, and V form metallic carbides. The modification of the crystalline structure of the steel and the size of the carbides in the steel can highly impact the overall hardness of the material [Abdul Rahim et al. 2018].

Regardless that this alloy has good mechanical properties, the lifetime of pieces and accessories fabricated with AISI D2 steel are affected by the evolution and type of work conditions in industrial processes. For example, pieces manufactured from AISI D2 steel are used as chuck and rolls in the process of canned food production, where liquid and vapor from the products being canned can come in contact with the pieces[Yam 2009; Shan 2016]. This environment can negatively impact the performance of the pieces and reduce the lifetime. A reduction of the useful lifetime of the pieces impacts the energy and the consumptions of spare parts consumptions. Therefore, one is looking for new technologies that can enhance the lifetime[Ramírez et al. 2012; Díaz-Guillén et al. 2013].

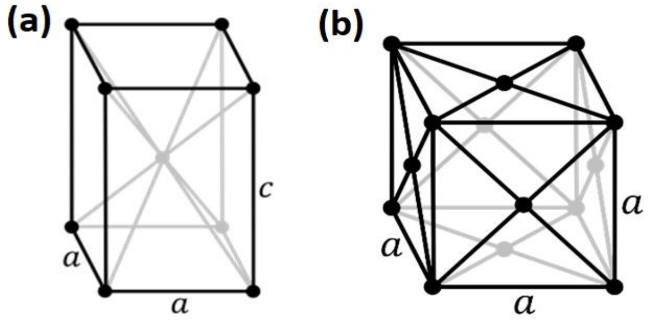

Figure 3.2 (a) Example of a body centered tetragonal crystalline structure, structure of the cementite. (b) example or a face centered cubic crystalline structure, crystallune estructur which coresponds to austenite.

To extend the useful life of pieces such as rolls, some films (TiN, TiC, Cr plating) are currently used to enhance the mechanical performance (reduction of the wear rate) with up to 31 GPa of hardness[Imeta Srl 2018]. Most of the work on the improvement of AISI D2 steel has been focused on its mechanical properties[Ramírez et al. 2012; Díaz-Guillén et al. 2013; Novak and Polcar 2014; Cho, Lee, and Lee 2015; Hamidzadeh, Meratian, and Mohammadi Zahrani 2012; Lesyk et al. 2017; Tang et al. 2013; Toboła et al. 2017; Bourithis, Papadimitriou, and Sideris 2006; Yasavol and Ramalho 2015]. Nevertheless, studies of the corrosion have not been extensively reported [Findik 2014; Gauvent et al. 2006; Sørensen et al. 2009; Fenker, Balzer, and Kappl 2006]. Moreover, the combined effect of mechanical wear and corrosion only has been explored for the coated material [Castillejo et al. 2014; Karakaş 2020].

3.1.2 AISI 431 / 1.4057-stainless steel

Stainless steel was discovered by accident in 1912 in Germany and England. Such type of steel must contain at least 11 % of chromium and have a low carbon concentration, between 0.03% and 1.00%. Stainless steels are well known for their corrosion resistance, such resistance occurs when a thin film (~2 nm) of chromium oxide grows over the alloy surface, such a layer is dense and almost inert, so it is an efficient passivation layer. The AISI 431 steel (EN 1.4057) reported composition of 15-17% Cr, 1.5- 3% Ni, 0-1% Si, 0- 1% Mn, 0.1-0.2% C, 0.04 % P and 0.03% S. Commonly this type of steel has a martensitic phase. Such phases correspond to a body-centered tetragonal crystalline structure (bct)[J. Verhoeven 2016].

Some of the most common properties for this type of steel are high hardness, good wear resistance, fair corrosion resistance, and good performance at high temperatures. Due to this, AISI 431 steel is frequently used for gas turbines, airplane engine parts, laboratory equipment, and aeronautic parts[Paxton 2004; J. D. Verhoeven 2007]. Similar to other types of steel, the final hardness of the material depends on the heat treatment received. Such heat treatment can modify the crystalline structure and the carbides presents on the alloy.

3.2 Materials – substrate's characterization

The present work involves studies of the tribological and electrochemical properties *via* a tribocorrosion study of these alloys. This chapter presents the results of the characterization of the AISI D2 tool steel and AISI 431 stainless steel used as substrates in this study. To verify the tribological, corrosion, and tribocorrosion behavior of the samples a series of tests were performed. Such tests were pin on disc, electrochemical impedance spectroscopy, and coupled pin on disc and EIS tests for the corrosion resistant material.

3.2.1 Sample preparation

Steel discs of 3.0 cm in diameter and 3 mm in thickness were used as substrates in the present work. To assure a similar initial surface for each test, the steel samples were polished up to mirror finishing using either a Buehler-MetaServ 250 at '*Institut Universitaire de Technologie d'***Amiens'** (IUT Amiens) or a Strueurs Tegra Pol-21 polishing machine at the '*Laboratoire de Réactivité et Chimie des solides*' (LRCS-UPJV). The polishing condition were 15 N of load and 300 rpm with different abrasive papers of SiC (from 600 up to 1200) to finish them with a cloth and a solution of Al_2O_3 of 0.1 μm of size. The abrasive papers, cloth and Al_2O_3 solution were provided by PRESI in France.

After the polishing process, each sample was cleaned consecutively with acetone (Fisher chemicals, general purpose grade) and isopropanol (Sigma-Aldrich ≥99,7%) for 10 min using an Elma ultrasonic bath. To finish up each sample was dried out using filtered compressed air.

3.2.2 Roughness

Roughness refers to the variations in the height of the surface relative to a reference plane. The surface roughness of the samples was measured along a standard linear distance using a Dektak XT contact profilometer from Bruker, with a diamond tip of 2.5 μm radial curvature at 3 mg of force. The measurement length was 3 mm crossing the center of the sample. Typical profiles for each of the studied steels are shown in

Figure 3.3. Each sample was measured five times. Each measurement was separated by an angle of 60°.

The software Vision 64 which follows the ISO 4287:1997, was used to calculate the surface roughness. The estimated average surface roughness, R_a, is defined as the arithmetical mean of the absolute values of the profile deviations from the mean value of the roughness profile[ISO 1997]. The average value obtained for the analyzed samples for both substrates was 112 ±33 nm.

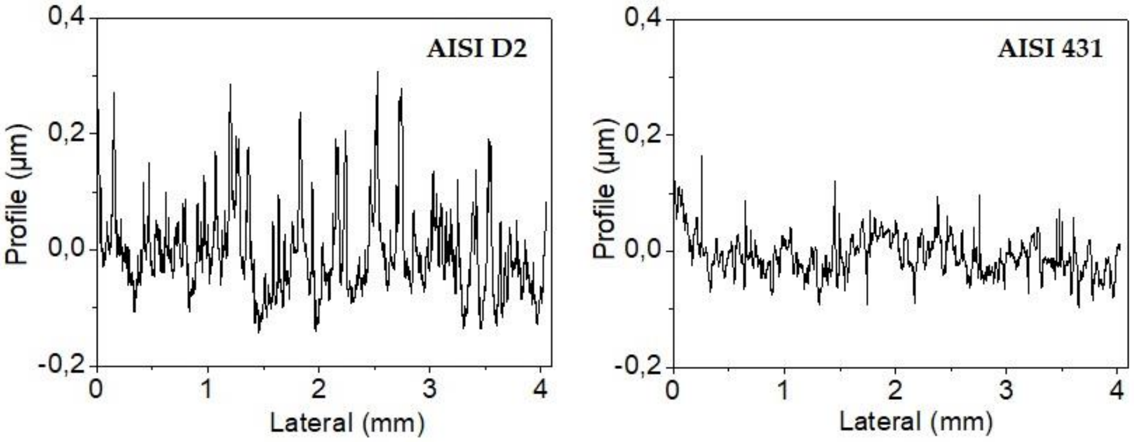

Figure 3.3 Example of a standard profile for mirror polished samples of AISI D2 (right) and AISI 431 (left).

3.2.3 Scanning electronic microscope and Energy Dispersive X-ray Spectroscopy

Once the samples were polished, scanning electronic microscopy (SEM) images and energy dispersive X-ray spectroscopy (EDX) of the substrates were taken. For both steel samples, the images were obtained under high vacuum at 20 KeV. The images and EDX analysis were obtained at the 'Plateforme de Microscopie Électronique' at the UPJV with a Quanta 200FEG microscope with a microanalyzer X INCA Oxford type SDD 80 mm^2.

Figure 3.4 shows an example of a typical SEM image along with examples of EDX mapping for AISI D2 steel. The SEM image shows a relatively smooth surface. The EDX analysis confirmed the AISI D2 steel composition, identifying the following weight percentages: 79.5 % Fe, 13.4 % Cr, 1.25 % Si 1.1 % V, 0.8 % Mo and 4.0% C. The mapping shows the dispersion of each element in the analyzed surface, the colored region represents the measured part where the element was found while the black parts represent an absence of such element. To confirm such uneven dispersion an EDX linear measure was performed. The result of such measurement is shown in

Figure 3.5. The bottom figure shows a graph of the 'counts per second (cps) for each element. This analysis helped to identify the distribution of each element along the measured line, where it was possible to see that there were areas of accumulation of carbon combined with an iron deficiency. Such carbon accumulations, common in high carbon steels help to increase the steel hardness.

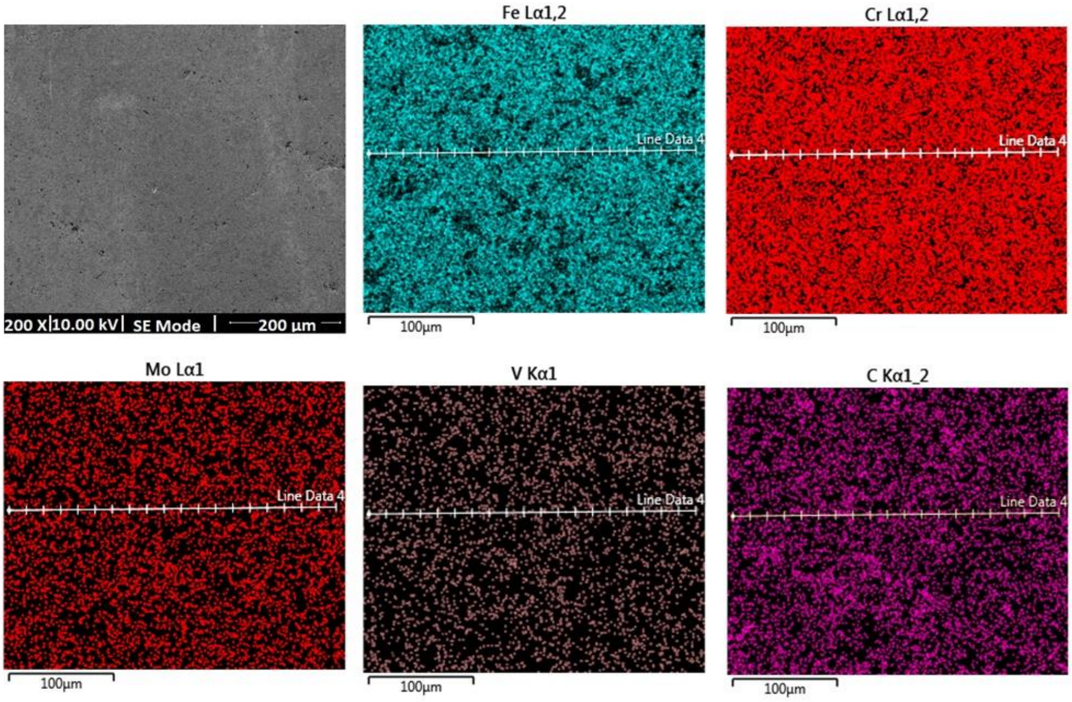

Figure 3.4 SEM micrography and mapping EDX of an AISI D2 steel sample, each image represents the dispersion of each detected element.

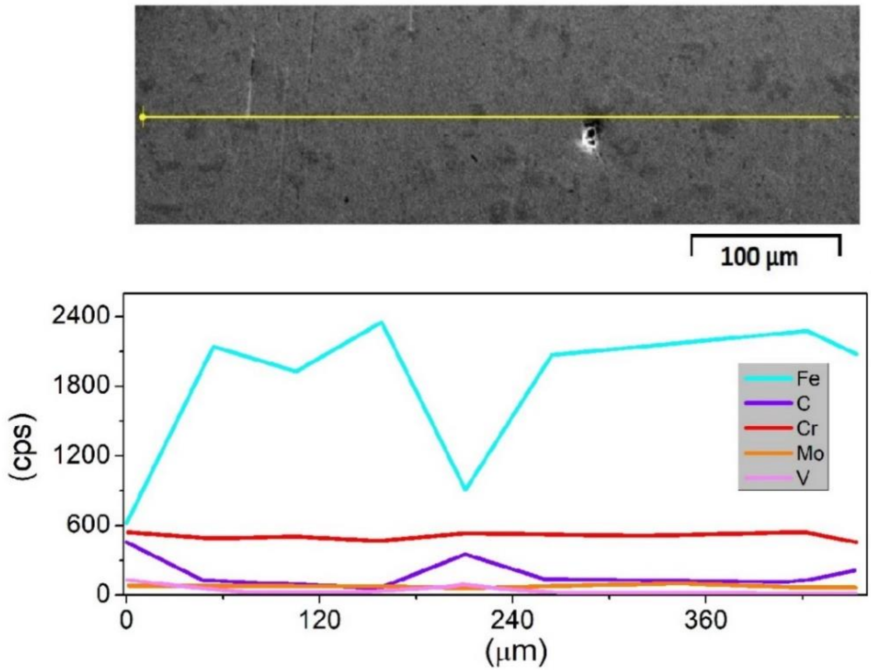

Figure 3.5 Top SEM of the section analyzed by EDX. Bottom counts per second of each element along the analyzed line for AISI D2 steel.

Furthermore, an example of a typical image of AISI431 steel is shown in Figure 3.6 along with the obtained images for EDX mapping. The SEM image exhibits a relatively smooth surface with few defects. The EDX mapping revealed an even dispersion of the elements over the analyzed surface. The detected elements were Fe 76.8%, Cr 17.5%, Ni 2.5%Si 0.4%, and C 2.3%. The amount of detected carbon was larger than expected; and such values are commonly found due to chamber and surface contamination as well as the detection sensibility of this equipment. As for AISI D2 steel, linear EDX measurements were performed over the surface, Figure 3.7 shows an example of such measurements. The graph shows that all the elements are present at similar amounts all along the measured line.

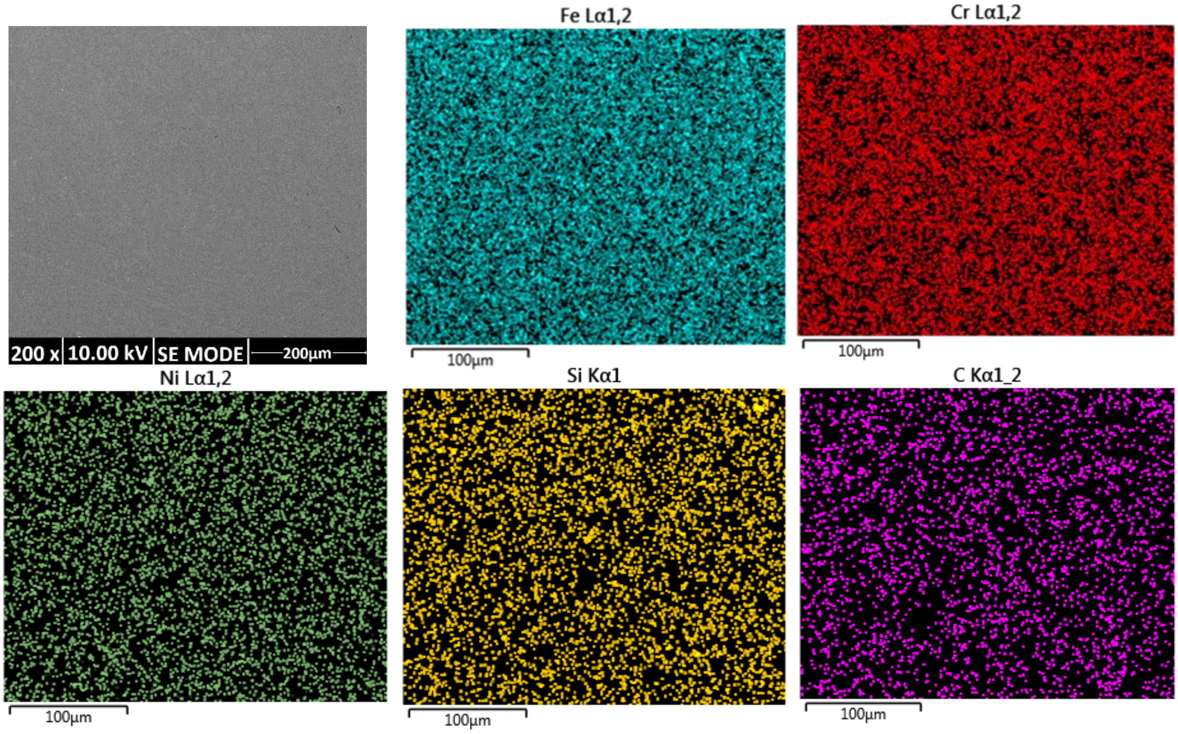

Figure 3.6 SEM micrography and mapping EDX of an AISI 431 sample, each image represents the dispersion of each detected element.

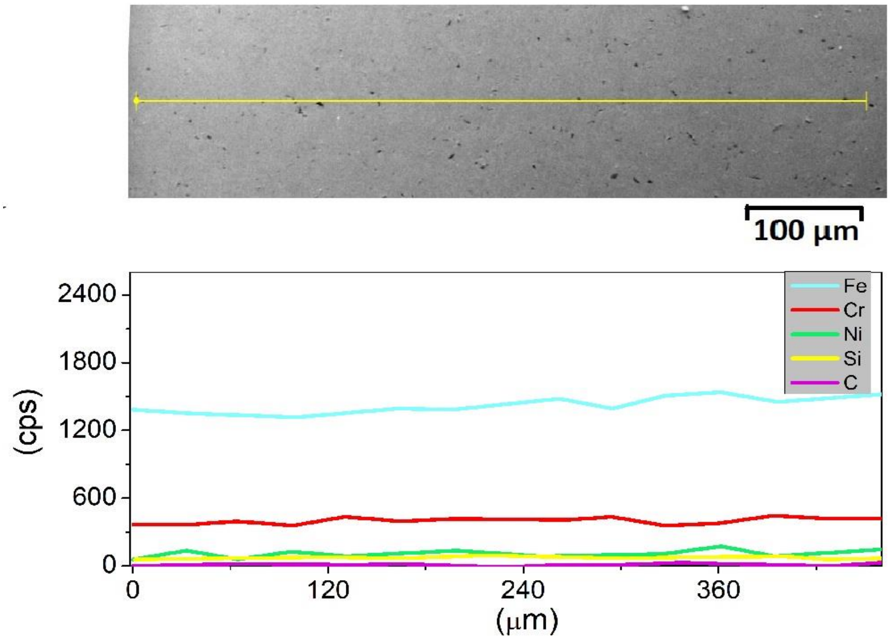

Figure 3.7 Top SEM of the section analyzed by EDX. Bottom counts per second of each element along the analyzed line for AISI 431.

3.2.4 X-ray diffraction

X–ray diffraction measurements were performed over the steel samples at 'Universidad Nacional Autónoma de Mexico', UNAM, with an X–ray diffractometer Rigaku Ultima IV (Cu Kα 1.5406 Å) in the θ-2θ mode. The obtained pattern was compared with a database provided by the PDXL2 software. A sample from each of the types of steel was analyzed and gave similar results. A typical diffractogram is shown in Figure 3.8. The peaks correspond to the α phase of iron[J. D. Verhoeven 2007].

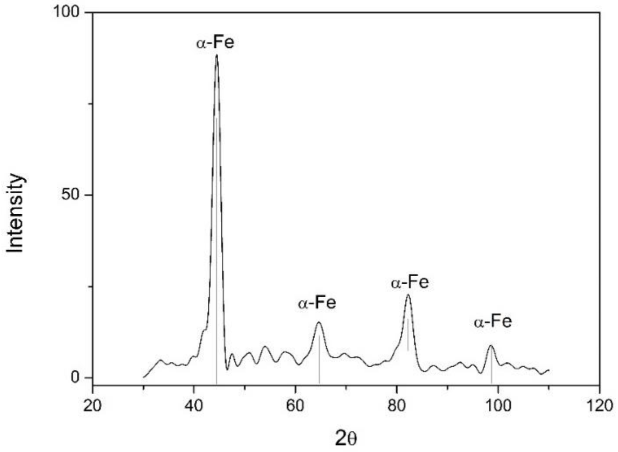

Figure 3.8 Diffractogram of a substrate of AISI D2

3.2.5 Hardness

Hardness is known as the measure of the resistance offered by a material against penetration. One way to measure it is by micro indentation as explained in Chapter1.

Micro-indentation tests were performed over mirror polished discs of AISI D2 and AISI 431 steel using a Nanovea PB1000 Hardness Tester at 5.0N of applied load with a Vickers indenter. An example of a load-indentation depth curve is shown in Figure 3.9. The estimated hardness for each of substrates were 351 (3.4 GPa) for AISI D2 steel and 348 (3.3 GPa) for AISI 431 steel , such hardness values corresponds to those reported for each material[Tang et al. 2013; Díaz-Guillén et al. 2013].

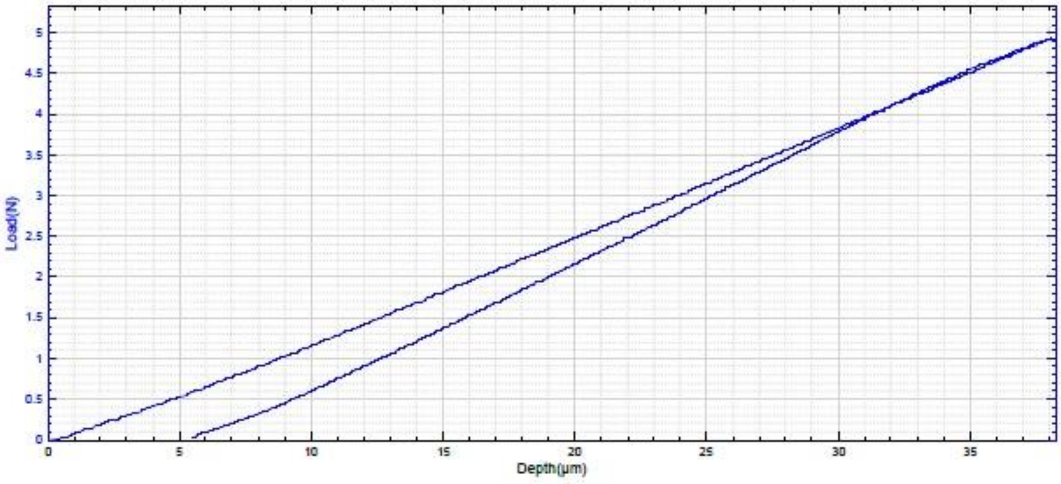

Figure 3.9 Load as a function of depth for a micro-indentation measure of AISI D2 steel at 5N

3.3 Experimental conditions

This section gives the working conditions for the different tests performed for the tribological and electrochemical characterization of the substrates.

3.3.1 Pin on disc tests

The measurements were performed in a UTM-Tribolab by Bruker in a pin on disc machine with a load capacity of 0.5 N to 20.0 N. The counter body for the tests were 12 mm of diameter grade 20 aluminum oxide balls from Redhill Materials. Normal loads of 0.5 N and 1.5 N were applied. The rotation speed was 60 rpm, which is equivalent to 0.02 m/s and for a total length of 72 m.

The UMT-Tribolab takes measurements with the upper sample (pin) fixed to a strain-gauge force sensor which processes mechanical and electrical signals that correspond to the sample's contact behavior. The system processes the signals by converting the mechanical behavior to a digital format.

The contact area and the average pressure in the contact region are given by Hertz's Law, described in chapter one. A summary of the obtained values applying *eq. 1.5* and *eq.1.6* are shown in Table 3-1. The values indicate that an increment of 1N corresponds to an increment of 25% in the average pressure at the contact point.

Table 3-1 Summary of the Hertzian contact area and average pressure of the working conditions.

Applied load (N)	Contact area (mm^2)		Average pressure (MPa)	
	AISI D2	AISI 431	AISI D2	AISI 431
0.5	$2.0X10^{-3}$	$2.1X10^{-3}$	264	239
1.5	$4.2x10^{-3}$	$4.3x10^{-3}$	381	345

3.3.2 Electrochemical tests

As a part of the characterization of the substrate, electrochemical measurements such as open circuit potential (OCP), and electrochemical impedance spectroscopy (EIS) were performed with a PalmSens 4 potentiostat. All measurements were made using a three-electrodes arrangement with a silver/silver chloride (Ag/AgCl) electrode as the reference, a platinum grid as the counter electrode, and the analyzed sample as the working electrode. The measurements were performed on the cell conceived for the tribocorrosion measurements, hence the contact between the working electrode and the potentiate was made through an aqueous solution of potassium chloride. A diagram of such a cell is shown in Figure 3.10.

3.3.2.1 Electrolyte

Citric acid (2-hydroxypropane-1,2,3-tricarboxylic acid) is a weak acid naturally found on several foods. Thanks to its flavor and pH it is frequently used as a protective additive for beverages, jams, jellies, canned food, and even meat[Taylor 2011]. As a food additive, it is classified by the European Union in the list of "other" additives with the number E330, this list compiles acid, acidity regulators, flavor enhancers, firming agents among others [Ekaterina Karamfilova 2016]. The amount of citric acid on the food is not restricted by the EFSA or FDA [IFIC and FDA 2010; FDA/Center for Food Safety & Applied Nutrition 2008]. It can also be used as an antibacterial substance at a pH of around 4 since a large number of bacteria do not survive at this pH value [Taylor 2011; Shan 2016].

Given that citric acid is extensively used in the food industry, an aqueous solution of citric acid at pH 4 was used as the electrolyte for all the electrochemical measurements. The citric acid solution was made using citric acid (NortemBio/ food grade). The acid was weighed using an Ohaus Scout Pro 600 balance, then it was transferred to a 200 ml Hirschmann EM volumetric flask. The desired volume was completed with distilled water. To confirm the pH of the solution, pH measurements were performed with an ezodo mp-103 pH meter.

3.3.2.2 *Open circuit potential and reaction time*

Open circuit potential measurements were carried out for up to five hours, to verify the system's steady-state and determine the characteristic reaction time (t_{react})[Celis and Ponthiaux 2012]. After the OCP measurements an EIS test was performed.

3.3.2.3 *Electrochemical impedance spectroscopy.*

EIS measurements were carried out using the same arrangement as for the OCP measurements in a frequency interval from 10^5 Hz to 10^{-2} Hz with at least three points per decade and amplitude of ± 10 mV vs OCP. The results were modeled using the equivalent circuit approach to determine the corrosion resistance of the system which multiplied by the exposed area of the sample gave the specific corrosion resistance.

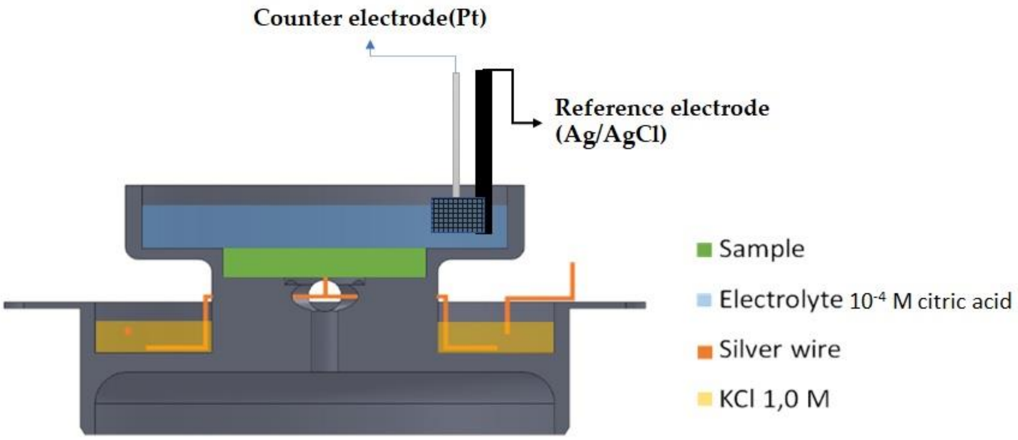

Figure 3.10 Diagram of the cell for electrochemical measurements

3.3.3 Tribocorrosion evaluation

For the passive alloy, the tribocorrosion behavior was evaluated. Given that tribocorrosion is a mixed phenomenon, such evaluation was carried out combining the pin on disc tests and the electrochemical measurements. For such measurements, a three-electrode cell and an aluminum oxide ball were used. Figure 3.11 shows a diagram of the employed cell.

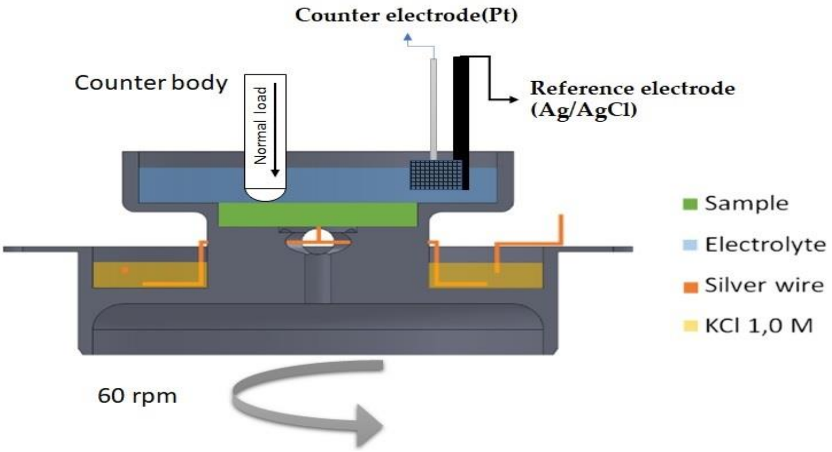

Figure 3.11 Diagram of the cell for tribocorrosion measurements.

3.3.3.1 *Continuous test*

After a steady OCP value was achieved, EIS and pin on disc tests were performed simultaneously. Continuous sliding pin on disc tests at 1.5 N normal load and 0.02 m/s of angular speed were performed, for a total length of 72 m. While the pin on disc test was running, EIS measurements were carried out in a frequency interval from 10^5 Hz to 10^{-2} Hz with at least three points per decade. From such tests, the volume loss and the corrosion current density of the active material were determined. Contact profilometry and SEM measurements were used to assess the final state of the wear surface and the material loss volume. Furthermore, the EIS results were modeled using the equivalent circuit approach.

3.3.3.2 *Latency tests*

For the latency tests, successive identical cycles of active pin on disc and latency were performed until a total length of 72 m was reached. The first part of the cycle corresponds to the active mechanical wear of the surface while the second (latency) allows the wear surface to passivate. The applied normal load was 1.5 N. Figure 3.12 shows a schematic top view of a disc at the different stages of a tribocorrosion latency test, where different areas can be identified during the test. A_0 represents the total exposed area (45 mm^2), A_{act} (4.2 mm^2) the area that corrodes actively and A_{repass} (4.7x10^{-2} mm^2) the area that re-passivates during the latency time[Diomidis et al. 2009].

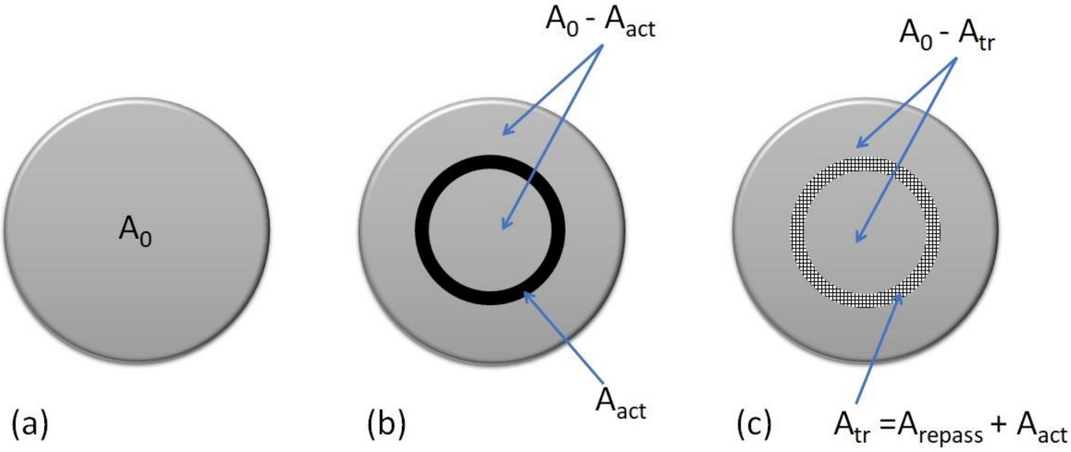

Figure 3.12 Schematic top view of a disc shaped test sample: (a) without sliding, (b) during sliding tests, and (c) during sliding tests at long latency times resulting in a partially active sliding track [Celis and Ponthiaux 2017].

During such tests, the corrosion potential fluctuates hence the corrosion current density cannot be obtained from EIS measurements. Nevertheless, the total volume loss can be used to calculate the ratio which indicates the effect of the material passivation in the mechanical material removal (K_m) and the contribution due to the re-passivation as described on the state of the art.

3.4 Results

The following section presents the tribological and electrochemical characterization of the substrates. The performed test followed the tribocorrosion evaluation protocol described in section 1.3.4.

3.4.1 Pin on disc tests

During the pin on disc test the normal force and the friction force were sensed and then transformed into the coefficient of friction. After the pin on disc test, a circular wear track was obtained on the steel surface, moreover, some changes over the surface of the counter body (aluminum oxide ball) were also examined. The resulting wear track and the contact point in the aluminum oxide ball were analyzed.

3.4.1.1 *Coefficient of friction*

Examples of the temporal evolution of the coefficient of friction for AISI D2 steel at 0.5 N and 1.5 N are shown in Figure 3.13, the yellow line represents the smoothed data using an adjacent average filter for every 500 points. Each of the presented curves shows sharp variations during the first few minutes, such drastic change is common in most of the tribological tests, and it is known as 'break in' or 'running in' period. This period is described as a series of different stages during which small adjustments in the geometry of interacting parts as well as changes in surface roughness occurs [Heilmann and Rigney 1982]. Once the break–in has passed it is possible to consider that the COF of the system is being measured, hence the average coefficient of friction was calculated in the steady state range. The estimated COFs were 0.67±0.04 and 0.53 ± 0.10 at 0.5 and 1.5 N respectively. Moreover, in the steady state range the curves presented a large dispersion, such 'noisy behavior' has been reported for AISI D2 steel and it can be attributed to stick–slip motion during the pin on disc test[Tang et al. 2013]. During the stick phase, the friction force builds up until reaching a critical value. Once the critical force overcomes the static friction, slip occurs at the interface, and

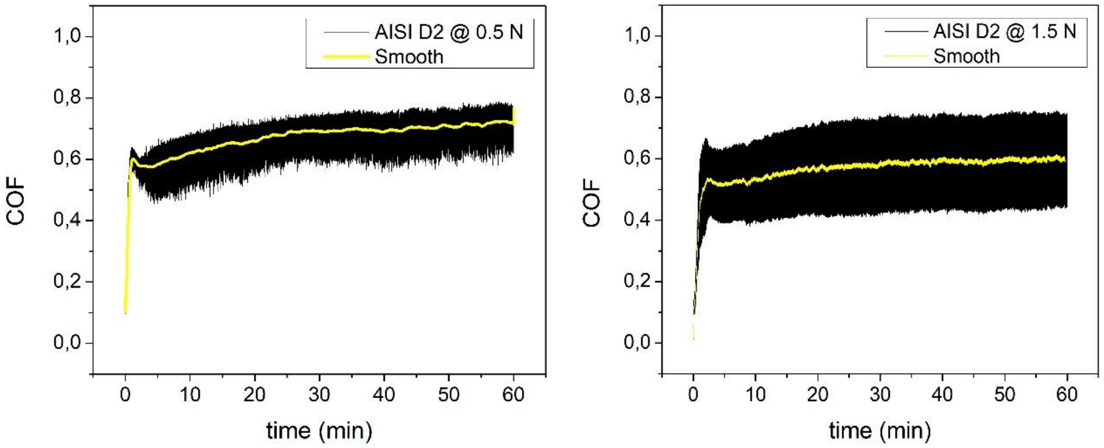

Figure 3.13 Graph of coefficient of friction as function of time for the system alumina (pin) AISI D2 (disc)at 0,02m/s of speed and Left-hand @ 0.5N, right–hand @ 1.5N of load

energy is released so that the frictional force decreases[X. Han 2014; Menezes et al. 2013].

Furthermore, for AISI 431 steel the pin on disc tests were performed at 1.5 N. Figure 3.14 presents the temporal evolution of the COF, the COF presents a curve that shows drastic changes during the first minutes of the tests, breaking in of the test. After the break in period a steady state was achieved. During the steady state a large dispersion was also observed. Such a form of dispersion can be attributed to external vibrations and the type of wear mechanism. The average coefficient of friction was 0.48 ± 0.21.

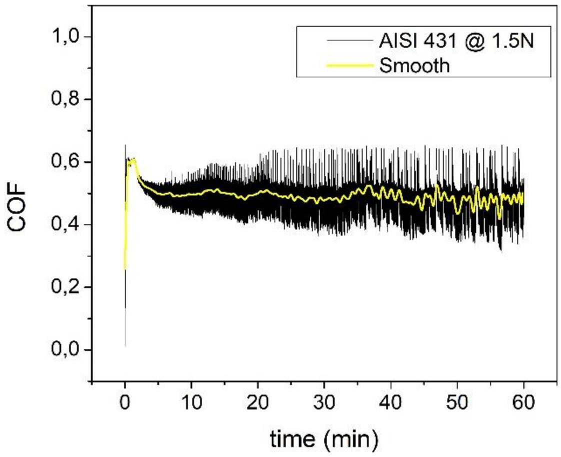

Figure 3.14 Graph of coefficient of friction as function of time for the system alumina (pin)-AISI 431 (disc)at 0,02m/s of speed at 1.5 N of normal load

3.4.1.2 *Wear track analysis by contact profilometry*

In 1953 John Archard proposed *eq. 3.1* at present known as Archard's equation. This equation establishes the proportional relation of the wear volume, V, with the normal load, F_N, and the total sliding distance, L, on a tribological test. The proportionality constant represents the wear coefficient, K, which allows predicting the useful life of a tribological system, as long as the system does not change the wear type [Jiménez and Bermúdez 2011; Kenneth 2007].

$$V = KF_N L \qquad eq.(3.1)$$

To estimate the wear volume, mapping profilometries were carried out with a Dektak XT contact profilometer. The total area analyzed was a square of 7 mm of length with 15 µm of separation between each single profilometry step. The obtained surface 3D map was analyzed with the software Visio 64.

As a result of the pin on disc tests, the average surface roughness of the area close to the wear track changed. The final roughness values for AISI D2 steel were, 245 ±200 and 238 ±370 nm, respectively for the 0.5 and 1.5 N loads. Such change in the surface roughness occurred because over the wear track, we found regions of material accumulation.

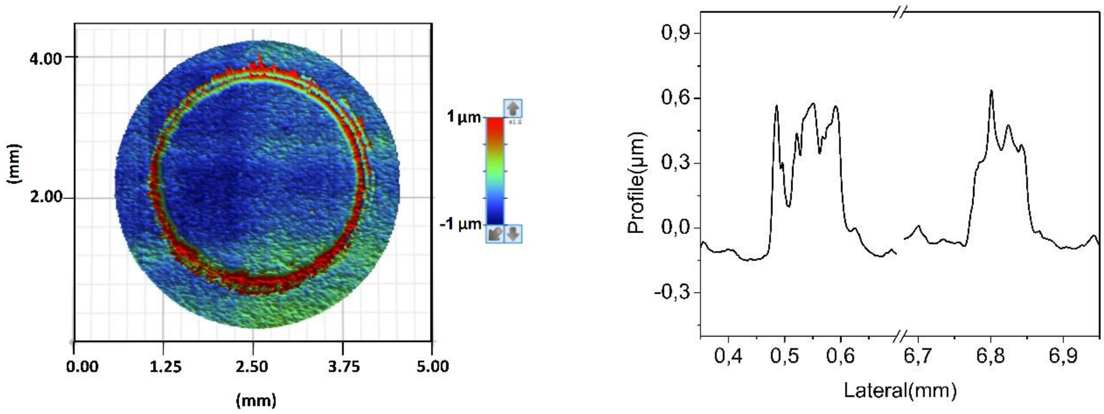

Figure 3.15 Right 3D mapping profilometry for AISI D2 after pin on disc test at 0.5N and room temperature and relative humidity. Left profile of the wear track region. room temperature and relative humidity.

A topographical image of a sample after the pin of disc test at 0.5 N of load is shown in Figure 3.15 along with an example of a single profile at 0.5N, the topographical data was used to estimate the material loss by applying the volume analysis in the region of the wear track. The estimated material accumulated at 0.5N was 2.4x10^{-5} ±1.8x10^{-6} mm^3 giving a wear coefficient of 6.7x10^{-7} mm^3/Nm.

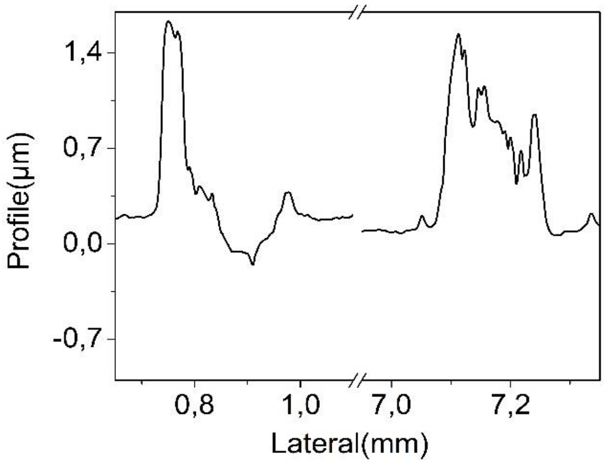

Figure 3.16 Profile of the wear track region for AISI D2 after a pin on disc test at 1.5 N, and room temperature and relative humidity.

Similar measurements were performed over the samples subjected to 1.5 N, an example of a single profile (Figure 3.16) showed that there was accumulated material in the wear track and a smooth surface in the surrounding area. The obtained accumulated material volume was 2.1x10^{-4} ±4.2x10^{-5} mm^3 giving a wear coefficient of 1.9x10^{-6} mm^3/Nm.

Furthermore, for AISI 431 steel the same type of profilometry was performed. Figure 3.17 shows a topographical image of the obtained wear track alongside a single profile. The single profile better illustrates the roughness change over the wear track.

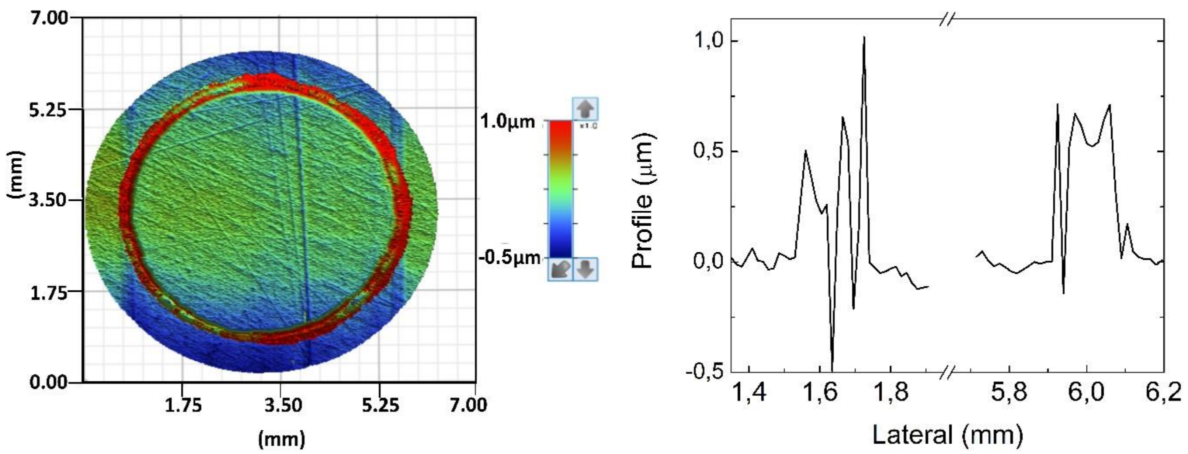

Figure 3.17 Right 3D mapping profilometry of an AISI 431 steel disc after pin on disc test at 1.5N and room temperature and relative humidity. Left profile of the wear track region.

The estimated accumulated material was 1.6x10^{-4} ±1.0x10^{-4} mm^3 giving a wear coefficient, k, of 1.4 X10^{-6} mm^3/Nm.

Additionally, map profilometries were carried out over the surface of the counter bodies. An image of an Al_2O_3 ball is shown on Figure 3.18, such a topographical image

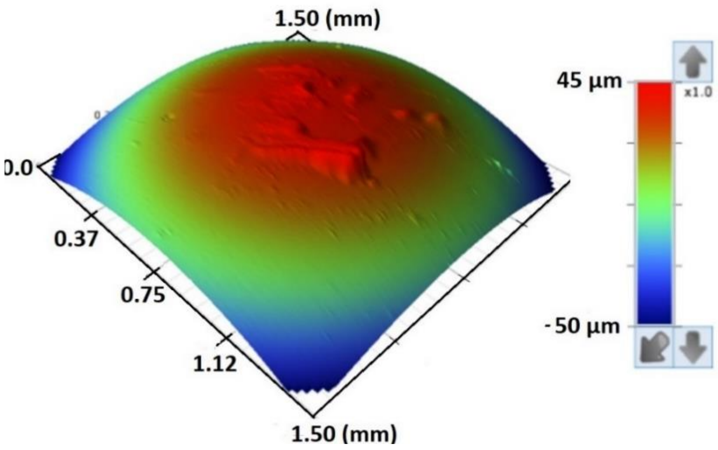

Figure 3.18 Al_2O_3 ball 3D image of profilometry after 60 min of pin on disc test at 0.5 N; in contact with AISI D2 steel.

revealed the presence of accumulated material in the surrounding area of the contact point.

3.4.1.3 *Wear track analysis by scanning electronic microscope and Energy dispersive X-ray spectroscopy.*

SEM images of the steel surface, before and after the pin on disc tests, were taken. the left-handed image on Figure 3.19 shows the surface of an AISI D2 steel disc before the test, while the right-handed image shows the wear track after the pin on disc test at 0.5 N. In each image the regions of accumulated material can be identified along with wear lines in the direction of rotation. The width of the wear track was about 50 μm, a comparable size to the one calculated by the Hertz *eq. (1.3)*.

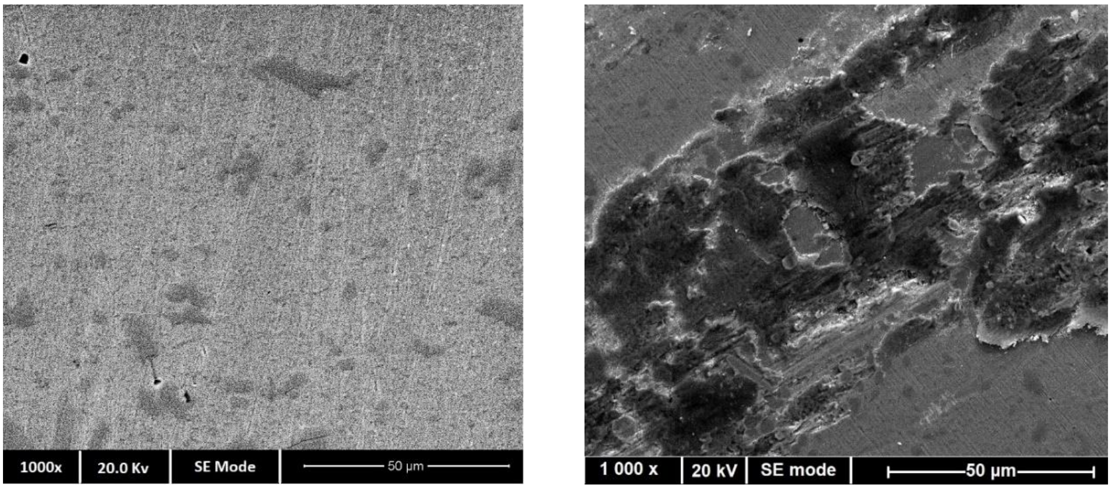

Figure 3.19 -Left- SEM micrography of the AISI D2 steel surface non exposed to wear at 1000 x. -Right- SEM micrography at 1000 x of steel after a pin on disc test at 0.5 N at 0.5 N

Furthermore, SEM images of the wear track using 1.5 N are displayed in Figure 3.20. The image shows a wear track width of around 90 μm, with many lines in the direction of the rotation. Additionally, there was evidence of accumulation over most of the surface.

Similar results were found for AISI 431 steel, a comparison of the surface before and after the pin on disc test is shown in Figure 3.21. Such comparison makes evident the damage produced by the pin on disc test, the region of the wear track presents a different topology to the rest of the surface with a track width of about 100 μm.

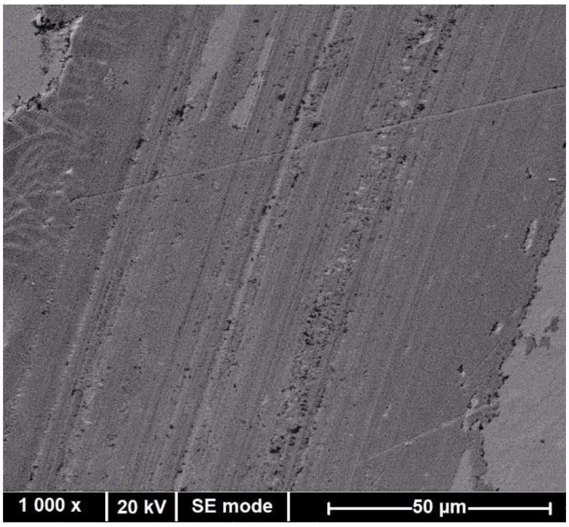

Figure 3.20 SEM micrography at 1000 x of AISI D2 steel after a pin on disc test at 1.5 N

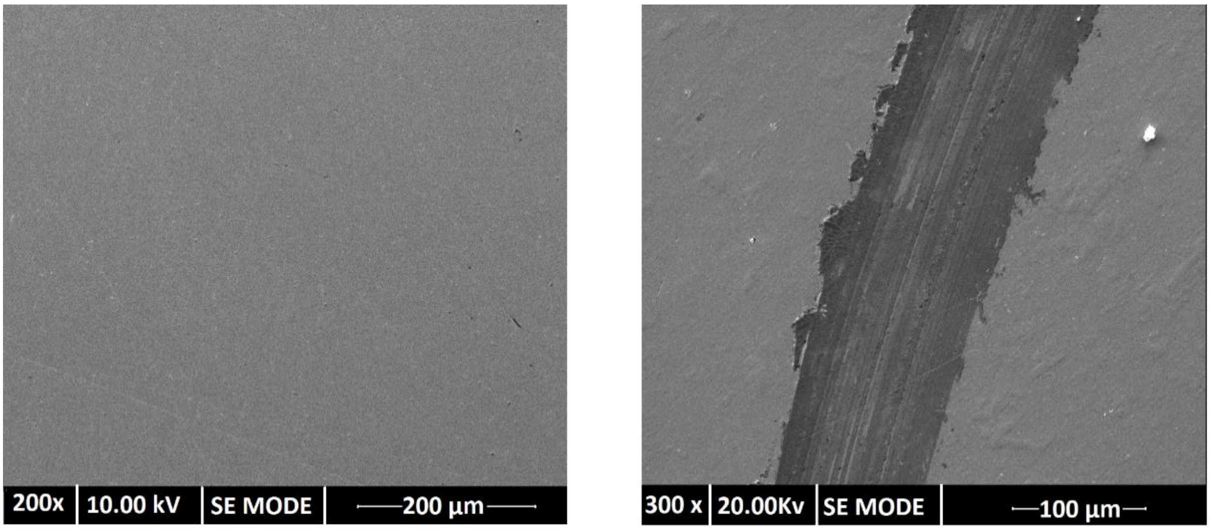

Figure 3.21 -Left- SEM micrography of the AISI 431 steel surface non exposed to wear. -Right- SEM micrography of AISI 431 steel after a pin on disc test at 1.5 N

In addition, SEM images and EDX analysis of the counter body were obtained. Figure 3.22 shows the SEM image, such image presents the contact point (B) with residues of material. The presence of material adhered to the Al_2O_3 surface affects the COF, and it is related to the breaking process. As seen in Figure 3.13, the coefficient of friction changes drastically after approximately 15 minutes. This indicates a change on the contact. The image of the analyzed region and the map of the identified elements are shown in Figure 3.23. Among the elements found in abundance over the surface, there are oxygen, aluminum, and iron. The oxygen and aluminum signals correspond to the ball while the iron corresponds to the adhered material. The amount of iron found in the counter body is relatively small and most of the accumulated material in the surrounding area of the contact point is aluminum and oxygen, indicating that such accumulation manly corresponds to displaced material from the contact point to the surrounding area.

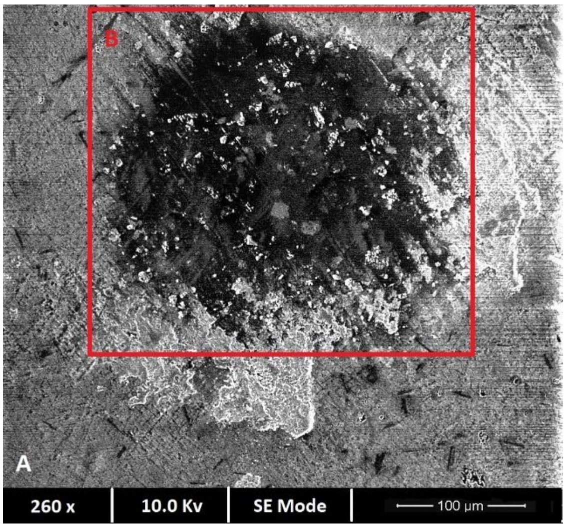

Figure 3.22 SEM image of the contact point of an Al_2O_3 ball after a pin on disc test at 0.5N of normal load in contact with a disc of AISI D2 steel. A corresponds to the surface of the ball not exposed to wear and B corresponds to the region in contact with steel during the pin on disc test.

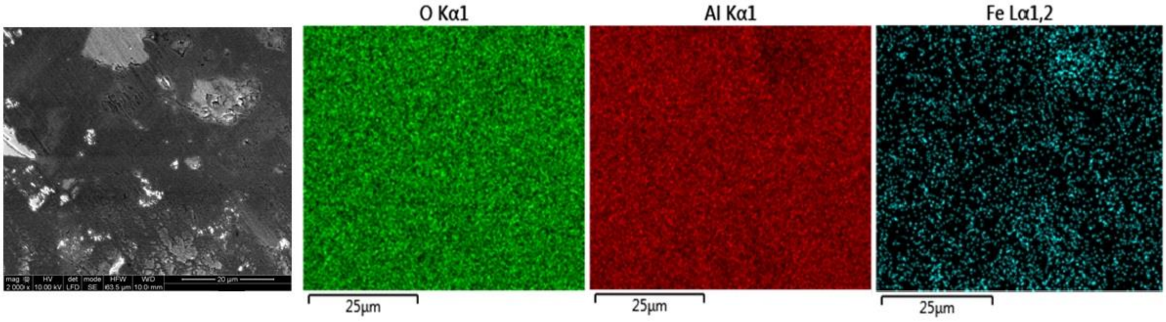

Figure 3.23 Mapping EDS images for a selected region in the counted body after a dry pin on disc test at 0.5 N

3.4.2 Electrochemical tests

3.4.2.1 Open circuit potential and reaction time

Figure 3.24 shows the curve of the temporal evolution of the OCP. The curve presents a sharp decrement at the beginning of the measurement until a steady state was achieved around -0.5 V vs Ag/AgCl. The estimated t_{react} was 28 min.

Considering the composition of the AISIS D2 steel and the pH of the electrolyte it is possible to get an idea of the expected corrosion behavior. Figure 3.25 presents the E-pH Pourbaix diagrams for the elements in the AISI D2 steel. The intersection of the red line in each diagram represents the working conditions of the present study. All these diagrams are referred to the normal hydrogen electrode (NHE). To convert them to the Ag/AgCl system 0.2 V must be subtracted from the values in the graphs. So, the measured value for AISI D2 – citric acid is -0.3 V vs NHE. According to diagrams V, Si, and Fe present a corrosion behavior while Cr, Mo, and C are passive. Due to the amount of chromium in this alloy, and the potential-pH conditions it is expected that the AISI D2 steel might passivate.

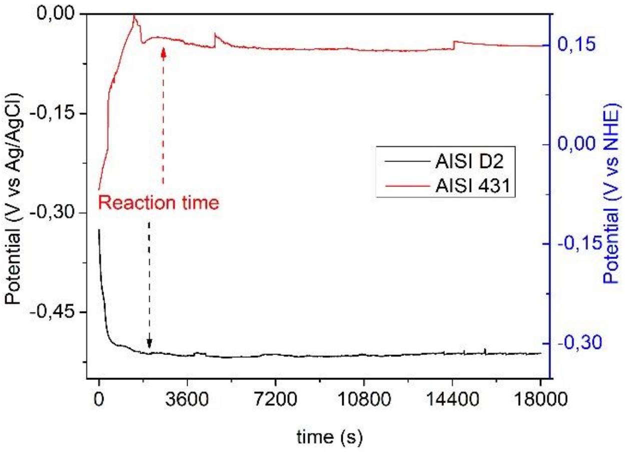

Figure 3.24 Temporal evolution of the OCP for AISI D2 steel in contact with 10^{-4} M

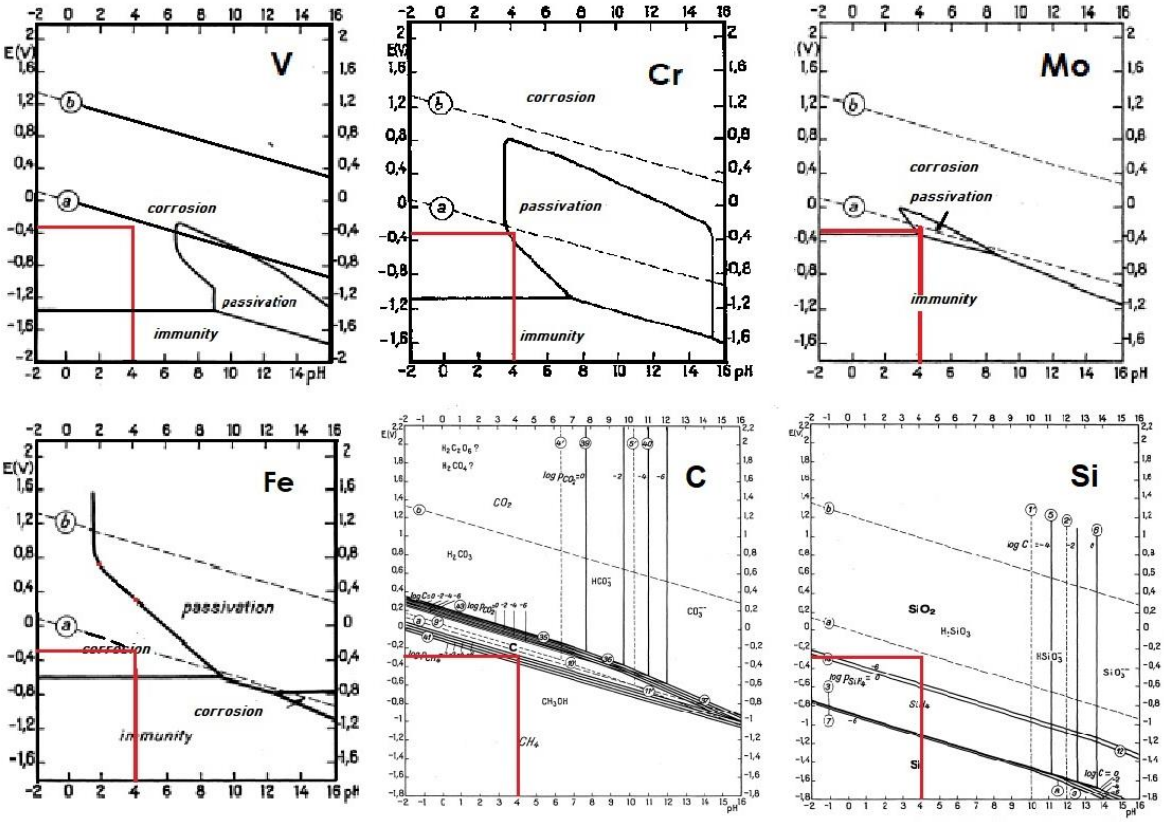

Figure 3.25 E-pH diagrams for the elements on AISI D2 steel, the dashed lines a and b indicates the stability range of water and the intersection of the red lines the current working conditions [Pourbaix 1974].

Making a similar analysis for AISI 431, the OCP steady state value was - 0.05 V vs Ag/AgCl (0.13V vs NHE) with a t_{react} of about 23 min. Figure 3.26 presents the E-pH Pourbaix diagrams for the elements in the AISI 431 steel. The intersection of the red line in each diagram represents the working conditions of the present study, 0.13 V vs NHE and pH4. According to the diagrams, all the elements in the alloy corrodes. Nevertheless, Cr is at the limit between corrosion and passivation, and consideration of the percentage of chromium suggests that the AISI 431 steel might also passivate.

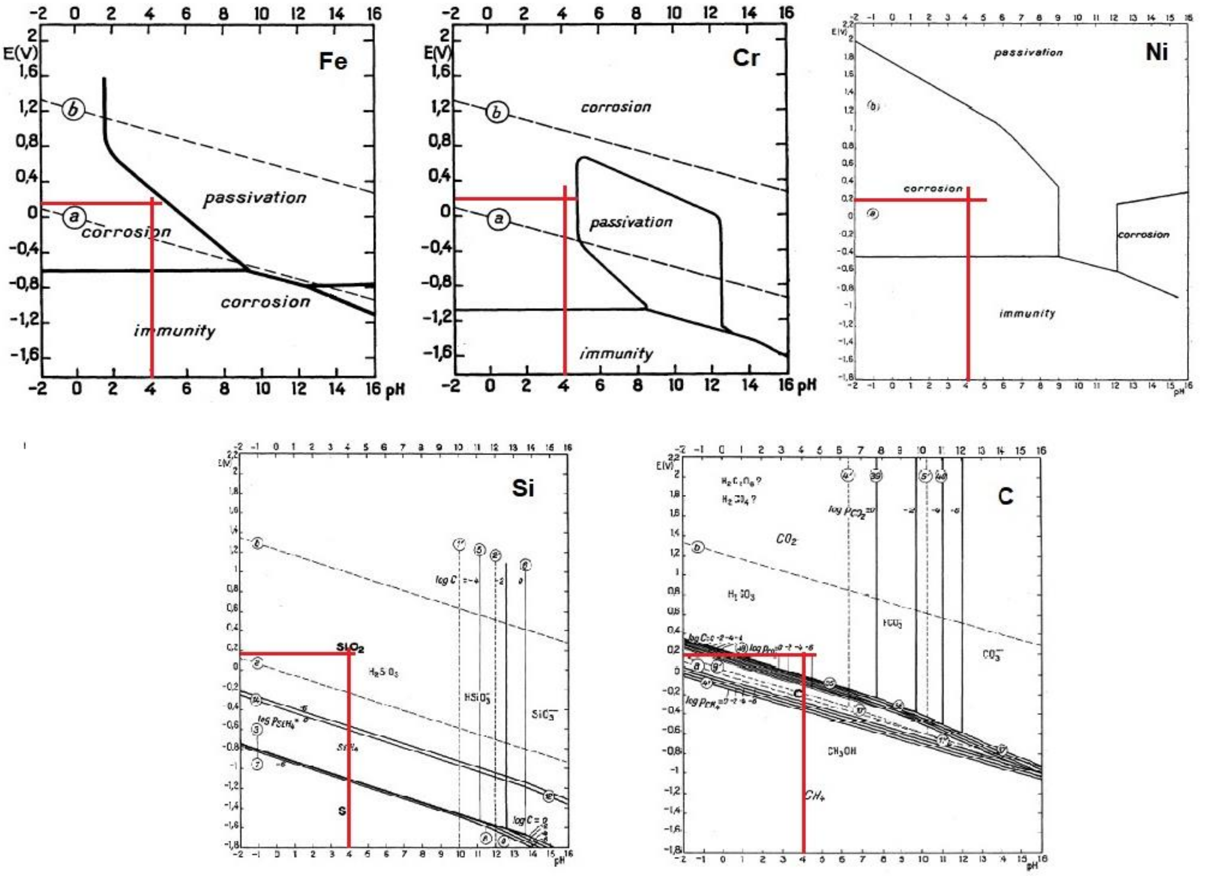

Figure 3.26 E-pH diagrams for the elements on AISI 431 steel, the dashed lines a and b indicates the stability range of water and the intersection of the red lines the current working conditions [Pourbaix 1974].

3.4.2.2 *Electrochemical impedance spectroscopy*

An example of a typical Nyquist diagram and its simulation is presented in Figure 3.27. The diagrams show two semicircles, hence two-time constants, that have been shifted from the origin. Such behavior is commonly found during corrosion processes and can be described by the equivalent circuit shown in Figure 3.28.

The proposed equivalent circuit consists of a resistance R_1 and two RQ parallel circuits. The first RC parallel circuit along with R_1 represents the ohmic resistance of the solution between the working and the reference electrodes. Such behavior is commonly attributed to the geometry of the electrochemical cell and the reference electrode geometry [Edwards et al. 1997; Hsieh et al. 1997]. Finally, in the second RC component, R_3 corresponds to the polarization resistance of the material (R_P); the Q element is a constant phase element (CPE) which describes a non-ideal capacitor when the capacitor phase angle is different from -90°[Walter 1986]. CPEs are generally used to describe surface reactivity, surface heterogeneity, and surface roughness as well as the distribution of the current and potential caused by the electrode geometry and porosity [Montemor and Ferreira 2007]. The Rp value was multiplied by the exposed area to obtain the specific corrosion current (r_P). The estimated value of r_P was 3.3 ±0.1 kΩcm^2, with a chi-square of 0.0052 suggesting a well-adjusted circuit. For a specific corrosion resistance lower than 100 kΩcm^2 the material is considered to be under corrosion [Ningshen et al. 2006; Diomidis et al. 2009], hence AISI D2 steel corrodes in contact with citric acid 10^{-4} M.

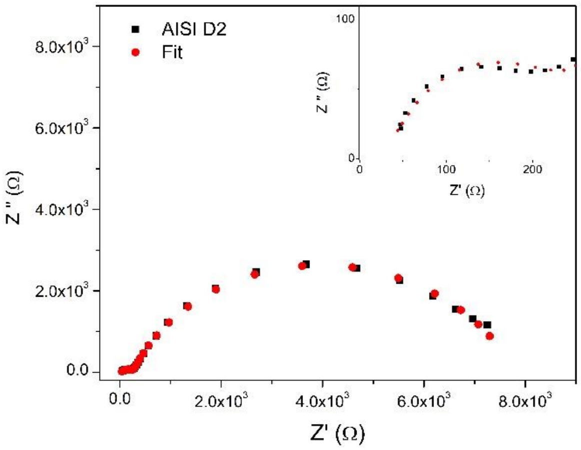

Figure 3.27 Nyquist diagram for the EIS of AISI D2 steel in contact with the citric acid 10^{-4} M solution.

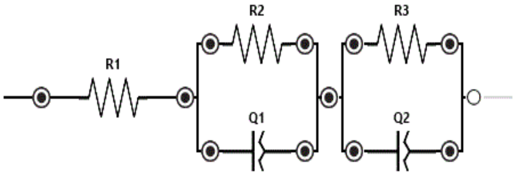

Figure 3.28 Equivalent circuit for the EIS response of AISI D2 steel in contact with the citric acid 10^{-4} M solution.

The corrosion resistance was used to calculate the corrosion current i_{corr} applying the Stern-Geary equation (*eq.3.2*) where B is a term that varies between 13 and 35 mV depending on the nature of the material and the environment. For metallic materials, in acidic environments, B can be considered as 24 mV as suggested by some authors[Mathew et al. 2009b; Diomidis et al. 2010; Celis and Ponthiaux 2012].

$$i_{corr} = \frac{B}{r_p} \qquad eq.(3.2)$$

The estimated i_{corr} was $9.3 \times 10^{-6} \pm 2 \times 10^{-8}$ A/cm^2, a comparable value to those obtained by other authors using different electrolytes [Chen et al. 1999; Sista et al. 2011; Díaz-Guillén et al. 2013]. This type of behavior has been reported for other pH values, due to precipitation of the alloying elements [Chen et al. 1999; Castillejo et al. 2014; Díaz-Guillén et al. 2013]. Furthermore, precipitation of the alloying elements is commonly found in iron-alloys with the cementite phase [Beitz and Kuttner 1994].

In addition, a Nyquist diagram for AISI 431 steel and its simulation are shown in Figure 3.29. The diagram is similar to the results for AISI D2 steel; the diagram presented two time constants, hence, the proposed equivalent circuit consists of two RQ parallel circuits (Figure 3.30), such circuit presents a slight difference from the one proposed in Figure 3.28, due to the electrode arrangement when the tests were performed. For the circuit in Figure 3.30 the first RC parallel circuit represents the ohmic resistance of the solution between the working and the reference electrodes, while in the second RC component, R_2 corresponds to the polarization resistance of the material (R_P); the Q element is a constant phase element (CPE). The estimated value of r_P was 160.6 ±5.0 kΩcm^2, with a chi-square of 0.002 suggesting a well modelled circuit. The r_P value was used to calculate the i_{corr} applying *eq. 3.2*. for AISI 431 the estimated value was 1.5×10^{-7} A/cm^2. The corrosion current and corrosion potential correspond to those of a passive material, hence AISI 431 steel passivates under citric acid pH 4.

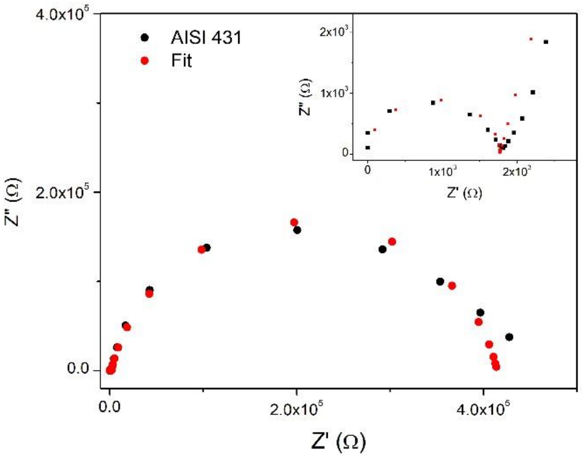

Figure 3.29 Nyquist diagram for AISI 431 steel in contact with the citric acid 10^{-4} M solution.

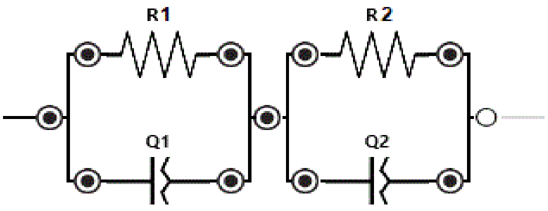

Figure 3.30 Equivalent circuit for the EIS response of AISI 431 steel in the citric acid 10^{-4} M solution.

3.4.3 Tribocorrosion evaluation

3.4.3.1 Continuous sliding

For AISI D2 steel the influence of the electrolyte on the material wear was studied, nevertheless, the tribocorrosion synergy could not be evaluated since it is not a passive material. To evaluate the influence of the electrolyte in the wear of AISI D2, steel pin on disc tests of the steel in contact with the electrolyte were performed. Figure 3.31 and Figure 3.32 show profiles of the wear track region. For the sample tested at 0.5 N, the wear track was difficult to identify since the surrounding area showed considerable damage due to corrosion. However, for the 1.5 N test, the wear track was more evident with a maximum depth of about 800 nm. As a result of the pin on disc tests the surface roughness changed, and the average surface roughness of the areas close to the wear track were, respectively, for the 0.5 and 1.5 N loads, 720 ± 60 nm and 773 ± 90 µm. Moreover, the material volume loss was $2.3x10^{-3} \pm 4.9x10^{-4}$ mm^3 at 1.5 N. In contrast, after the dry pin on disc test a smear accumulation of material was found, therefore it is evident that the damage over the steel surface is modified by presence of a corrosive environment than under normal room temperature and humidity conditions. As mentioned above the surrounding area of the wear track presented significant damage. Such damage made it difficult to correctly identify the wear track and increased the associated error.

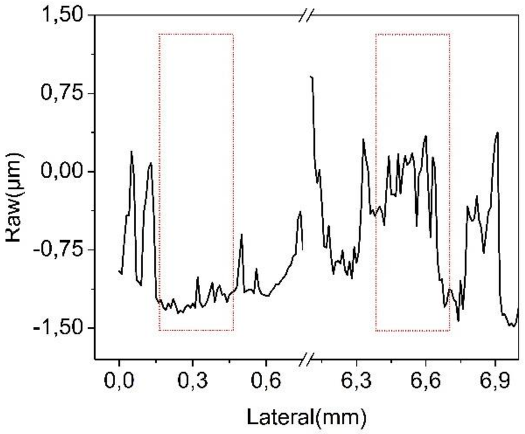

Figure 3.31 Profile of the wear track region after AISI D2 steel after a pin on disc at 0.5 N test in contact with citric acid 10^{-4} M.

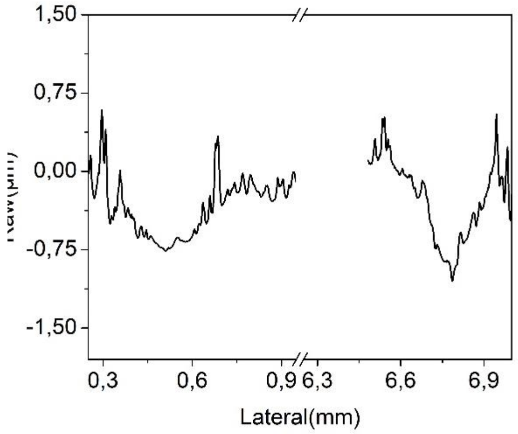

Figure 3.32 Profile of the wear track region after AISI D2 steel after a pin on disc at 1.5 N test in contact with citric acid 10^{-4} M.

In order to evaluate the tribocorrosion behavior of AISI 431 steel, coupled measurements of pin on disc and EIS were performed. As a first approach, the EIS tests were performed under continuous sliding. Figure 3.33 presents the temporal evolution of the COF, such a curve presents strong changes during the first minutes of the test, and this corresponds to the breaking in of the passivation layer that changes to a steady state, after about 20 min. A diminution of the COF occurred in the steady state, and such a change corresponds to the interaction between the counter body and the active material. The average COF in the second steady state was 0.23 ±0.01, a smaller value than the one found for the pin on disc test under room temperature and relative humidity (0.48 ± 0.21). This reduction in the COF can be attributed to the aqueous solution acting as a lubricant, such behavior has been reported for other systems [Karakaş 2020; Wood, Herd, and Thakare 2018; Henry, Takadoum, and Berçot 2011].

Furthermore, the resulting Nyquist diagram for the test under continuous sliding is presented in Figure 3.34. In the diagram, two time constants can be identified. The obtained results were modeled using the equivalent circuit shown in Figure 3.28. Here R_2 represents the polarization resistance R_{ps}, which is the combination of two polarization resistances, R_{act} that corresponds to the area that corrodes and R_{pass} the area that passivates *eq 3.3* [Celis and Ponthiaux 2012]. The estimated R_{ps} value was 65.4 ±6.1 kΩ,

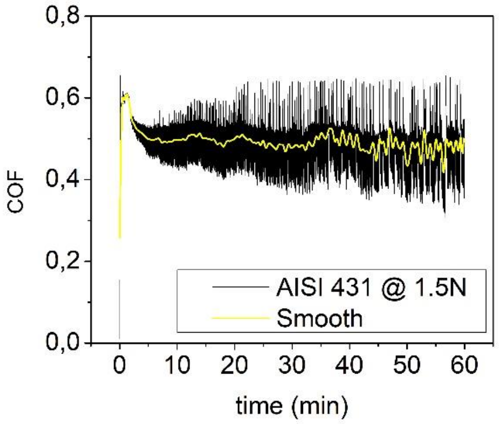

Figure 3.33 Temporal evolution of the COF for the system AISI 431 steel -Al_2O_3 at 1.5N when in contact with the citric acid 10^{-4} M solution.

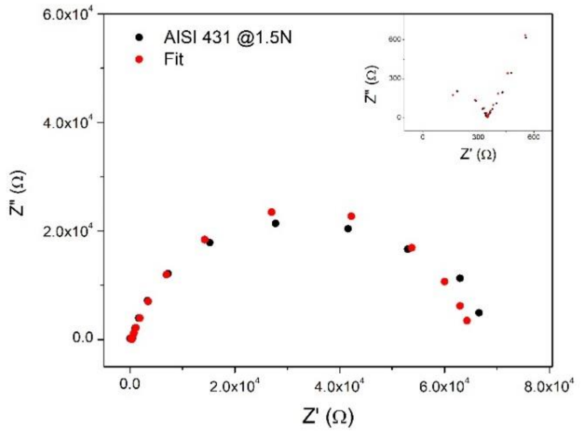

Figure 3.34 Nyquist diagram for of AISI 431 steel in contact with the citric acid 10^{-4} M solution while in continuous sliding at 1.5 N

$$\frac{1}{R_{ps}} = \frac{1}{R_{act}} + \frac{1}{R_{pass}} \qquad eq. (3.3)$$

Where:

$$R_{act} = \frac{r_{act}}{A_{act}} \qquad eq. (3.4)$$

and:

$$R_{pass} = \frac{r_{pass}}{A_0 - A_{tr}} \qquad eq.(3.5)$$

For AISI 431 steel the r_{pass} corresponded to the r_p value calculated in section 3.4.2.2, 160.6 ±5.0 kΩcm^2. Knowing R_{ps} and r_{pass} we could calculate r_{act} applying *eq. 3.6.* such resistance value represents the corrosion resistance value of the surface being exposed to mechanical wear.

$$r_{act} = \frac{A_{tr} R_{ps} r_{pass}}{r_{pass} - R_{ps}(A_0 - A_{tr})} \qquad eq.(3.6)$$

The estimated r_{act} value was 3.5 kΩcm^2, applying *eq.3.2*, the corrosion current was found to be 7.6 x10^{-6} A/cm^2. Such corrosion resistance and corrosion current values represent a system under corrosion. Hence, the surface of the material, being exposed to mechanical wear corrodes.

Additionally, Figure 3.35 shows the mapping profilometry of the wear track and a single profile. The wear loss was 4.1x10^{-3} ±4.0x10^{-7} mm^3 with a K value of 3.7 x10^{-5} mm^3/Nm. In comparison with the dry test, instead of material accumulation over the wear track we found material loss. Such difference made evident that the presence of the electrolyte modified the tribological response.

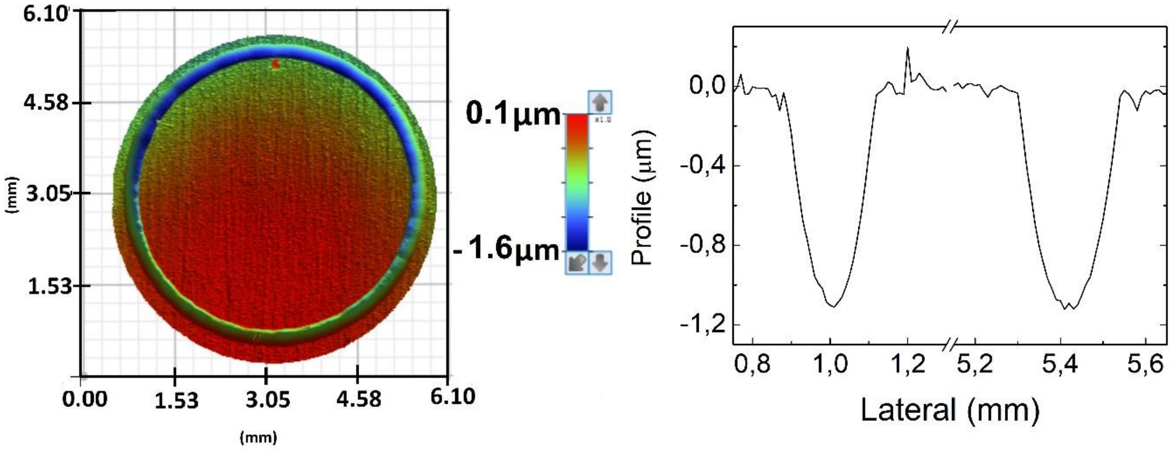

Figure 3.35 Right 3D mapping profilometry of an AISI 431 steel disc after continuous pin on disc test at 1.5N and in contact with the electrolyte. Left profile of the wear track region.

3.4.3.2 Latency tests

During the tribocorrosion latency tests, the surface material undergoes successive events of de-passivation (the passive layer is removed) and re-passivation (re–growth of the passive layer). The latency time was selected so that the re-growth of the passivation film, was not negligible[Celis and Ponthiaux 2012].

The resulting wear track was measured by contact profilometry as for the previous experiments. Figure 3.36 shows the resulting mapping and a single profile. Such results were used to calculate the total volume loss over the wear track. The estimated loss volume was $2.8 \times 10^{-3} \pm 4.0 \times 10^{-7}$ mm^3 with a K of 2.6×10^{-5} mm^3/Nm.

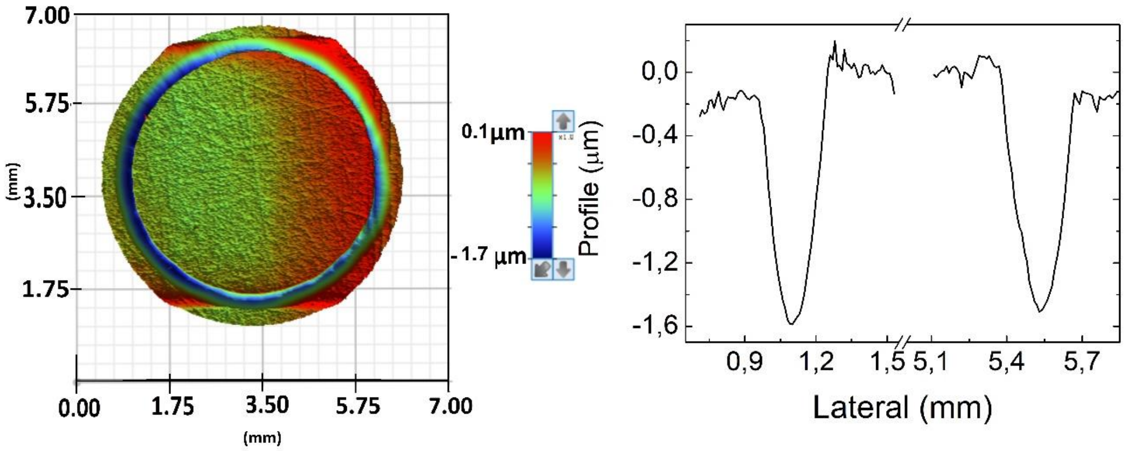

Figure 3.36 Right 3D mapping profilometry of an AISI 431 steel disc after latency pin on disc test at 1.5N and in contact with the electrolyte. Left profile of the wear track region.

The volume loss value measured after the latency tests along with the previous corrosion evaluation results for AISI 431 steel were used to calculate K_c and K_m as described in 1.2.2. The estimated value of K_c was 3.6×10^{-1}, and such a value describes a system where the contribution, to tribocorrosion, due to the acceleration of corrosion induced by the destruction of the passive film is low compared to the total wear. Furthermore, K_m was estimated to be 3.0×10^{-3}, and a $K_m < 1$ is typical for a system where the formation of the passive film accelerates the mechanical removal of the material[Celis and Ponthiaux 2012]. This means that when the passive film has time to regrow the mechanical wear removes a larger amount of material than when the passive film was not present.

3.5 Chapter's conclusions

In this chapter, the tribological and electrochemical behavior was studied of the substrate material was studies. For the tribological part, pin on disc tests were performed. The obtained experimental results confirmed the good wear resistance of both AISI D2 steel and AISI 431 steel.

For AISI D2 steel, the analysis of the obtained wear tracks showed accumulated material over the wear track area. Moreover, the presence of material adhered was responsible for the drastic change on the coefficient of friction and its presence was confirmed by the EDS analysis, where important amounts of iron over the counter body surface were found.

The electrochemical study was performed using an aqueous solution of citric acid pH 4. Under such pH conditions, the open circuit potential had a steady state at about -0.5 V vs Ag/AgCl. At this pH-E condition, most of the elements in the alloy could be expected to corrode. Moreover, the linear polarization and EIS experiments revealed that the AISI D2 steel corroded with an estimated value of specific corrosion resistance of 3.3 ±0.01 kΩcm^2. Hence to prevent the corrosion of the alloy without affecting its wear resistance the use of a protective thin film was proposed.

Similar to the AISI D2 steel, the AISI 431 steel presented accumulated material over the wear track area. The electrochemical tests showed that AISI 431 steel passivated with a specific corrosion resistance of 160.6 ±5.0 kΩcm^2.

Finally, the tribocorrosion evaluation showed that the combined damage over the surface modified the overall response of the system. Moreover, the determination of the ratios K_c and K_m showed that the acceleration of the corrosion induced by the destruction of the passive film was negligible compared to the total wear and that the formation of the passive film accelerated the mechanical material removal.

Chapter 4

Synthesis and characterization of the tungsten nitride thin film

This section presents the theoretical and experimental parts concerning the synthesis of the tungsten nitride thin films. The deposition of tungsten nitride and the role of the deposition parameters on the properties of the thin film are described.

4.1 Physical vapor deposition

Physical vapor deposition (PVD) is a well-known technology, widely used for the deposition of thin films. Such films are generally applied to increase tools lifetime, decrease friction, and to improve thermal properties[Kelly and Arnell 2000; Baptista et al. 2018]. PVD is a film deposition process in which a film grows on the substrate atom by atom, hence, it requires the atomization or vaporization of a material from a solid source (target). The atomic deposition can be carried out in vacuum, gas, plasma or electrolytic environment. When performed in vacuum environment, the reduction in residual gas reduces the contamination during the deposition process. Moreover, the PVD process can be plasma assisted; such plasma assisted PVD is divided into different power sources technologies. The different power sources used in PVD are direct current, radio frequency, pulsed plasma, ion beam, etc.

The most common surface coating methods in a gaseous state regarding the PVD process are thermal evaporation, arc evaporation and sputtering[Depla, Mahieu, and Greene 1991; Baptista et al. 2018]. These techniques allow for particles to be extracted from the target at very low pressure and be transported and deposited on to the substrate[Mubarak, Hamzah, and Toff 2005].

4.1.1 Magnetron Sputtering

Coating technologies are classified as physical or chemical deposition methods. The deposition methods can be divided into vacuum evaporation, glow-discharge processes, gas-phase chemical processes, and liquid phase chemical techniques[Aliofkhazraei 2011; Seshan 2002]. Amongst the glow discharge methods, different types of sputtering can be found. The most common approach to growing films by sputtering is the use of a magnetron source. A magnetic field is applied to a sputtering target so that it traps primary and secondary electrons in a localized region close to the cathode into the "racetrack"[Swann 1988; Edgar Alfonso and Cubillos 2012; Depla, Mahieu, and Greene 1991]. The electron trajectory is elongated so that the probability of ionizing a gas atom increases.

The sputtering technique was developed at the end of the 19th century and has been adapted to large scale production in the last decades[Wasa 2012]. The main advantages of this technique are: (1) deposition of virtually any material, (2) high deposition rates,(3) high purity films, (4) good film adhesion, (5) uniform films over large areas, (6) and relatively low cost [Depla, Mahieu, and Greene 1991; Swann 1988; J. G. Han, n.d.]. To obtain thin films by magnetron sputtering first, high-energy ions strike a solid surface (target) and through the momentum interchange cause the emission of atoms from the surface. Second, the ejected atoms are transported towards the object to be coated[Swann 1988]. To allow the atoms to move freely low gas pressures are required.

To power a magnetron it is possible to choose from radio frequency (rf), direct current (dc), pulsed dc and high-power impulse magnetron sputtering (HIPIMS)[Depla, Mahieu, and Greene 1991]. Among them, the most extensively used is dc magnetron sputtering. In dc sputtering, the target works as the cathode electrode, and the substrate is placed on the anode, which is electrically floating or biased to some negative potential. During the dc discharge, a plasma is generated near the cathode (-ve) surface, typically the gas pressure must be > 0.1 Pa. The magnetron traps the electrons close to the target surface creating a high density plasma from which ions (+ve) can be extracted to sputter the target material[Edgar Alfonso and Cubillos 2012]. This type of sputtering requires that the target be a conductive material. A diagram of a dc magnetron sputtering is presented in Figure 4.1.

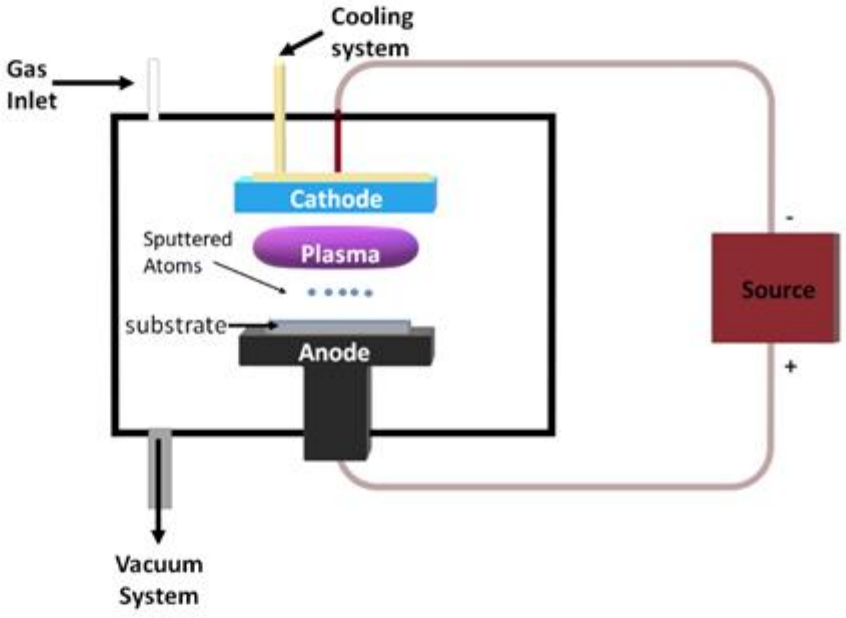

Figure 4.1 Schematic diagram of a dc magnetron sputtering system. Image adapted from reference [Edgar Alfonso and Cubillos 2012]

4.1.1.1 *Reactive magnetron sputtering*

The use of electrical conductors as targets limits the choice of materials that can be deposited. To mitigate this problem, a reactive gas can be added to the discharge. The reactive gas, e.g. nitrogen, oxygen, hydrogen sulfide, etc. can react with the sputtered material to form a compound on the substrate[Depla, Mahieu, and Greene 1991; Swann 1988]. Reactive sputtering is commonly used for the deposition of oxide and nitride thin films using metallic substrates because of the high deposition rate, controlled deposition, and the possibility to use either dc or rf power[Seshan 2002]

A possible drawback of reactive sputtering is that the reactive gas can react with the target surface. This is known as target "poisoning", which results in a significantly reduced sputter yield and, thereby, reduced deposition rate. A further consequence of poisoning is a hysteresis of the reactive gas partial pressure at increasing/decreasing reactive gas flow, and, associated with an unstable operation regime between high and low target uptake of the reactive gas at a constant partial flow of that reactive gas, which often requires additional means of stabilization in practical applications[Safi 2000; Güttler et al. 2004]. The significance of this phenomenon is that quite extensive investigation is required to establish the optimum experimental conditions to deposit a given compound in a particular deposition system.

4.1.2 Radiofrequency magnetron sputtering

Radiofrequency sputtering was developed to enable the sputtering of dielectric materials, but it can also be used to sputter metals as well. The rf sputtering operates analogously to dc sputtering only that for a small part of the rf cycle, the cathode and anode are electrically reversed in each electrical cycle. This eliminates charge buildup on an insulating surface by providing an equal number of ions, then electrons[Seshan 2002]. This allows insulators or metals to be sputtered in reactive environments. The use of an insulating target together with the difference in mobility of the electrons and ions (because of the difference in mass), and the existence of a capacitor in the rf circuit, means that a large negative space charge accumulates in the surface of the target. It is this negative charge that attracts the plasma ions and produces the sputtering. Nevertheless, rf sputtering has a notable lower deposition rate, this is because the intensity of the negative space oscillates and the magnetron trap alternately opens and closes, allowing the electrons to escape when the trap is open and forcing electrons to cross the magnetic field line. This leads to a drop in the discharge power and consequently to a decrease of the available power at the target [Depla, Mahieu, and Greene 1991].

4.2 Experimental part

In this section, all the materials, methods, and experimental conditions for the growth and evaluation of the thin films are described.

4.2.1 Substrate's preparation

Before coating the substrate, each substrate was polished to mirror finishing utilizing either a Buehler-MetaServ 250 at IUT Amiens or a Strueurs Tegra Pol-21 polishing machine at the 'Laboratoire de Reactivite et Chimie des solides'. The polishing condition were 15 N of load and 300 rpm with different abrasive papers of SiC (from 600 up to 1200) to finish them with a cloth and a solution of Al_2O_3 of 0,1 µm of size. The abrasive papers, cloth and Al_2O_3 solution were provided by PRESI in France.

After the polishing process, each sample was cleaned consecutively with acetone (Fisher chemicals, general purpose grade) and isopropanol (Sigma-Aldrich ≥99,7%) for 10 min using an Elma ultrasonic bath. To finish each sample was dried using filtered compressed air.

4.2.2 Coating conditions by RF magnetron sputtering

To select the deposition conditions several publications were consulted and used as a guide. Such references reported good mechanical and tribological properties but none of them reported the corrosion behavior or the tribocorrosion behavior of the resulting thin films [P. Hones et al. 2000; Polcar, Parreira, and Cavaleiro 2007a; 2008; Brett and Nimigean 1997; Baker and Shah 2002; Samano et al. 2010; Shen and Mai 2000; Addonizio et al. 2012; Polcar, Parreira, and Cavaleiro 2007b; Parreira, Carvalho, and Cavaleiro 2006; Louro and Cavaleiro 1999]. A summary of the deposition conditions in such publications is presented in Table 4.1, most of the references used dc reactive sputtering in a wide range of deposition powers and pressures. Moreover, most of them have shown that at a 12 % of nitrogen in the gas mixture crystalline W_2N could be obtained.

Table 4.1 Summary of the deposition conditions for tungsten nitride films

Author	Sputtering	Power density (W/cm^2)	Temperature	Pressure (Pa)	Pressure (mTorr)	N_2 %	Distance substrate-target (cm)
Hones, P. et al	rf	5.05	500 ± 20 K	0.66	5	0.1-0.3	10
Samano, E.C. et al	dc and laser ablation	5.09	400 °C	0.53-2.13	4 - 17	0 - 50	3
Polcar, T: et al	dc	6 mA cm^{-2}	<350 °C	0.3	2	0- 75	6.5
Polcar, T: et al	dc	10 mA cm^{-2}	<350 °C	0.3	2	0- 75	6.5
Louro, Cavaleiro	dc	10	450 °C	0.3	2	0.1 – 0.6	--
Addonizio , et al	Pulsed dc	0.65-1.97	'Room temperature'	0.73	5	7.7- 20	8
Shen, Mai	d c	4.28	200 °C	0.8	6		7

In the present work, tungsten nitride thin films were obtained by magnetron sputtering using a MP300S Plasyss system. The vacuum chamber was evacuated at a pressure of 1.25×10^{-4} Pa (1×10^{-6} Torr) before deposition. The target was a metallic tungsten disc (99.99%) provided by Plasmaterials, Inc. The target-sample distance was fixed at 4.5 cm. The target was cleaned by starting the plasma with argon, at least 5 minutes before each deposition. During this time, the substrate was covered with a shield. Figure 4.2 shows a diagram of the used system.

For each experiment a 300nm metallic tungsten buffer layer was first deposited.

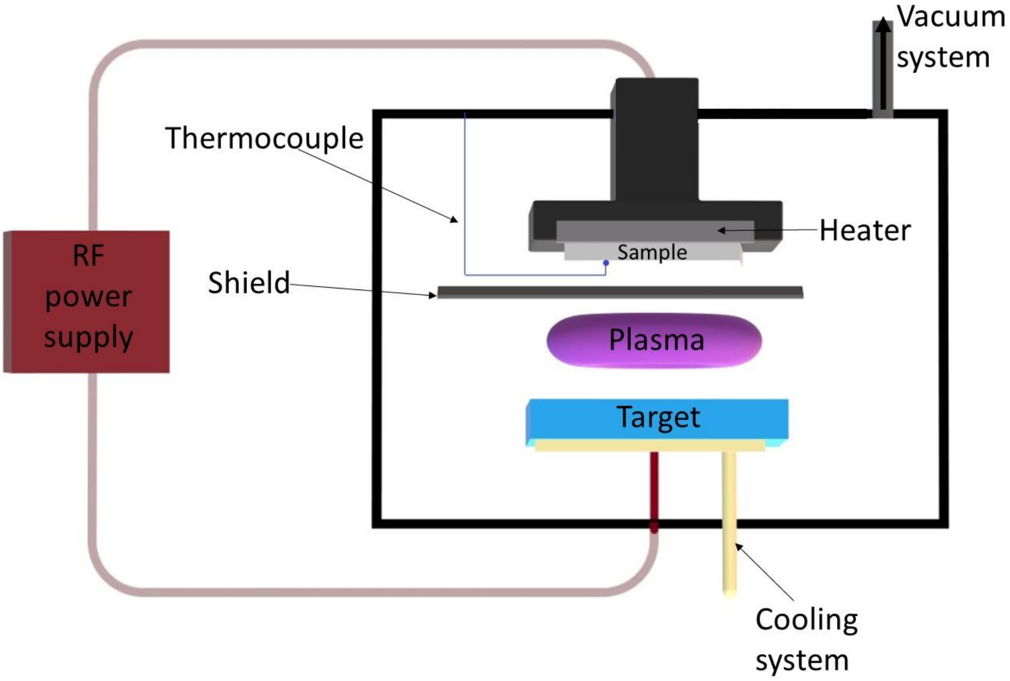

Figure 4.2 Diagram of the experimental sputtering configuration.

For the tungsten nitride deposits, a mixture of argon (88 %) and nitrogen (12 %) was used. The pressure was fixed at 1.0, 0.7 or 0.5 Pa (7.5, 5.2 or 3.2 mTorr). The deposition power was 35 W, 150 W or 200 W. The substrates were heated at 220°C, before starting the deposition and the heating system was kept on during the deposition process. Each substrate was coated with at least 1μm of thickness. Following to sputtering, the samples were left to cold down inside the vacuum chamber overnight. Subsequently, the samples were transferred to a tubular furnace provided by 'Services for research'. Once in the furnace, the samples were heat-treated for 90 min at 500 °C under a nitrogen atmosphere. The nitrogen flow was started at least five minutes before the furnace was turned on. The heating rate was fixed at 10°C/min for all the samples. The samples were left to cold down in the furnace to a temperature lower than 80 °C before the nitrogen flow were stopped. After the heat treatment the samples were stored in a closed acrylic box in presence of a desiccant.

4.3 Results

This section presents the experimental details of the coating process, the thin film properties, and the properties optimization in terms of tribocorrosion protection.

4.3.1 Thin films by dc vs rf sputtering magnetron.

As a film, tungsten nitride is an electric conductor; hence it can be obtained by either dc or rf magnetron sputtering. If similar deposition conditions are used the chemical composition of the thin film could be similar. Nevertheless, properties such as crystallinity, adherence, porosity, etc. might not be the same. AISI D2 steel samples were coated by either dc or rf magnetron sputtering at 35 W and 1 Pa with the mixture of Ar and N_2. SEM images of the surface of thin films obtained by dc and rf magnetron sputtering are shown in Figure 4.3a and 4.3c respectively. For the thin film deposited by dc sputtering the image shows a cauliflower like texture. Moreover, the image obtained of the coating deposited by rf magnetron sputtering presented some material

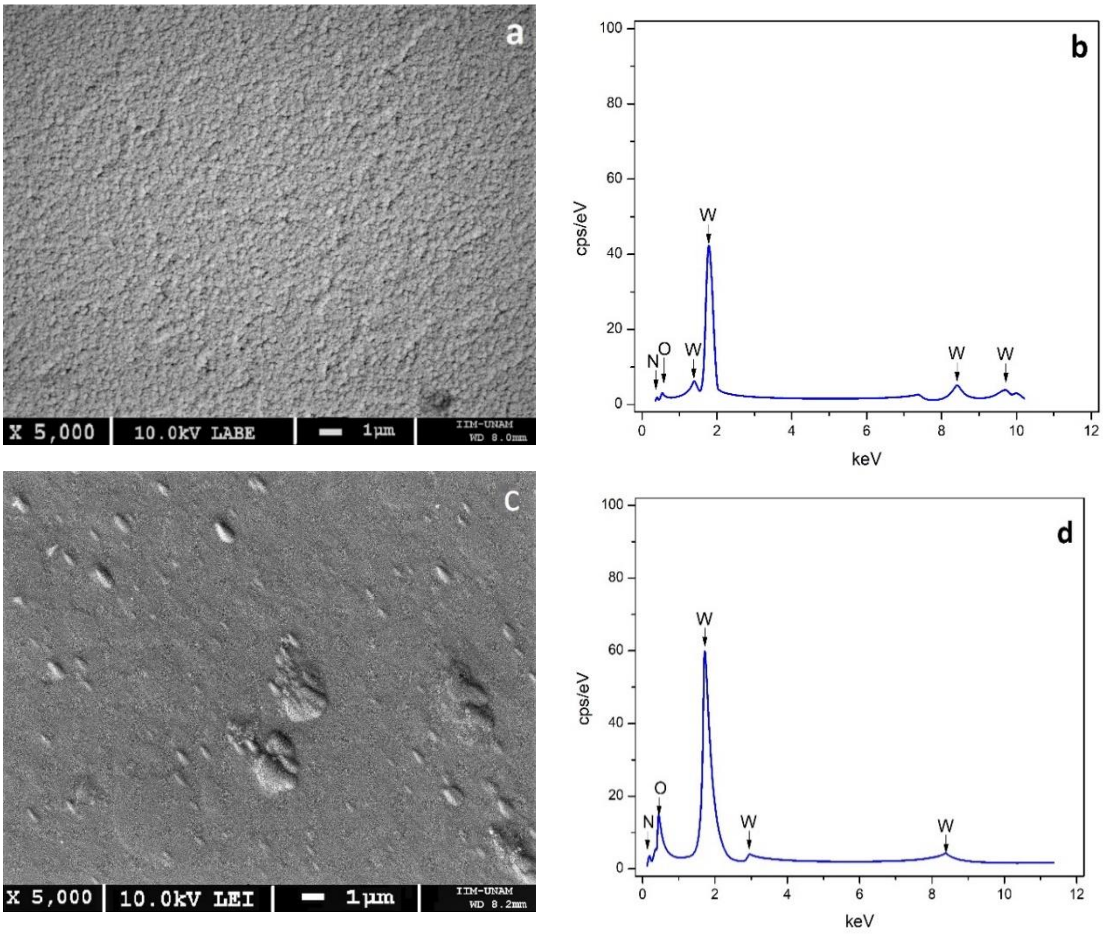

Figure 4.3 SEM image and EDS spectrum for the thin film sputtered by dc magnetron sputtering (a,b) and rf magnetron sputtering (c,d) at 5000 x.

accumulations. Additionally, Figure 4.3b and 4.3d present the EDS spectrum for each of the samples where the same elements were detected.

For a film to protect against corrosion, they must be the smoothest possible to avoid problems of diffusion of the electrolyte in between defects or pores in the thin films. Considering the observed surfaces, the thin film deposited by dc magnetron sputtering might present corrosion due to the observed texture. The electrolyte could travel in between the granules and hence directly attack the substrate and/or trigger the detachment of the thin film. Preliminary corrosion tests showed similar corrosion resistance for the coatings deposited by dc and rf sputtering. Since no significant difference between the coatings deposited by rf or dc sputtering was found and most of the experimental work was carried out in France, it was decided to continue the study with thin films deposited by rf magnetron sputtering (the deposition system available in France).

4.3.2 Growth rate and thickness

To estimate the deposition time, thickness measurements by profilometry were performed using different coated glass samples. Samples at each gas pressure and power were obtained. Figure 4.4 shows the temporal evolution of the tungsten nitride thickness for 1 Pa at different deposition power. Such a figure illustrates how at larger power the growth rate increases due to an increment on the ion bombardment. The estimated growth rates were 8 nm/min at 35 W, 15 nm/min at 150 W and 18nm/min. Figure 4.5 presents the growth rate of the film at 150 W and different deposition pressures; the curves show that the deposition rate is approximately linearly proportional to the deposition power. The estimated deposition rates were 8 nm/min

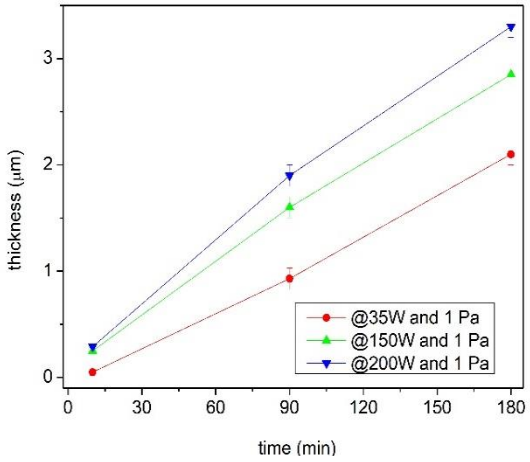

Figure 4.4 Tungsten nitride growth rate at 1 Pa of pressure and different deposition powers

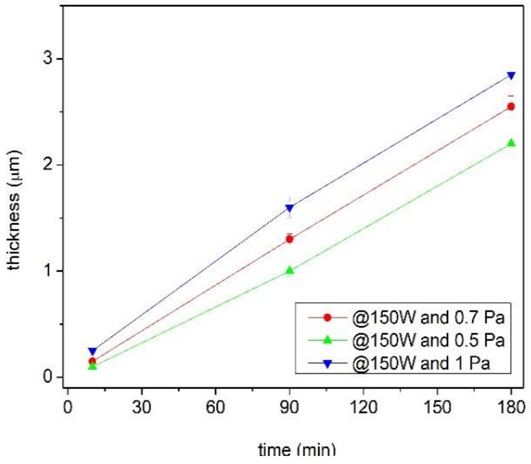

Figure 4.5 Tungsten nitride growth rate at 150 W and different pressures.

at 0.5 Pa, 11 nm/min at 0.7 Pa and 16 nm/min at 1 Pa. On the other hand, high powers and low pressures have been linked to increments on the thin film density[Sun, Liu, and Cao 2010; Long et al. 2021; Musil et al. 2013].

The mean free path defined by *eq 4.1* represents the average distance traveled by the sputtered particle of diameter, δ_m. Such distance is enhanced at low pressure (P) and high temperature (T). Such enhancement has been linked to larger relative densities on the resulting thin film.

$$\lambda = \frac{2.3\ x\ 10^{20}\ T}{P\ \delta_m^2} \qquad eq. 4.1$$

For applications such as corrosion protection, a dense film is recommended to avoid the migration of the electrolyte up to the substrate. Hence for the present work, a dense thin film is looked for.

4.3.3 Surface roughness

After deposition, contact profilometry was performed to measure the surface roughness of the thin films. The average roughness (R_a) and the maximum peak to valley (R_z) were evaluated for the different deposition conditions. Table 4.2 presents a summary of the results. They show that an increment in the deposition power led to an increase in the surface roughness. However, no significant change was found when the pressure was changed.

Table 4.2 Summary of the thin film's surface roughness at different deposition conditions.

Sputtering conditions		**Ra (nm)**	**Rz (nm)**
Power (W)	**Pressure (Pa)**		
35	1	120 ± 20	850 ± 180
150		270 ± 50	700 ±150
200		280 ± 20	800 ± 200
	0.7	260 ± 10	1000± 300
	0.5	250 ± 20	800 ± 150

4.3.4 Thin film stress

A common characteristic we can find in films obtained by sputtering is residual stress [Thornton and Hoffman 1989a; Shen et al. 2000; Clyne 2001]. The stress can come from intrinsic, thermal, and mechanical origins. The presence of stress can impact the performance reliability and durability of material components and devices. Nevertheless, stress can have a positive effect on conductivity, dielectric permittivity, and charge carrier mobility. On the other hand, stress can lead to low adherence, fracture, or blistering of the thin films. In the case of films intended to enhance mechanical properties, it is important to determine the stress and reduce it to avoid problems such as peeling off and cracking.

Intrinsic stress is present as a result of the combined chemical and microstructural defects incorporated during the condensation process [Abadias et al. 2018b]. Thermal stress is caused by the difference in thermal expansion coefficients of the film and the substrate since the use of an insulating target together with the difference in mobility of the electrons and ions (because of the difference in mass), and the existence of a capacitor in the rf circuit, means that a large negative space charge accumulates in the surface of the target. it is this negative charge that attracts the plasma ions and produces the sputtering.[Thornton and Hoffman 1989b]

To decrease intrinsic stress and hence the blistering and fracture risk, the thin films obtained in the present work were heat treated at different temperatures and in order to estimate the stress, the wafer curvature technique was utilized.

This technique is one of the most common ways to determine stress. The principle behind it is to measure the curvature of the substrate before and after deposition of the film.

To determine the stress, of 2 cm x 1 cm x 100 μm thick pieces of silicon wafers [100] were coated. Standard profilometries measurements were performed over the center line of the pieces of silicon before and after the coating process. The Stoney equation was applied to calculate the thin films stress at the different deposition conditions.

In a first approach, to estimate the heat treatment temperature, thin films obtained at 35 W and 1 Pa of pressure were synthetized. The heat treatment of independent samples was performed under continuous nitrogen flow at either 300 °C, 400 °C or 500 °C, the heat rate was 10 °C per minute. The sample was kept at the aimed temperature for 90 min. Table 4.3 presents the results of the stress found for the different heat treatment temperatures. It can be observed that there was a decrease in the stress with the increasing temperature of the heat treatment. For the tested thin films, it was impossible to heat treat the sample over 500 °C because at larger temperatures the thin film tended to delaminate probably due to thermally induced stress or oxidation [Polcar, Parreira, and Cavaleiro 2008].

Table 4.3 Summary of surface stress results of thin films at different heat treatment temperatures.

Heat treatment temperature (°C)	Stress (MPa)
Without heat treatment	11.3 ±9.9
300	5.4 ±3.4
400	2.8 ±1.2
500	2.5 ±1.2

Stress can also be caused by chemical and structural defects present in a thin film depending on the deposition conditions. Hence, the stress was determined for the different deposition conditions (power and pressure) and heat treated at 500°C. Table 4.3 presents a summary of the found values. Such values showed that the coating stress was not significantly different for the different deposition conditions.

Table 4.4 Surface stress values for thin films sputtered at different conditions.

Power (W)	Pressure (Pa)	Stress (MPa)
35	1	2.5 ± 1.2
150	1	2.6 ± 0.6
200	1	2.6 ± 0.3
	0.7	3.4 ± 0.5
	0.5	3.8 ± 0.3

4.3.5 X ray diffraction

The measurements were made either at the UNAM with a x ray diffractometer Rigaku Ultima IV (1,5406Å) or at LPMC using x ray diffractometer D8 by Bruker (1,5406Å) in either θ-2θ or grazing incidence arrangement with a rotatory detector from 10° to 100°.

Figure 4.6 shows the diffraction pattern for thin films deposited on silicon wafers at the same deposition pressure and temperature, and different powers. Such patterns were obtained using the grazing incidence configuration. The obtained signals corresponded mainly to two different types of crystal WO_3 and W_2N. Moreover, it is evident that at larger power deposition the crystallinity of the tungsten nitride phase increased.

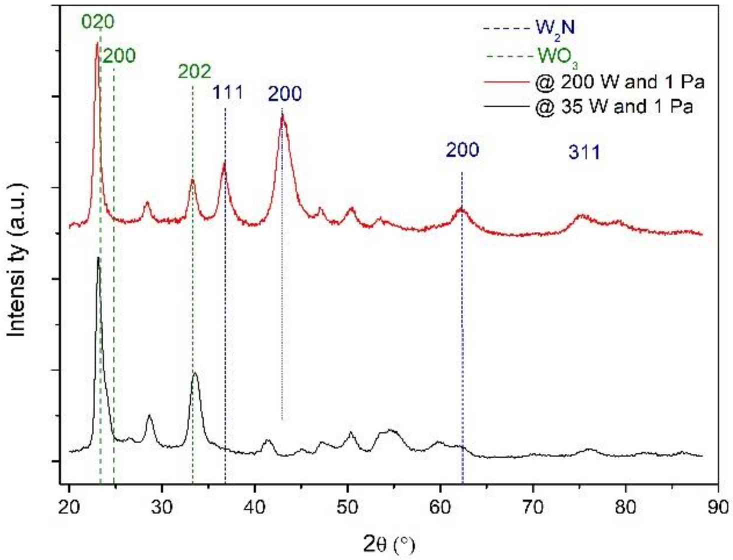

Figure 4.6 XRD patterns for thin films obtained at 1 Pa of pressure and different powers.

Figure 4.7 presents the diffraction patterns for thin films synthesized at the same deposition power but at different pressures. The spectra show that an increment in the deposition pressure probably reduces the crystallinity of the thin film.

Figure 4.8 shows the θ-2θ diffraction patterns for the thin film obtained at 150 W and 0.5 Pa, the red line is the pattern for the thin films as deposited. While the black line presents the pattern of the thin film after the heat treatment process. Such comparison shows that the heat treatment promotes the crystallinity of the thin film. The estimated crystalline size was of about 25 nm for the coatings deposited at 1 Pa and different powers, 162 nm and 198 nm for 200 W and 0.5 and 0.7 Pa respectively.

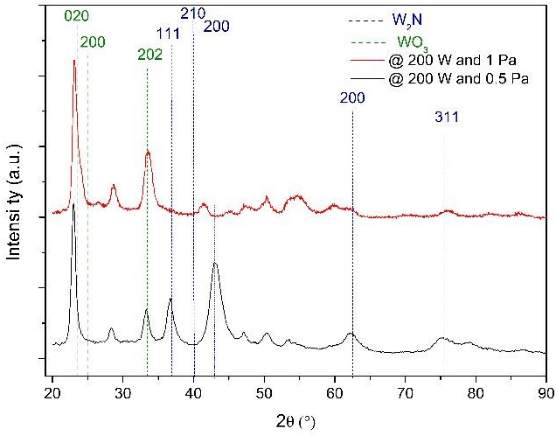

Figure 4.7 XRD patterns for thin films obtained at different pressures and 200 W of power.

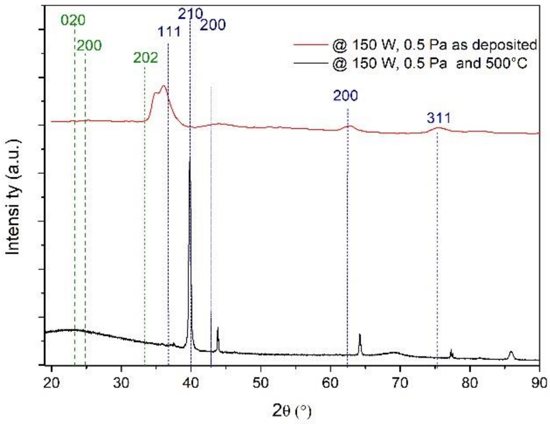

Figure 4.8 XRD patterns for thin films at 150W and 0.5 Pa before and after heat treatment at 500°C. θ-2θ configuration

4.3.6 Scratch test (adherence of the thin film)

Scratch tests were performed either at IIM-UNAM or LPMC-UPJV using a Scratch tester Millennium provided from TRIBO technic. The tests were performed at increasing charge from 0 to 50 N using a 0.2 mm diameter ball of Al_2O_3 grade 20 from Redhill Precision balls. The critical loads were identified following the ASTM C1624-05 [ASTM 2015].

To evaluate the adherence several scratch tests were performed on thin films deposited under different conditions on AISI D2 substrates. Figure 4.9 shows images of the scratch tack on thin films made at 1 Pa gas pressure and different plasma powers. Each sample shows different critical loads. For the sample deposited at 35 W the L_{C1} 9.4 ±0.5 N and L_{C2} 15.6 ±0.7 N. The thin films obtained at 150 W and 200 W presented L_{C1} 9.4 ±0.5 N and 8.4 ±0.4 N respectively. Moreover, L_{C2} was detected at 12.5 ±0.6 N and 10.9 ±0.5 N, at these charges chipping failure could be identified. Such results show that at larger deposition power the critical load decreases slightly.

Figure 4.9 Resulting scratch track by increasing load scratch tests for tungsten nitride thin films deposited at different powers and 1 Pa of gas pressure.

Figure 4.10 displays images of the obtained scratch tracks for samples at different pressure depositions. The thin film deposited at 0.7 Pa a L_{C1} was 8.3 ±0.4 N and L_{C2} is present at 10.5 ±0.4N. Finally, for the sample coated at 0.5 Pa L_{C1} was 7.9 ±0.3N and L_{C2} 10.8 ± 0.5 N. No significant difference was found in the film adhesion of coatings deposited at different gas pressures.

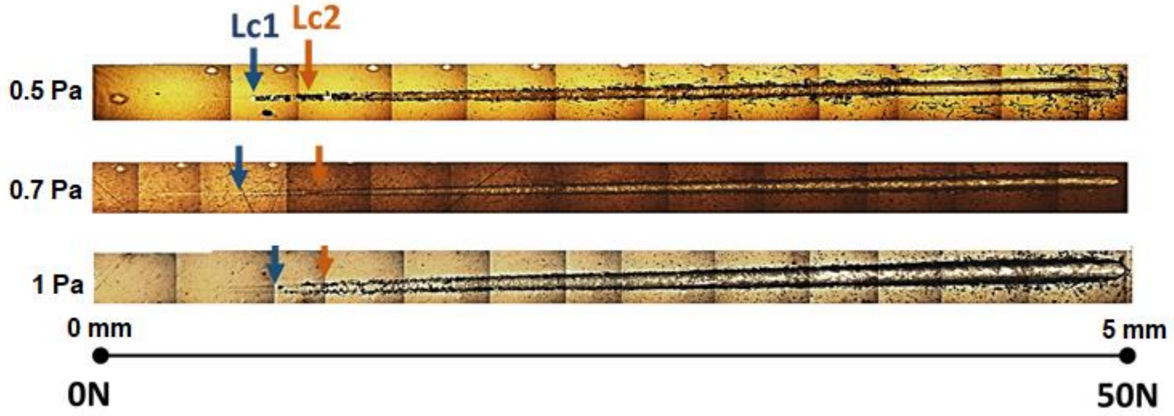

Figure 4.10 Resulting scratch track by increasing load scratch tests for tungsten nitride thin films deposited at different gas pressure and 200W.

4.3.7 X-ray photoelectron spectroscopy

XPS analysis was performed on the steel coated samples. The tests were performed at IIM-UNAM using a PHI 5000, Versa Probe II, type scanning XPS microprobe. The samples were measured with an incident monochromatic radiation Al Kα X-rays (1486.6 eV) at 45 ° and 170 W.

Figure 4.11 presents the XPS survey spectrums for thin films made at 1.0 Pa of gas pressure and various plasma powers. The survey spectrum shows the spectral signatures of tungsten, nitrogen, and oxygen. Similar results were found for thin films deposited at 150 W power and different gas pressures; the survey spectra are shown in Figure 4.12. Such type of survey spectra has been previously reported for WN_x and

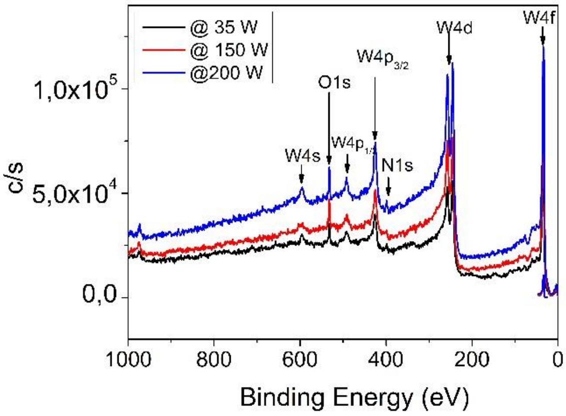

Figure 4.11 XPS survey spectrum for thin films deposited at 1 Pa of gas pressure and different plasma powers.

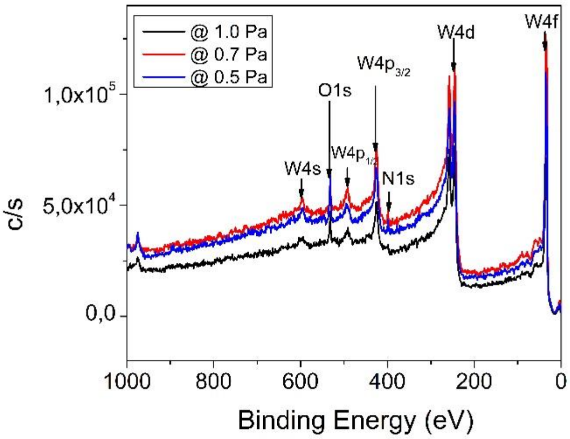

Figure 4.12 XPS survey spectrum XPS survey spectrum for thin films deposited at 150 W of plasma power and different gas pressures.

WO_3 thin films [Baker and Shah 2002; Shen and Mai 2000; Wen et al. 2010; Tesfamichael et al. 2010; Addonizio et al. 2012].

Figure 4.13a shows the high-resolution data for tungsten (W 4f), the spectrum shows the typical doublet for tungsten along with a small signal commonly assigned to WO_3. The core level spectrum for nitrogen (N 1s) and oxygen (O 1s) are displayed in Figure 4.13b and 4.13c, respectively. Similar have been reported for tungsten nitride thin films by other authors [Wen et al. 2010; Addonizio et al. 2012; Shen and Mai 2000].

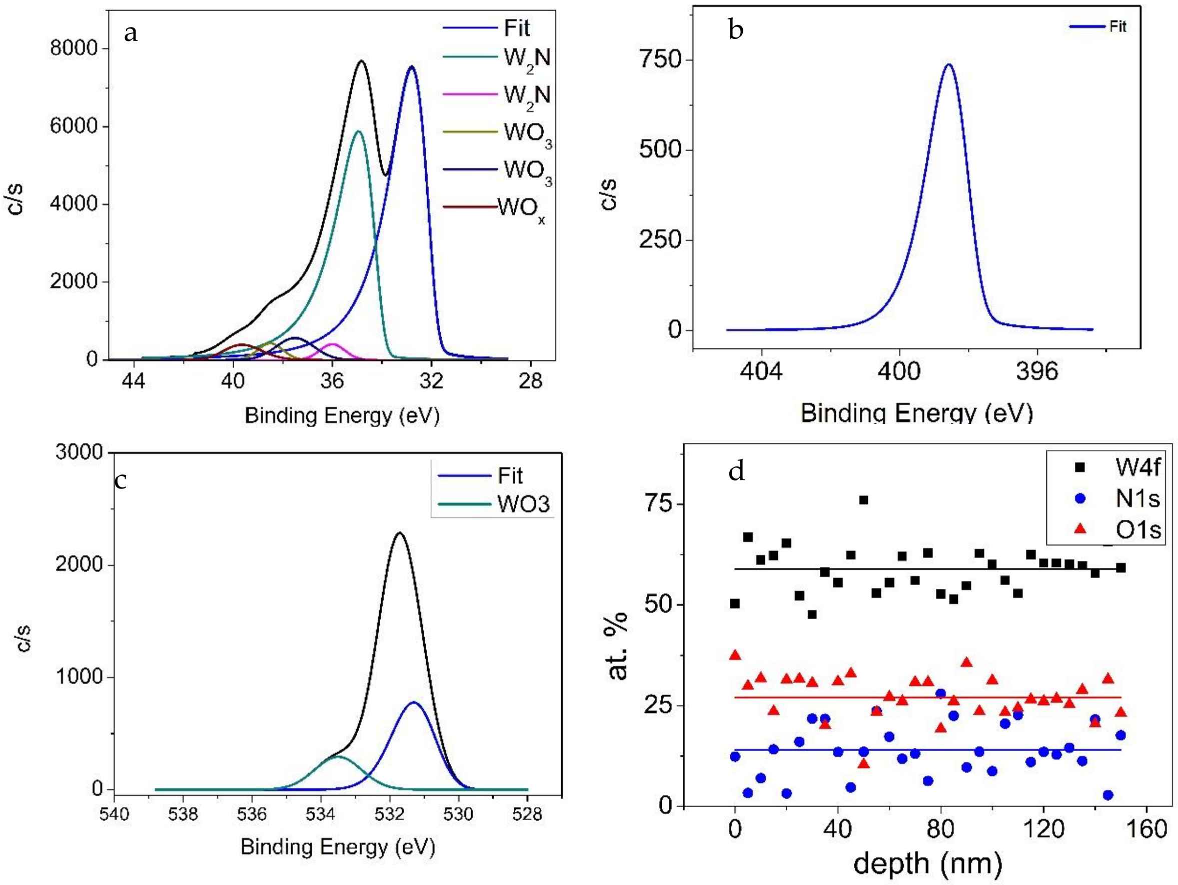

Figure 4.13 High resolution spectrum for a) W 4f, b) N1s, and c) O1s. d) Atomic percentage detected at different depths.

Since the Ar/N_2 ratio was kept constant, no large changes in the final composition of the thin films were expected. This was confirmed from the XPS analysis where the average atomic composition was found to be 51.1 ± 3.5 % of W, 35.4 ± 3.4% of O and 13.3 ± 2.1% of N. Such composition obtained from the sample surface after erosion. Moreover, composition analysis measurements were performed at different depths. Figure 4.13d shows the atomic percentage profile of each element from the surface down to 160 nm within the thin film, the lines represent the average value of each element and the points the value measured at the given depth. The percentage of the elements is constant in the measured profile indicating that all the detected elements are part of the analyzed coating.

Moreover, analysis of the chemical shift showed that the tungsten detected was bonded to oxygen and nitrogen, and both nitrogen and oxygen are only bonded to tungsten. Hence the obtained coatings are tungsten oxynitride.

4.3.8 Hardness measurement by micro indentation.

Micro indentations measurements were made to the samples using a Nanovea PB1000 Hardness Tester with a Vickers diamond point in a load range between 0.1 to 2 N. To estimate the thin film hardness, the mixed hardness for the substrate-thin film was considered. Different loads were applied the model proposed by Lesage et al [Lesage et al. 2006] was used to estimate hardness of the thin films.

During the indentation process delamination frequently occurred, hence only estimated hardness values could be obtained to give a general tendence of the hardness values as a function of the preparation conditions and not the actual hardness values.

For thin films deposited at 35 W and 1.0 Pa the estimated value by the Lesage model was 8.9 ± 0.2 GPa, whereas for a thin film made at 200 W and 1.0 Pa the estimated value was 9.1 ± 1.7 GPa. Clearly these values are not significantly different. For the samples obtained at other deposition conditions the obtained results could not be adjusted due to the delamination problems. Figure 4.14 shows examples of the indentation marks. Figure 4.14 (a) shows an indentation mark for a measurement with no delamination, hence the hardness value obtained could be used in the thin film's hardness estimation. Figure 4.14 (b) shows an example of an indentation mark obtained at the same indentation conditions as for (a), nevertheless, this thin film presented evident delamination in the indentation region. When this type of behavior was encountered attempts to estimate the thin film hardness with the different existing models were unsuccessful. The delamination problems will be treated in more detail in the following chapter.

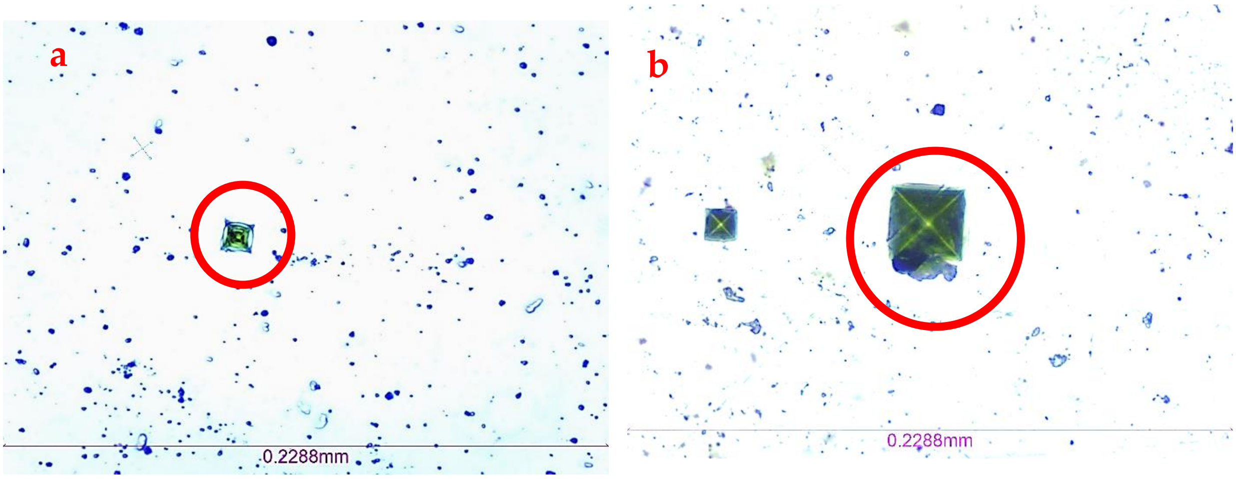

Figure 4.14 (a) Indentation trace for a 0.5 N applied load over AISI D2 coated with tungsten nitride at 200 W and 1.0 Pa. (b) Indentation trace for a 0.5 N applied load over AISI D2 coated with tungsten nitride at 200 W and 0.7 Pa.

4.4 Conclusions

The XRD measurements of the obtained thin films showed the existence of a combination of two crystalline structures, a fcc structure of tungsten nitride and a monoclinic phase of tungsten oxide (WO_3). The crystallinity was somehow promoted by using higher deposition powers and lower gas pressures.

The heat treatment of the coated samples caused a decrement in the stress and improved crystallinity of the films. Such diminution in the stress might be expected to improve the tribological response. Nevertheless, the heat treatment boosted the formation of the oxide, and the oxidation of the thin film has been linked to delamination problems.

The scratch tests showed that an increase in the deposition power, slightly diminished the resistance towards fracture of the thin films giving a L_{C2} of 10.9 N for the sample sputtered at 200 W and 1.0 Pa.

The XPS results showed that elements in the thin film not affected by the deposition conditions. As the XPS depth profile showed, the detected elements and their atomic percentages remain constant, and the thin films are tungsten oxynitride. The same elements were detected by EDS. Hence, the variations in the response of the thin film are not related to the composition but to other factors such as the crystalline structure, roughness, thin film's density, etc.

For this work a dense thin film with good adherence should present the best performance as a protective thin film to tribocorrosion. Therefore, the best deposition conditions for tribocorrosion protection of the proposed substrates are probably low deposition pressures and medium to high powers.

Chapter 5

Tribological and tribocorrosion properties of the thin film

This chapter presents the wear behavior at room temperature and relative humidity of the1µm of thick tungsten nitride thin films. The type of wear and the wear rate were determined. Additionally, the corrosion resistance was evaluated by electrochemical impedance. The influence of the sputtering parameters and the type of substrate were appraised. Finally, the tribocorrosion behavior of the passive thin films was determined.

5.1 Experimental conditions

5.1.1 Pin on disc tests

The tribology experiments were performed using a UTM-Tribolab by Bruker in a pin on disc configuration at the conditions described in 3.3.1

5.1.2 Electrochemical tests

Electrochemical measurements such as open circuit potential, and electrochemical impedance spectroscopy were performed with a PalmSens 4 potentiostat at the conditions described in 3.3.2.

5.1.3 Open circuit potential

Open circuit potential (OCP) measurements were carried out for up five hours to verify the steady-state and determine the characteristic reaction time (t_{react}). After the OCP measurements either a linear polarization or an EIS test was performed.

5.1.4 Electrochemical impedance spectroscopy

EIS measurements were carried out using the same arrangement as for the OCP studies in a frequency interval from 10^5 Hz to 10^{-2} Hz with at least 3 points per decade and an amplitude of ± 10 mV vs OCP. The results were modeled using the equivalent circuit approach to determinate the corrosion resistance of the system which when multiplied by the exposed area of the sample gave the specific corrosion resistance.

5.1.5 Tribocorrosion evaluation

The tribocorrosion behavior of the passivated coatings was evaluated. Given that tribocorrosion is a mixed phenomenon, such evaluation was carried out coupling the pin on disc tests and the electrochemical measurements. For such studies a three-electrode cell and an aluminum oxide ball were used.

5.1.6 Continuous sliding test

After a steady OCP value was achieved, EIS and pin on disc tests were performed simultaneously. A continuous sliding pin on disc tests at 1.5 N of normal load and 0.02 m/s of angular speed were performed, for a total length of 72 m. While the pin on disc test was running, EIS measurements were carried out in a frequency interval from 10^5 Hz to 10^{-2} Hz with at least 3 points per decade. From such tests the volume loss and the corrosion current density of the active material were determined. Contact profilometries and SEM measurements were used to assess the final state of the wear surface. Furthermore, the EIS results were fit using the equivalent circuit approach.

5.1.7 Latency tests

For the latency tests, successive identical cycles of active pin on disc and latency were performed until a total wear test length of 72m was reached. Each cycle comprised a full turn (1 s) and a time off (t_{off})of 20 s. The applied normal load was 1.5 N.

By Combining the EIS results, the continuous sliding volume loss and the total volume loss during on the latency tests, the ratios K_c and K_m were calculated. As described in Chapter 1, the K_c value can be used to define if the corrosion process of the mechanical wear dominates over the tribocorrosion process. Furthermore, K_m indicates the effect of the material passivation in the mechanical material removal, and the contribution due to the re-passivation as described in the first chapter.

5.2 Results

5.2.1 Pin on disc

During the pin on disc test the normal force and the friction force were sensed, and then used to calculate the coefficient of friction. The pin on disc test produced a circular wear track on the thin film.

5.2.1.1 *Coefficient of friction*

The temporal evolution of the COF from the pin on disc tests of the thin films sputtered at 1.0 Pa and different powers are shown in Figure 5.1. The red line is the smoothed data using the adjacent average filter of 500 points. In each case the curves showed the typical sharp variation at the beginning of the test. Corresponding to the running in period, once the steady state regime was achieved the COF was estimated, the results for the plasma powers of 35, 150 and 200 W were 0.37 ± 0.02, 0.27 ± 0.05 and 0.32 ± 0.03 respectively. Such results present no clear tendency with respect to the deposition power and are almost within the experimental uncertainty of the measurement. Considering the obtained XRD presented in 4.3.5 one can infer that the crystallinity of the thin film and the COF do not depend on the plasma power used for the deposition process.

Additionally, thin films sputtered at 200 W but different gas pressures were tested, and Figure 5.2 presents the comparison of the temporal evolution of samples sputterer at 200 W and 1.0, 0.7 or 0.5 Pa. The curves have a similar behavior than the one found for the thin films made using different deposition powers. The average COF was estimated in the steady state range of the test giving the following values: 0.32 ± 0.03, 0.33 ± 0.03 and 0.42 ±0.05 for 1.0, 0.7 and 0.5 Pa respectively. Such values of COF are slightly smaller than the ones found for AISI D2 steel (0.53 ± 0.10) and AISI 431 steel (0.48 ± 0.21). Such smaller COF is linked to a smaller friction force, so probably the thin film acts as a lubricant and smaller damage over the wear track was expected.

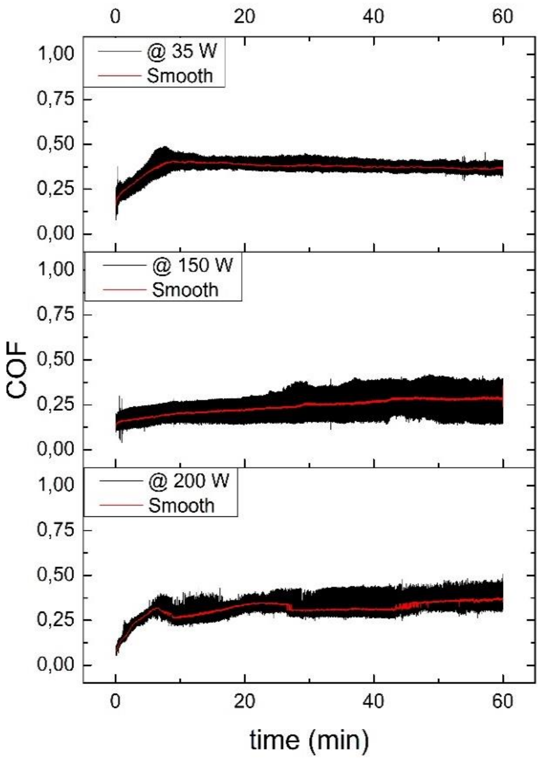

Figure 5.1 Temporal evolution of the coefficient of friction for thin films sputtered at 1.0 Pa and different powers.

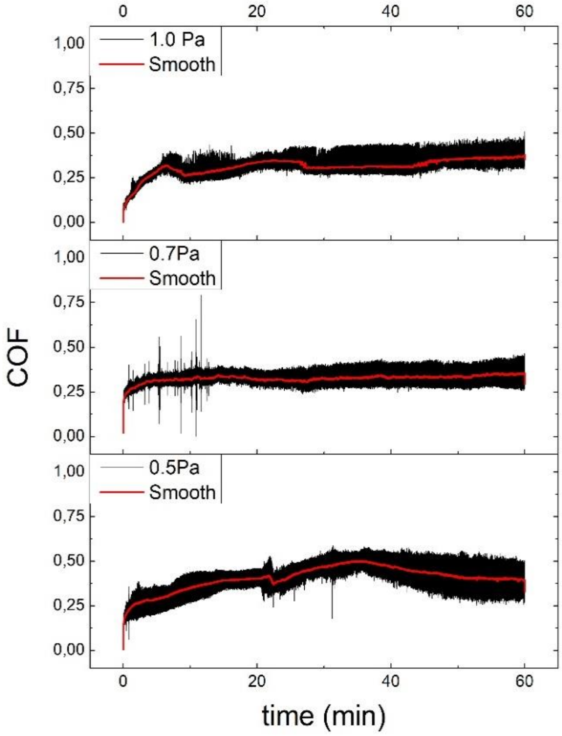

Figure 5.2 Temporal evolution of the coefficient of friction for thin films sputtered at 200 W and different pressure.

5.2.1.2 *Wear track analysis*

After the pin on disc test, mapping profilometries of the wear track were acquired. Such profilometries were carried out using a Dektak XT contact profilometer by Bruker, with a tip of 2.5 μm at 3 mg of normal load. The obtained topographic images were used to estimate the surface changes on the wear track region, an example of the topographical image acquired is presented in Figure 5.3. In the image

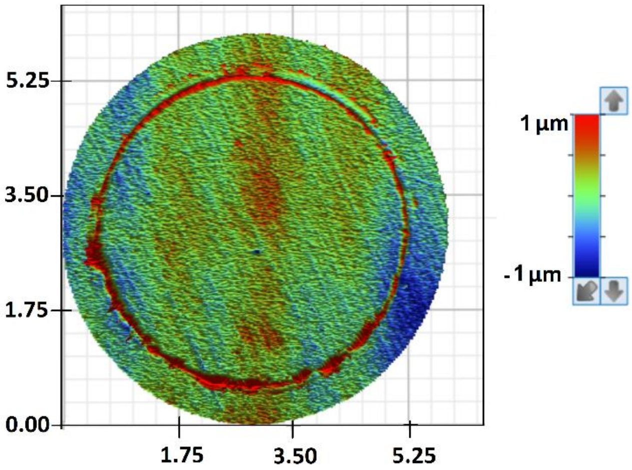

Figure 5.3 Resulting mapping profilometry image of the tungsten nitride thin film (150W and 0.5 Pa) after a pin on disc test under room temperature and humidity.

it is possible to distinguish the circular wear track; such type of image was used to estimate the material loss volume reported in Table 5.1.

Table 5.1 Summary of profilometry results for the tungsten nitride thin films after the pin on disc test at 1.5 N of normal load and 0.02m/s of speed.

Deposition conditions			**Material loss (mm^3)**	**Wear track average roughness (nm)**
Power (W)	Pressure (Pa)			
35	1.0		3.3×10^{-5}	122
150			1.9×10^{-5}	188
200			1.9×10^{-5}	254
	0.7		1.8×10^{-5}	120
	0.5		2.4×10^{-5}	137

Moreover, examples of single profiles for thin films obtained at different deposition conditions are presented in Figure 5.4. Each profile shows a significant change in the surface roughness on the wear track region (highlighted by the dotted red rectangles).

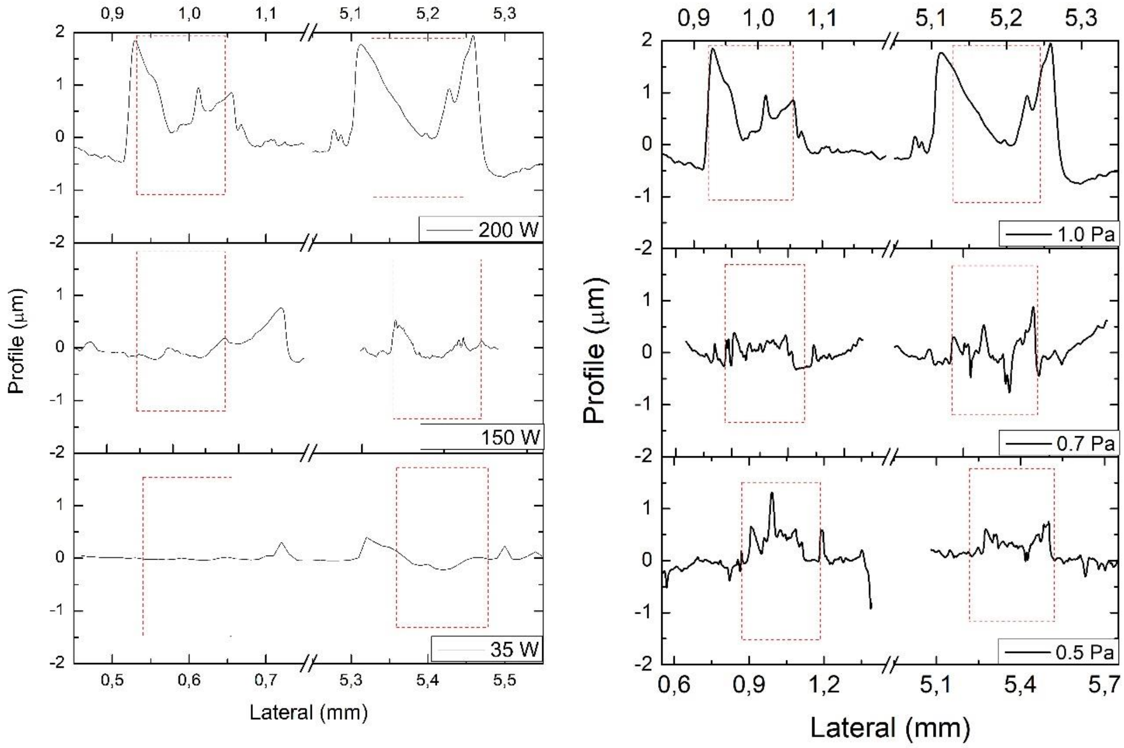

Figure 5.4 Left- Example of average profiles after a pin on disc test at 1.5 N of normal load for tungsten nitride thin films sputtered at 1.0 Pa and different powers Right- Example of average profiles after a pin on disc test at 1.5 N of normal load for tungsten nitride thin films sputtered at 200 W and different pressures.

A summary of the wear track roughness and the material loss is presented in Table 5.1. The material loss values were consistently smaller than the ones found for the substrates, 2.1 x10^{-4} mm^3 for AISI D2 steel and 1.6 x10^{-4} mm^3 for AISI 431 steel. Such values show that the thin film is more resistant to mechanical wear, than any of the tested steels.

Furthermore, mapping profilometries of the counter bodies were acquired, Figure 5.5 shows a common topographical image of a counter body after a pin on disc test in contact with the thin film. In the image one can identify the contact region due to a change of roughness due to transferred material from the thin film to the counter body.

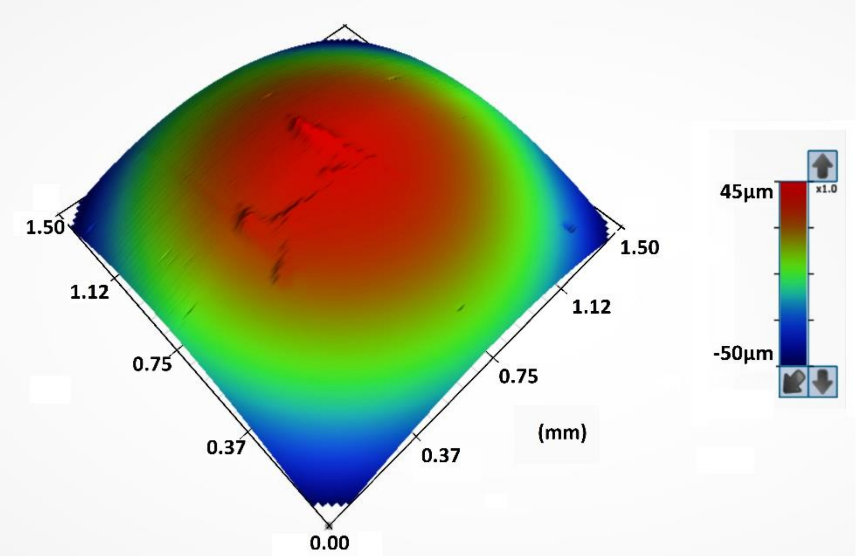

Figure 5.5 Al_2O_3 ball 3D image of profilometry after 60 min of pin on disc test at 1.5 N; in contact with a tungsten nitride thin film.

Additionally, pin on disc tests were performed over AISI 431 coated at 150 W and 0.5 Pa. Figure 5.6 presents the temporal evolution of the coefficient of friction, as for the other systems evaluated the COF presents a sharp change at the beginning of the tests to eventually reaches a steady state. The average COF was 0.28 ±0.09. Moreover Figure 5.7 shows an example of a profile of the AISI 431 coated with tungsten nitride after the pin on disc test at 1.5 N, and room temperature and relative humidity. The region of the wear track is highlighted by red rectangles. The estimated volume of accumulated material was 7.1x10^{-6} ±1.8x10^{-7} mm^3.

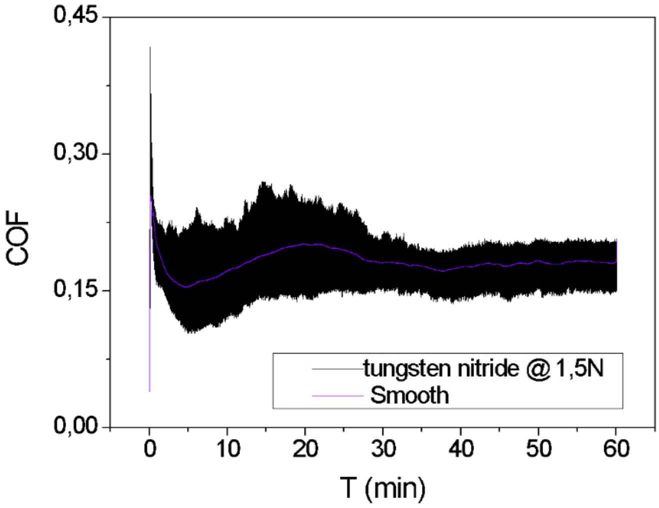

Figure 5.6 Temporal evolution of the coefficient of friction for the system alumina (pin)- tungsten nitride (coated disc) at 0,02m/s of speed at 1.5 N of normal load and, room temperature and relative humidity

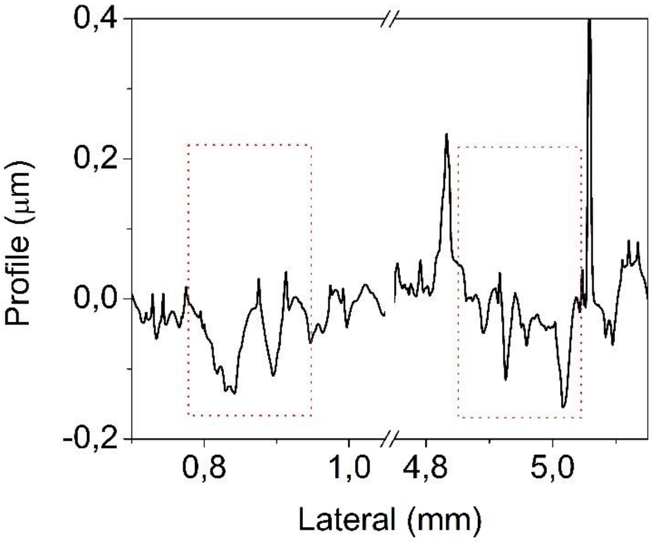

Figure 5.7 Profile of the wear track region for AISI 431 coated with tungsten nitride after a pion on disc test at 1.5 N, and room temperature and relative humidity.

5.2.2 Wear track analysis by scanning electronic microscope and Energy dispersive X-ray spectroscopy.

As for the steel substrate samples, images were acquired by scanning electronic microscopy, Using a Quanta 200FEG microscope with a microanalyzer X INCA Oxford type SDD 80 mm^2. For the thin films, the images were obtained under high vacuum at 20 KeV while for the counter bodies the images were obtained at low vacuum and energies of about 10 KeV.

Figure 5.8 shows SEM images of AISI D2 steel coated with tungsten nitride (a) made at 35W and 1 Pa before the pin on disc test and after the pin on disc test b) a coating made at 35W and 1 Pa, c) 150 W and 1 Pa and d) 200 W and 1 Pa. Each image after the pin on disc test is of a portion of the wear track. Moreover, for b, i.e., the thin film deposited at 35 W and 1 Pa we can observe a difference in contrast between the wear track and the rest of the thin film. The reason for this contrast disparity is a different height, the darker region (the wear track) corresponds to a material accumulation. Such contrast difference is less evident on the thin films c and d hence there is a difference on the overall damage over the surface. Table 5.1 (page 97).

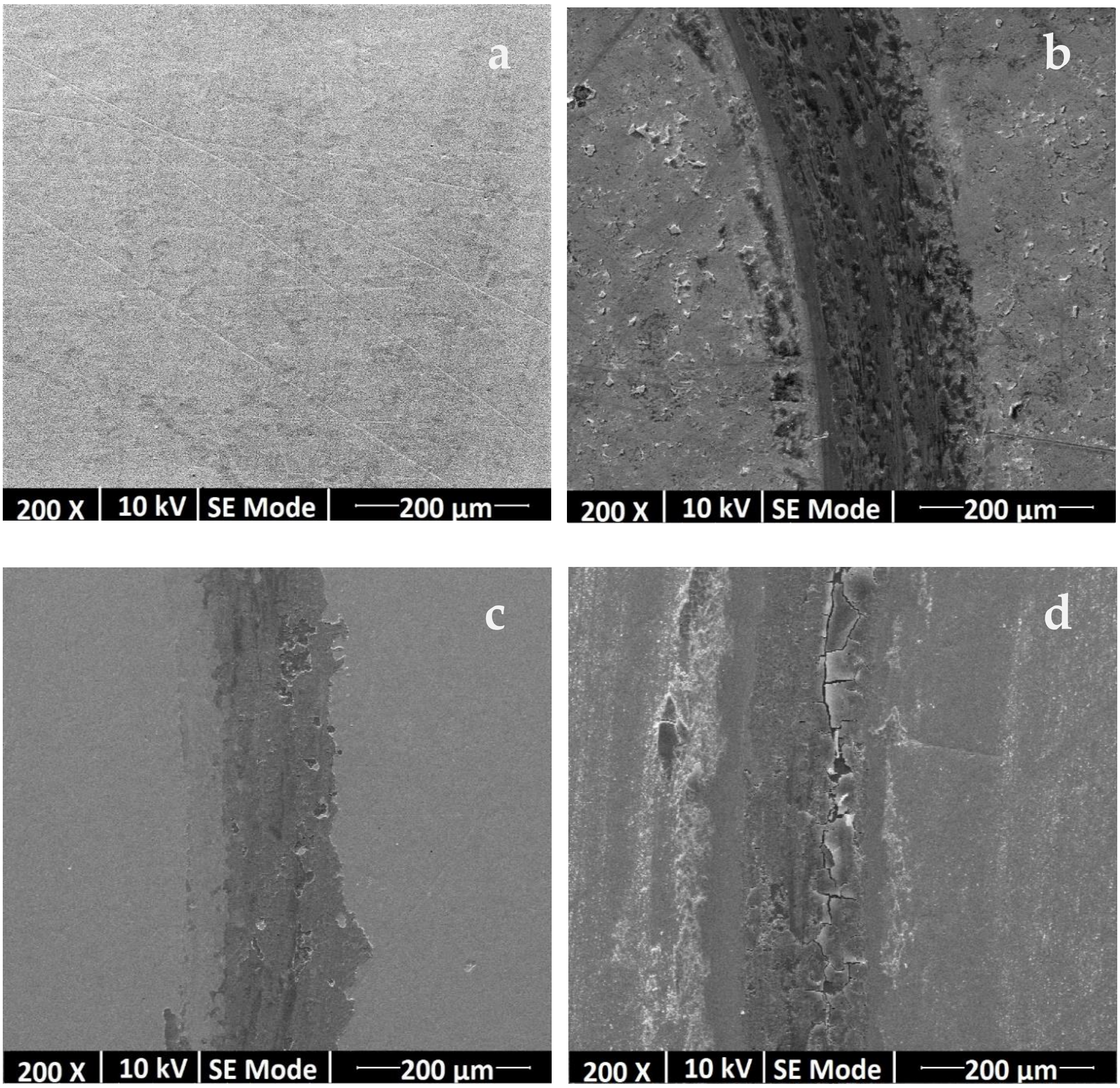

Figure 5.8 SEM images of the tungsten nitride thin films a) before the pin on disc test, and after the pin on disc b) 35 W and 1.0 Pa, c) 150 W and 1.0 Pa, d) 200 W and 1.0 Pa.

Furthermore, for thin films c and d one can remark the presence of fractures and adherence problems. For the c sample, pieces of the thin film have detached from the surface and small cracks can be seen, whereas for the d sample an important crack is visible in all along the wear track region. Such adherence problems could be related to the deposition rate. The thin film density increases with the deposition rate and thereby the thin films stress increases, leading to cracking and fractures when exposed to mechanical efforts. The presence of such fractures can be detrimental for the corrosion resistance.

In general, the wear track presented lines in the direction of the rotation and evidence of material accumulation. EDS tests revealed a difference of detected elements before and after the pin on disc test. On average, for the thin film before a pin on disc test 87 % of W, 3 % of N, 6% of O and 4% C were detected. Such percentages changed after the pin on disc test.

Figure 5.9 presents an EDS mapping for the sample presented in Figure 5.6 c after the pin on disc test. The detected elements and their percentage were: W 76%, N 3 %, O 10%, C 5%, and Fe 6%. The mapping images present the distribution of the elements

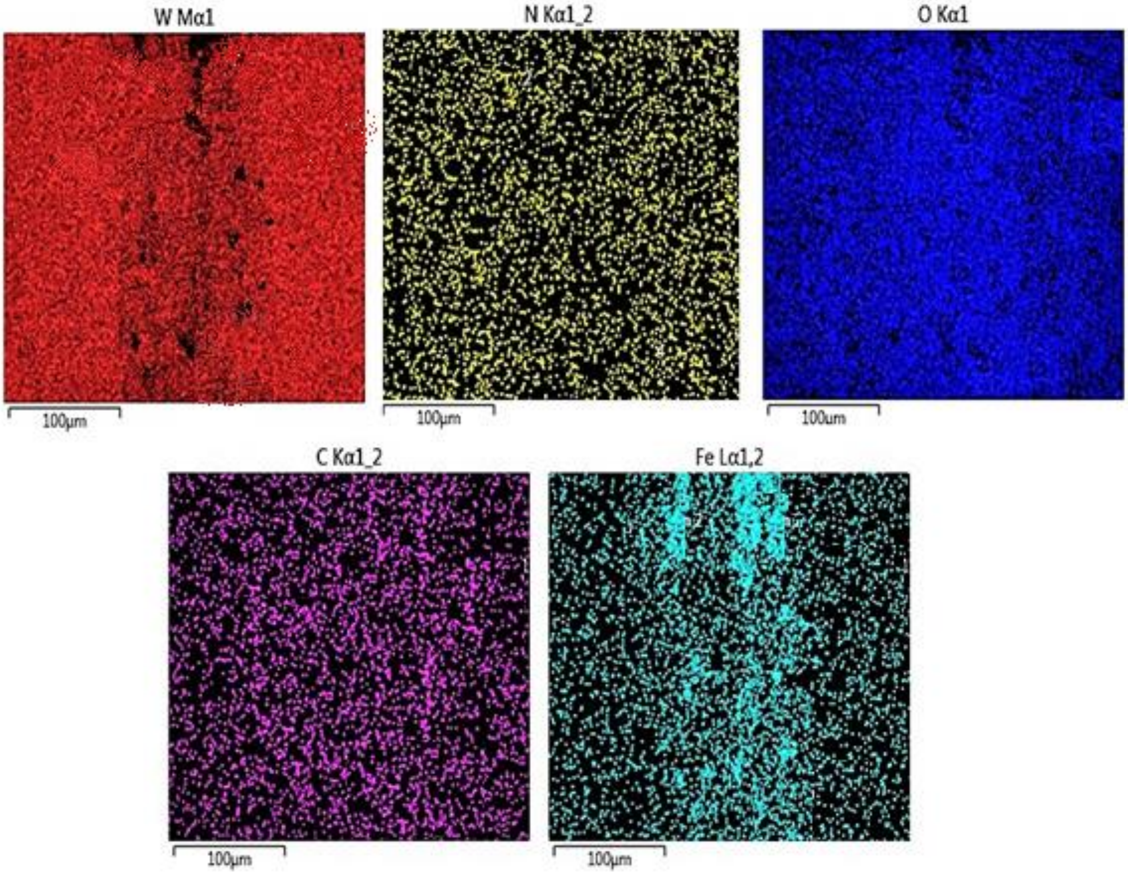

Figure 5.9 Mapping EDS of a tungsten nitride thin film (150 W and 1.0 Pa) after a pin on disc test at room temperature and relative humidity.

over the analyzed region; the various colored region represents the parts where the element was detected, while the black parts indicate the absence of it. Hence for W one can identify small regions over the wear track where the thin films have been detached, such regions match with a larger Fe concentration (the most abundant element on the substrate). Moreover, no aluminum from the counter body was not found indicating that the material accumulation did correspond to material transferred from the counter body to the wear track.

Analogous to the thin film s over AISI D2 steel, Figure 5.10 presents a comparison of an AISI 431 steel sample coated with tungsten nitride sputtered at 150 W and 0.5 Pa before and after the pin on disc test. The wear track region presented lines in the direction of the rotation and material accumulation. Moreover, small fractures in the surrounding area of the wear track were found. Additionally, EDS measurements were performed for the sample before and after the pin on disc test. The detected elements and their percentages were: 84 % of W, 13% of O, 3% of N and 2% of C. A small difference on the percentages of each element was found after the pin on disc test, such values were: 83 % of W, 10% of O, 3% of N and 4% of C.

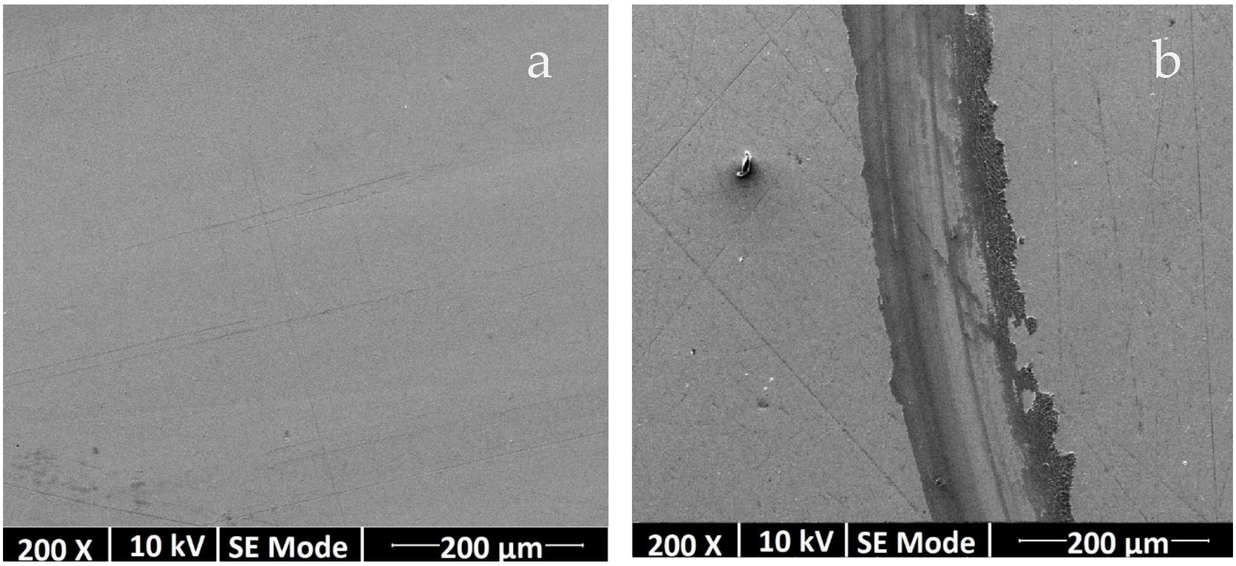

Figure 5.10 SEM image of AISI 431 coated with tungsten nitride at 150 W and 1.0 Pa, a) before and b) after a pin on disc test.

Figure 5.11 shows the element maps of the sample after the pin on disc test. The colored parts represent the points where the element was detected, there was a decrease in the oxygen concentration in the wear track, probably due to the removal of an external oxide film. Moreover, no iron was detected hence, the thin film in the analyzed region was not removed.

Finally, SEM images and an EDS measurement of the counter body were taken. Figure 5.12 presents a SEM image along with the EDS mapping of a counter body after a pin on disc test of AISI D2 coated with tungsten nitride. The SEM image shows the contact point with some accumulated material. This region (red square) was analyzed by EDS, most of the detected elements corresponded to the counter body elements Aluminum (35 %) and Oxygen (55%) with approximately 10% of W from the thin film. Since the thin film material adhered to the counter body and the type of marks found over the wear tracks, one can infer that the thin film wear occurred by third body abrasion.

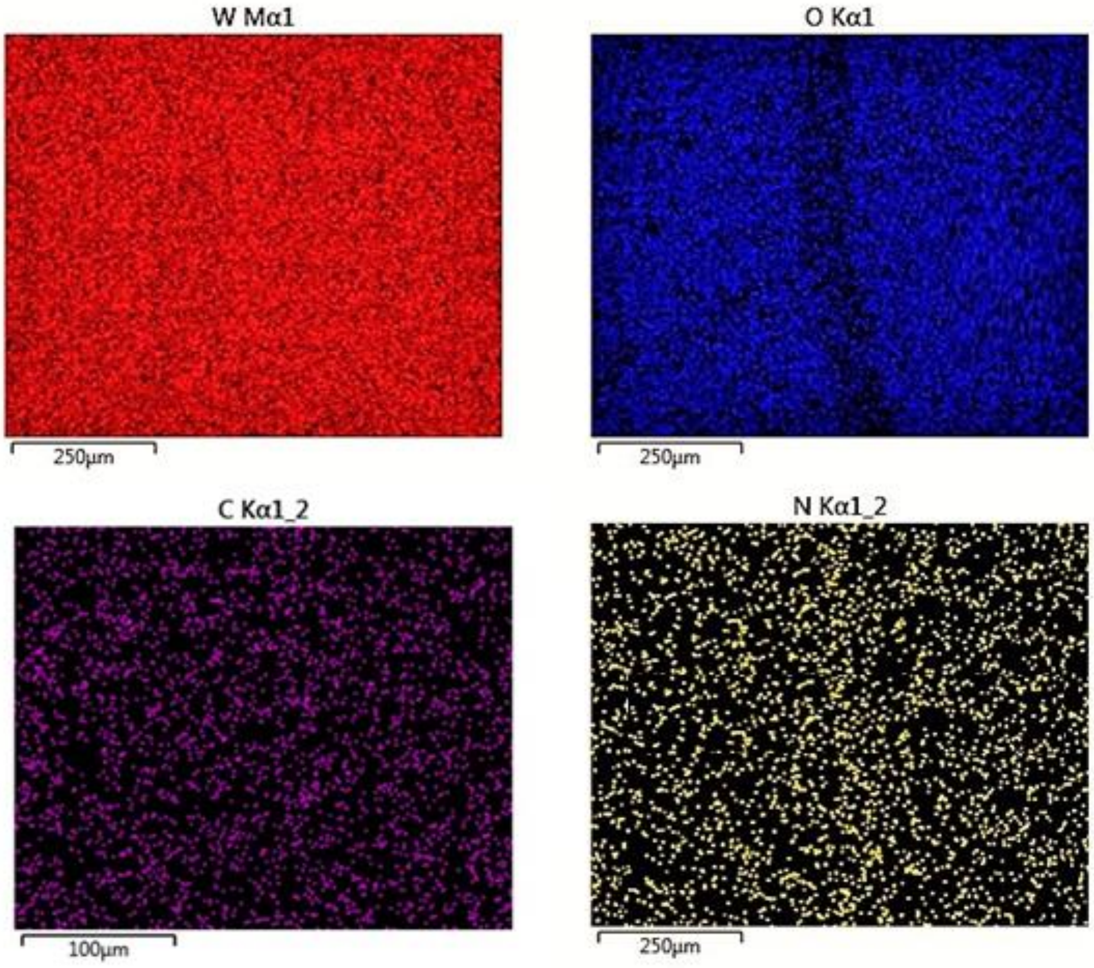

Figure 5.11 EDS mapping images for the elements detected in an AISI 431 steel sample coated with tungsten nitride after a dry pin on disc test.

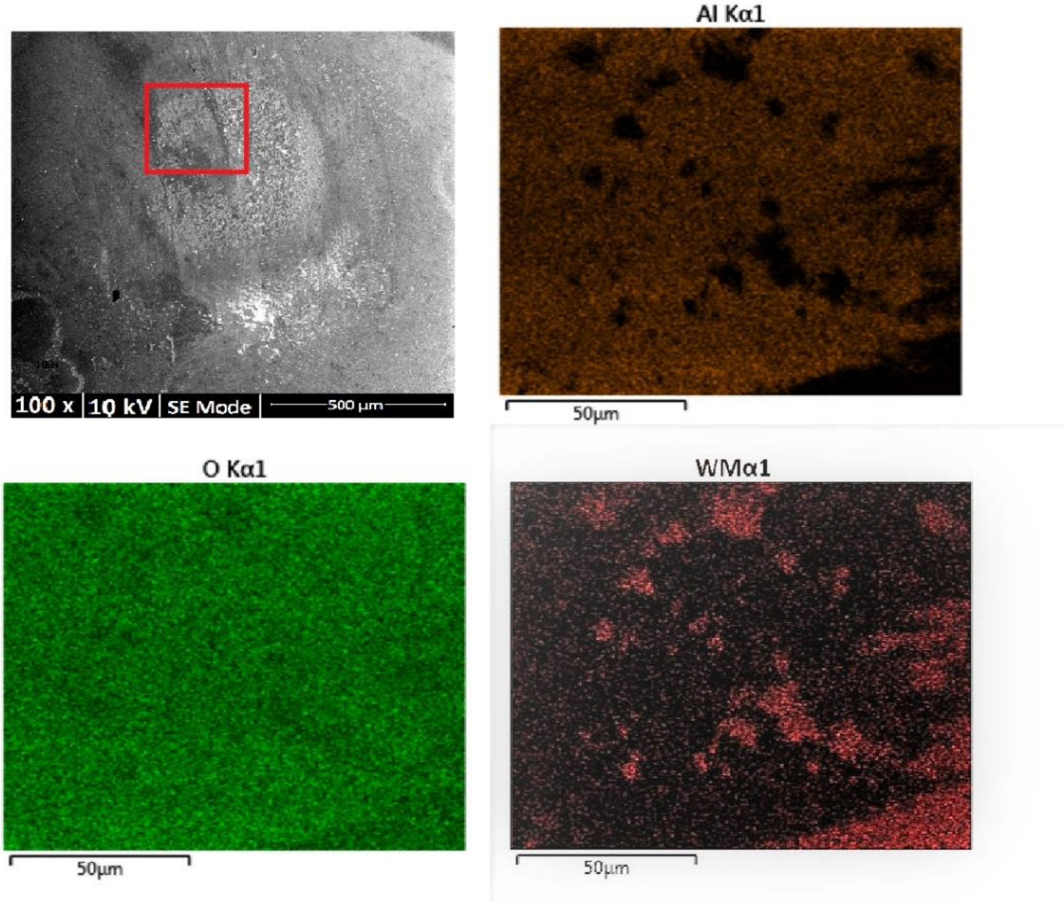

Figure 5.12 SEM image and EDS mapping of a counter body after a pin on disc test in contact with AISI D2 steel coated with tungsten nitride.

5.2.3 Electrochemical tests

This presents the electrochemical evaluation of AISI D2 and AISI 431 steel coated with tungsten nitride. The tests were performed in a three electrode arrangement as described in section 3.2.2.

5.2.4 Open circuit potential and reaction time

The temporal evolution of the open circuit potential of the samples with tungsten nitride coatings prepared at different power and pressure values was recorded. Figure 5.13 displays a comparison the evolution for the uncoated and coated AISI D2 at 1.0 Pa and different powers. Each of the curves show a sharp decrement of the potential, until a steady value was achieved. For steel, the steady value was reached after only 23 minutes, whereas, for the coated steel this took various hours. The OCP steady state value of the thin film s sputtered at 35 W was -0.4 V vs Ag/AgCl or -0.23 V vs NHE after a reaction time of 3 h 40 min. The thin film at 150W reached the steady state at-0.35 V vs Ag/AgCl (-0.14 V vs NHE), with a reaction time about 2h 30 min. Finally, for the sample sputtered at 200 W a steady state was reached at -0.29 V vs Ag/ AgCl (-0.09 V vs NHE) with an estimated reaction time of 3h 40 min. In general, when comparing two electrochemical systems, the system with the higher OCP value is more likely to be corrosion resistant. Therefore, the increment on the deposition power presented a beneficial effect in the OCP.

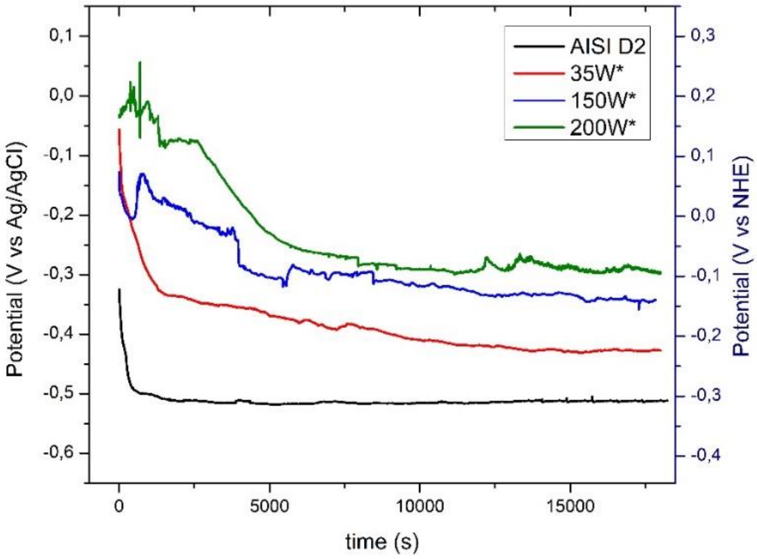

Figure 5.13 OCP curves for AISI D2 steel, and thin films obtained at different deposition powers.

Moreover, the reaction time is significantly larger than the one found for AISI D2. This larger reaction time indicates that the system equilibrium took longer to be reached. This can be due to changes in the thin film surface, which alters the measured interface.

Figure 5.14 shows the E-pH or 'Pourbaix diagram' for tungsten, such a diagram represents the chemical species which can be found in aqueous solution for a given element at a specific E-pH values. The red dots represent the OCP for the different thin film s at pH 4. At these points, tungsten is in the passive region, and this means that the metal will react to form a passive film. Hence, it was expected that the thin film passivated. Nevertheless, the shape of the curve (decreasing values) is commonly associated with systems under corrosion [Celis and Ponthiaux 2012].

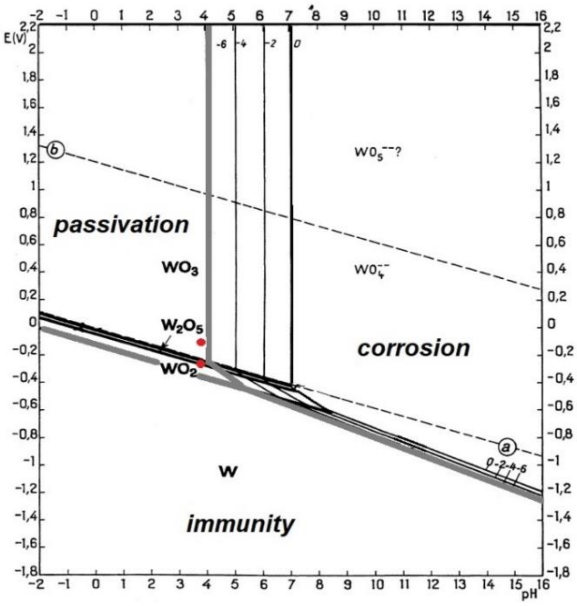

Figure 5.14 E-pH diagram for tungsten [Pourbaix 1974].

Additionally, the effect of the gas deposition pressure used to deposit the coatings on the OCP was studied. The tested samples were heat treated thin film, grown at 200 W of power and either 0.5, 0.7 or 1 Pa. The samples were put in contact with citric acid 10^{-4} M. The temporal evolution of the open circuit potential is presented in Figure 5.15. The curves for the samples at 0.7 and 0.5 Pa presented a sharp decrement at the beginning of the test and achieved steady state at around –0.47 V vs Ag/AgCl (–0.26 V vs NHE), a smaller value than that one found for the thin film obtained at 1 Pa. The estimated reaction times for the 0.7 and 0.5 Pa samples were 25 min and 48 min, respectively. Analogous to the thin films deposited at different powers, the steady

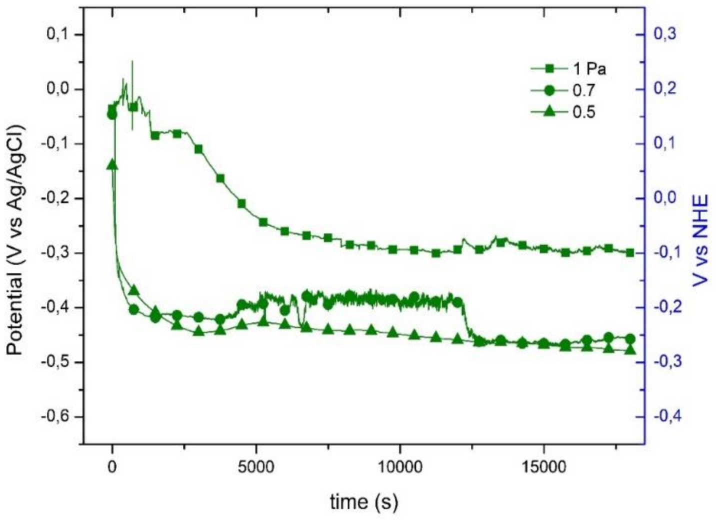

Figure 5.15 OCP curves for AISI D2 steel, and thin films obtained at different deposition pressure.

state value was located in the passivation region of tungsten. Nevertheless, the decrease in the OCP curve is commonly reported for systems under corrosion.

Moreover, to estimate the effect of the substrate on the corrosion behavior of the tungsten nitride thin films a substrate of conductive silicon (4-6 Ωcm) and another of AISI 431 were coated with tungsten nitride at 150 W and 0.5 Pa. The Comparisons of the temporal evolution of the OCP for AISI 341 steel uncoated and coated and silicon uncoated and coated are presented in Figure 5.16. The curves show a sharp increment at the beginning of the test. The coated AISI 431 sample achieved a steady OCP value after 1 h 4 min. This was a larger time than the one for the uncoated steel (23 min); hence the passivation process took longer. The measured OCP for the coated sample was -0.04V vs Ag/AgCl (0.15 V vs ENH) a similar value than that found for the uncoated sample. Furthermore, the uncoated silicon sample achieved a steady state at about 0.06 V vs Ag/AgCl (0.26V vs NHE), and for the coated sample had an OCP value was 0.03V vs Ag/AgCl (0.23V vs NHE) at a t_{react} of 30 min. Such OCP represents a system which tends to passivation, indicating that the coatings deposited on conductive silicon and AISI 431 could passivate.

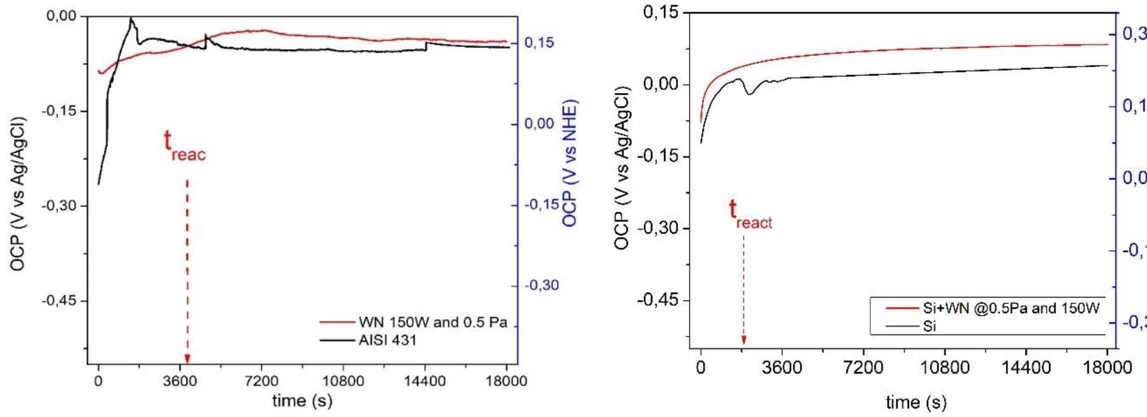

Figure 5.16 Temporal evolution of the OCP for -left-AISI 431 steel uncoated and coated -right- un coated and coated conductive silicon in contact with 10^{-4} M citric acid.

5.2.4.1 *Electrochemical impedance spectroscopy*

Electrochemical impedance spectroscopy (EIS) measurements were carried out with a 10.0 mV perturbation in a frequency range from 10^5 Hz to 10^{-2} Hz. For each decade of frequency, at least three measurements were made. The obtained response was fitted using the equivalent circuit method. The Z circuit fitting tool in the PS Trace 5.8 software was used applying the Levernberg-Marquarat algorithm. An area of 0.45cm^2 was exposed during the experiments.

Once the system achieved steady state, the electrochemical impedance spectroscopy test was performed. Figure 5.17 shows in the left-handed graph the Nyquist diagrams for the uncoated and coated AISI D2 steel. The coatings were made at different plasma powers and 1.0 Pa of gas pressure, and the right-handed figure presents the modelled Nyquist diagram for the samples just described. Each diagram is composed by two semicircles. The first semicircle represents the electrolyte resistance whereas the second can be used to evaluate the sample corrosion resistance. To evaluate the material resistance values the data were fitted using the equivalent circuit method. The proposed circuit is presented in Figure 5.18. The circuit contains constituted by the same elements as for uncoated AISI D2 steel and has two RC components. The first RC parallel circuit represents the ohmic resistance of the solution between the working and the reference electrodes, modified by the geometry and the distance between the electrodes. The second RC component, R_2 corresponds to the polarization resistance of the material (R_p); the Q element is a constant phase element (CPE).

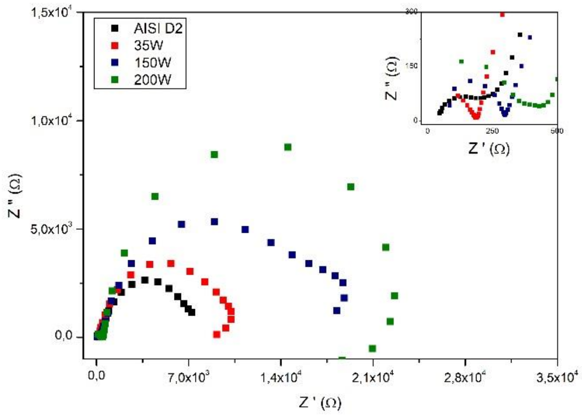

Figure 5.17 Nyquist diagram for the EIS of AISI D2 steel uncoated and coated (1.0 Pa and different powers) in contact with the citric acid 10^{-4} M solution.

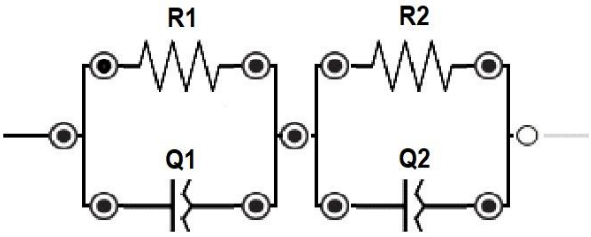

Figure 5.18 Equivalent circuit for the EIS response of coated AISI D2 steel in contact with 10^{-4} M citric acid solution.

Moreover, a similar response was found for thin films deposited at different pressures and 200 W of power; Figure 5.19 presents the Nyquist diagrams (left-handed image) and resulting Nyquist diagram of the modelled data from the left-handed figure (right-handed). The results were as well fitted using the previously described equivalent circuit in Figure 5.18.

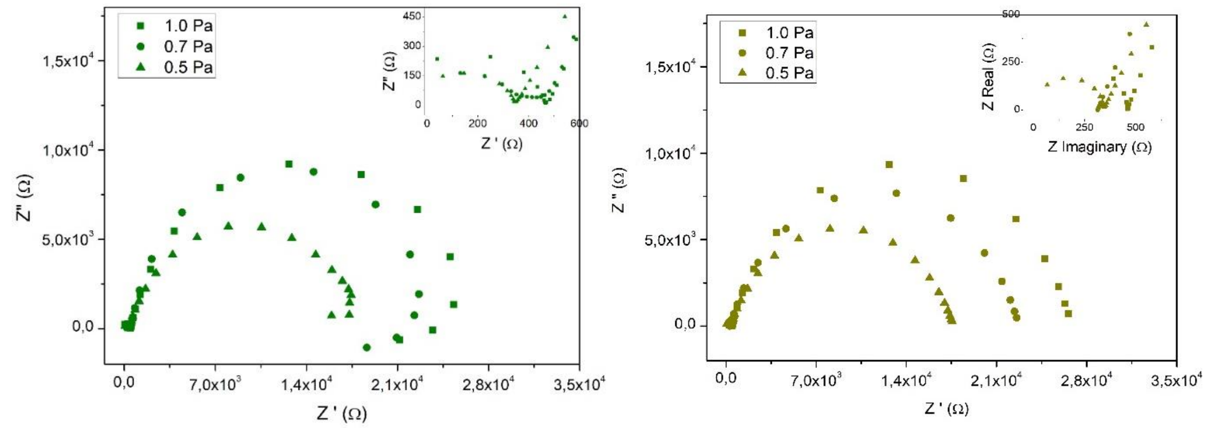

Figure 5.19 Nyquist diagram for the EIS of AISI D2 steel coated at 200 W and different pressures in contact with the citric acid 10-^{4} M solution.

The obtained resistance values were used to calculate the specific corrosion resistance (r_{corr}) and the corrosion current (i_{corr}), and Table 5.2 presents a summary of the values. The r_{corr} was slightly larger for the coated samples, moreover, the r_{corr} value increased with the deposition pressure used. Nevertheless, these values correspond to a system under corrosion, hence, the tungsten nitride partially protects the substrate.

Table 5.2 Summary of corrosion resistance and specific corrosion resistance for AISI D2 coated with tungsten nitride.

Power (W)	Pressure (Pa)	R_p(kΩ)	r_{corr} (kΩcm^2)
AISI D2		7.3	3.3 ± 1.0
35	1.0	8.6	3.9 ± 0.2
150		17.1	7.6 ±0.6
200		26.4	12.1 ±0.3
	0.7	22.7	10.1 ±0.3
	0.5	17.7	7.2 ± 0.5

Moreover, EIS measurements were performed for AISI 431 steel and conductive silicon coated with tungsten nitride sputtered at 150 W and 0.5 Pa. Figure 5.20 presents a comparison of the obtained Nyquist diagram for the coated and uncoated samples. Each of the analyzed samples presented similar Nyquist diagrams composed of two flattened semicircles. The equivalent circuit used to fit the results was the one proposed in Figure 5.18. The R_P of the thin film deposited on the AISI 431 was 410 ± 50 kΩ, which corresponds to a r_{corr} of 207 ±22 kΩ cm^2, such specific polarization resistance corresponded to a passive system with an i_{corr} of 5.8x10^{-8} A/cm^2. Such values are of a better passivated surface than for the uncoated steel. The r_{corr} estimated value represents the passivation resistance value of the system (r_{pass}). As for the silicon samples, the estimated R_P value was 188MΩ ± 5MΩ (84 MΩ cm^2) for the uncoated sample and for the 617 ± 20 kΩ for the coated sample. The R_P value for the coated sample corresponds to a r_{corr} of 277 kΩ cm^2 and again this specific polarization resistance corresponds to a passive system with an i_{corr} of 8.6x10^{-8} A/cm^2.

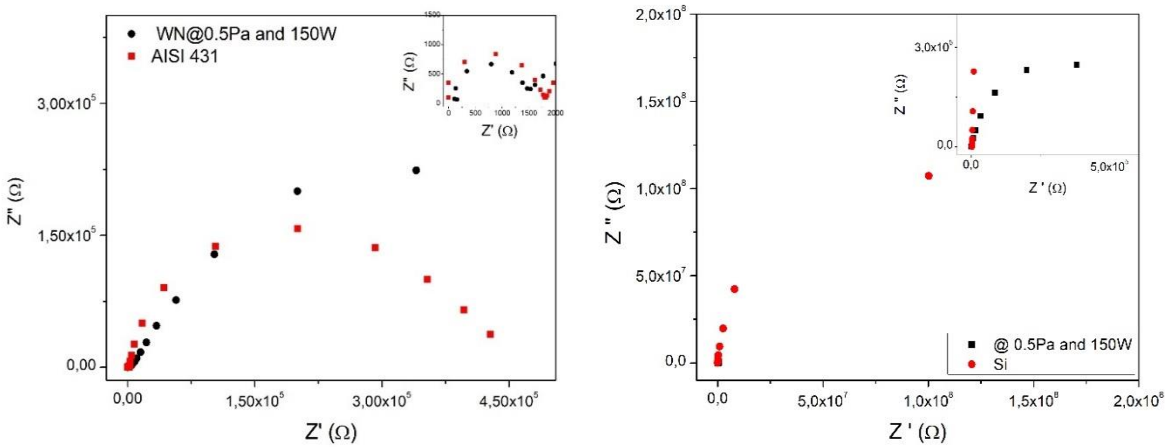

Figure 5.20 Nyquist diagram for the EIS of -right- AISI 431steel uncoated and coated and -left- silicon uncoated and coated in contact with the citric acid 10^{-4} M solution.

The specific corrosion resistance found for the thin film in both AISI 431 steel and Si were very similar, 207 and 277 kΩ cm^2. Hence, one can infer that such a value truly corresponds to the corrosion resistance value of the tungsten nitride thin film.

5.2.5 SEM and EDS

To determine if surface changes occurred due to the electrochemical tests, SEM images and EDS measurements on the thin films before and after the electrochemical tests were. Figure 5.21 shows representative SEM images of the AISI D2 coated samples as deposited and after the electrochemical tests. Figure 5.21a is an example of a coating as deposited, such image shows a smooth and uniform surface. Figure 5.21 b, c and d show the changes of texture surface of the samples. For the coating deposited at 35 W and 1 Pa (b) a large incidence of corrosion areas was observed. The total corroded area diminished when the power increased, as observed on c and d (deposited at 150W and 200W respectively). This indicates that an increment on the plasma power helps to diminish the corrosion regions helping to control the corrosion damage.

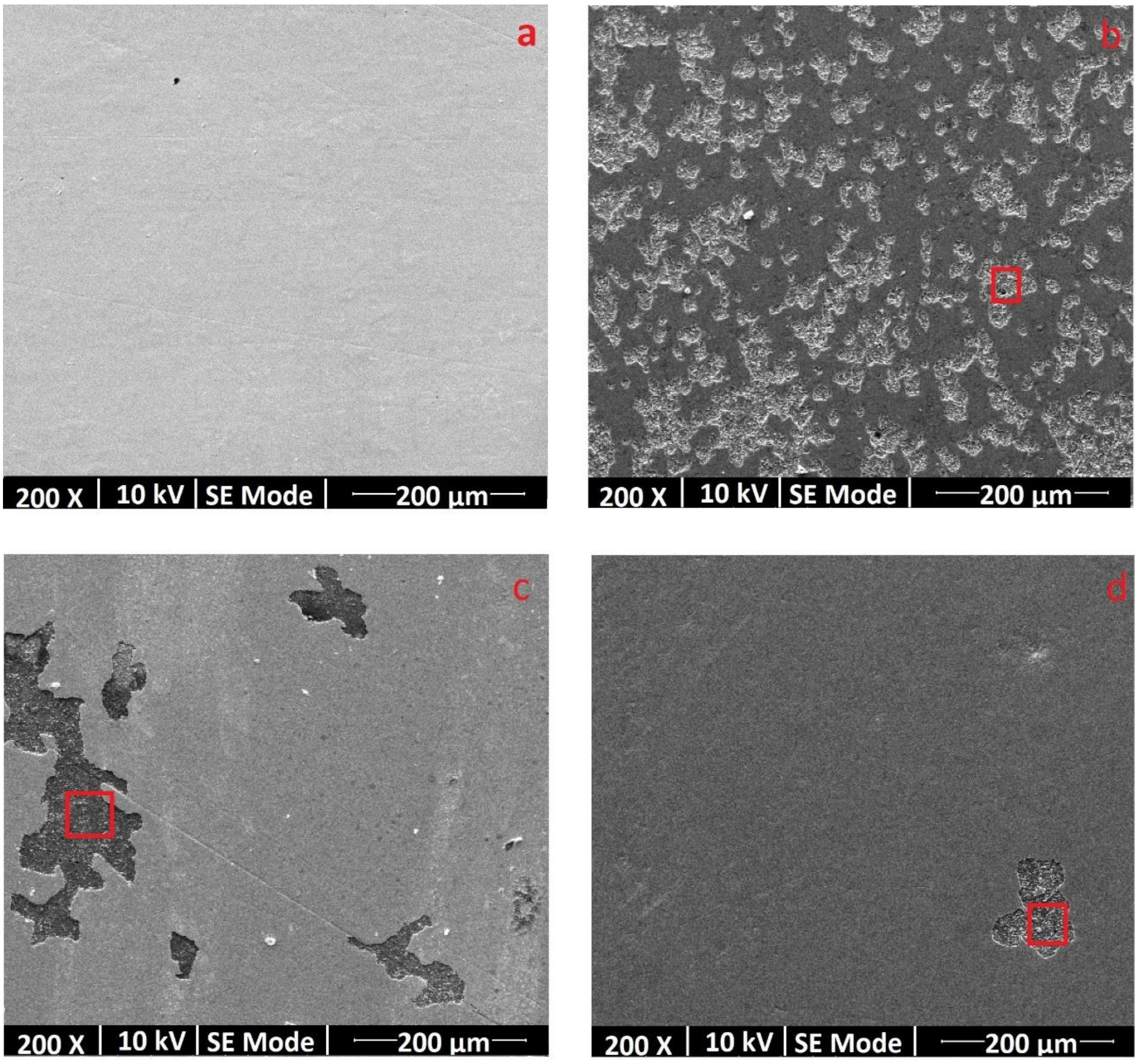

Figure 5.21 SEM images of AISI D coated with tungsten nitride at (a) 150 W and 1.0 Pa before electrochemical test (b) 35 W and 1.0 Pa after electrochemical tests (c) 150 W and 1.0 Pa after electrochemical tests (d) 200 W and 1.0 Pa after electrochemical tests.

Furthermore, EDS measurements were performed and for the thin film as deposited the average composition was 87 % of W, 3 % of N, 6% of O and 4% C. As for the samples after the electrochemical tests, EDS measurements were performed on the regions of the texture (red squares), such regions had a different composition than that of the as deposited samples. The analyzed regions in b, c and d had similar compositions. The average of such compositions was: Fe 75%, Cr 9%, O 8%, V 3%, C 3%, and W 4%. The most abundant elements correspond to the substrate, hence in such regions the thin films had been almost completely removed. On the area where no texture changes were detected the composition of the surface corresponded to that of the sample before the electrochemical test.

Figure 5.22 presents a comparison of the EDS spectrum of the AISI D2 steel as coated and after the electrochemical test, for the coating as deposited only tungsten, oxygen and nitrogen from the coating were found but for the coating after the electrochemical test elements from the substrate, Fe, Cr and V were detected, confirming that part of the coatings has been removed.

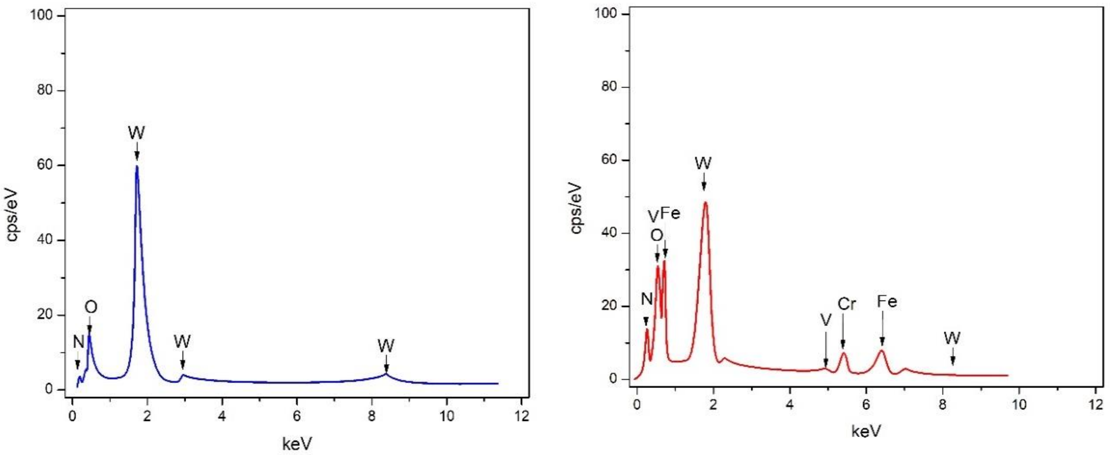

Figure 5.22 EDS spectrum for AISI D2 coated with tungsten nitride -left- as deposited and -right- after electrochemical test.

Furthermore, Figure 5.23 shows the SEM images of AISI 431 steel coated samples before and after the electrochemical tests. The detected elements in both cases were the same W, O, N, Ar, and C. The percentages for the sample before were 84%, 9%, 4%, 1% and 2% respectively. A not significant difference was found on the percentages after the electrochemical test with W 81%, O 12%, N 3%. Ar 1%, and C 3%. The elements distributions were kept similar, Figure 5.24 presents the EDS mapping of the thin film as deposited over AISI 431.

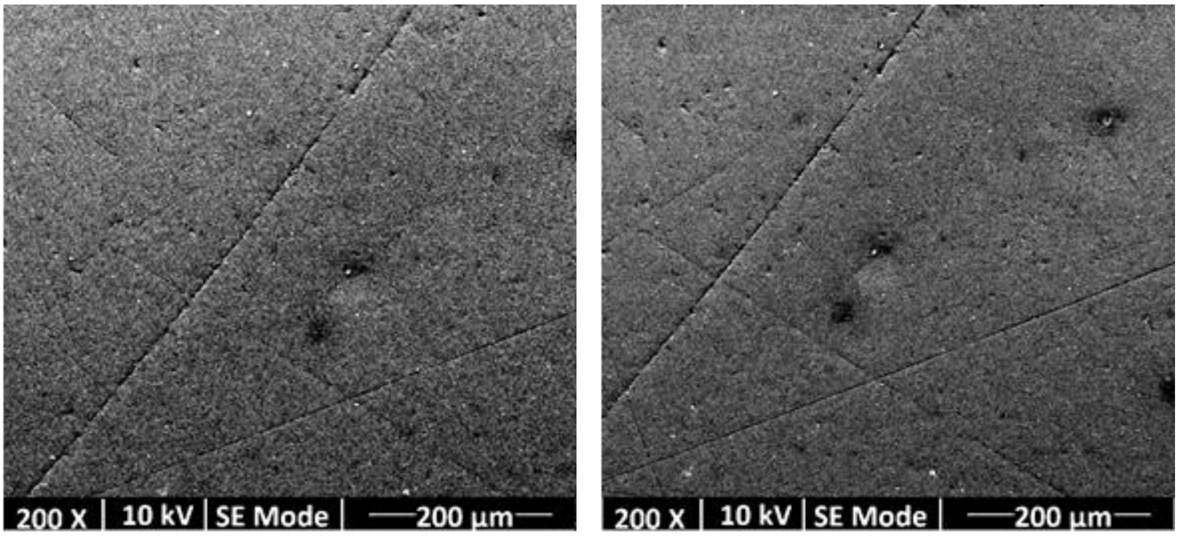

Figure 5.23 SEM image of AISI 431 coated with tungsten nitride, left hand, as sputtered and right hand after the electrochemical tests.

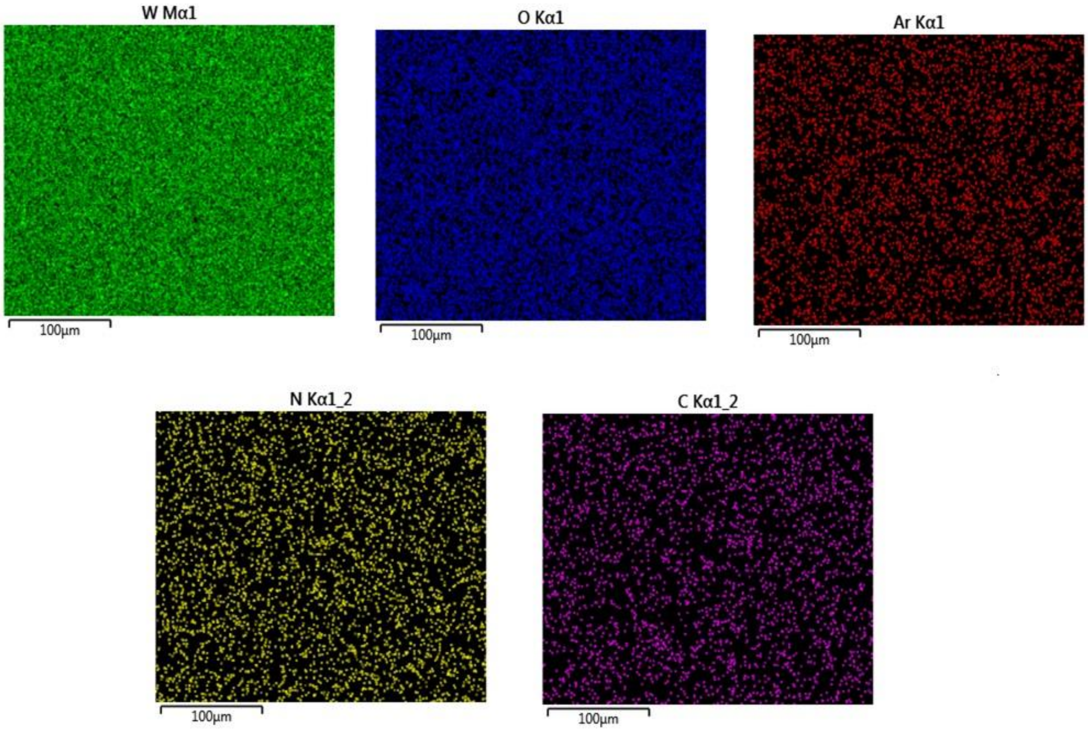

Figure 5.24 EDS mapping of AISI 431 coated with tungsten nitride as deposited.

Similarly, to the thin films obtained on steel, SEM images and EDS measurements were performed on the thin films deposited on the conductive silicon. Figure 5.25 shows the SEM images for the coated silicon sample before and after the electrochemical test. Both images show a uniform surface without significant changes in the texture. Figure 2.26 is of the EDS mapping of the sample after the electrochemical tests, the images show an even distribution of the element in the thin film The weight percentages of each element were 84% W, 10% O, 3% N, 2% C, and 1% Ar, for the thin film as deposited and 82% W, 12% O, 3% N, 2% C, and 1% Ar after

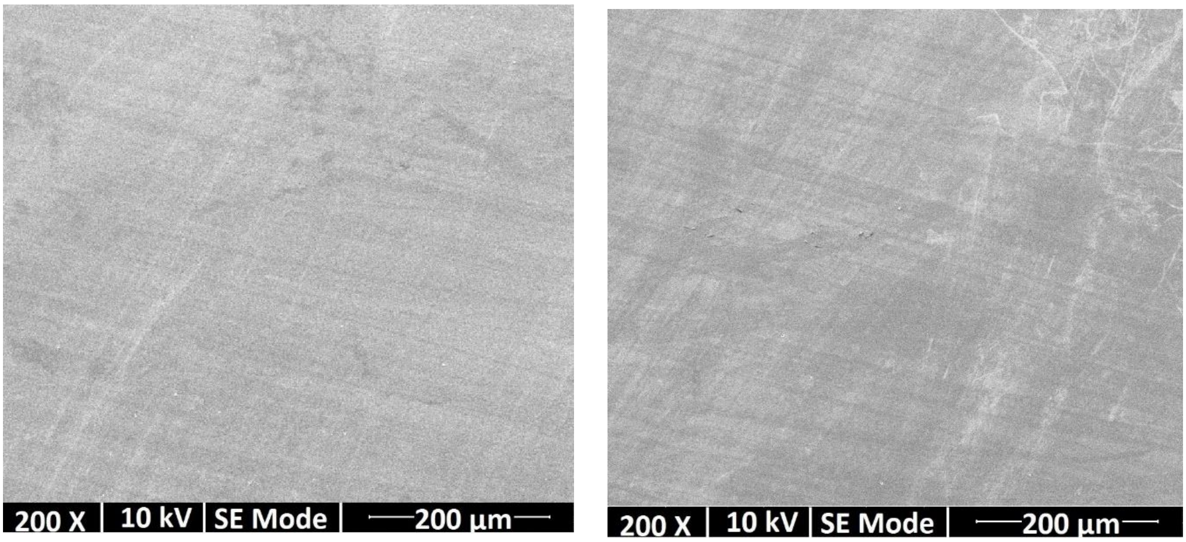

Figure 5.25 SEM images of conductive silicon coated with tungsten nitride, left hand, as sputtered and right hand after the electrochemical tests.

the electrochemical test. One can consider that the amounts of the elements in the thin films deposited on AISI 431 steel and silicon were virtually unaltered by the electrochemical test. Nevertheless, the thin films deposited over AISI D2 presented localized corroded regions. The total area of the corroded region was found to decrease for the films deposited at the higher plasma powers.

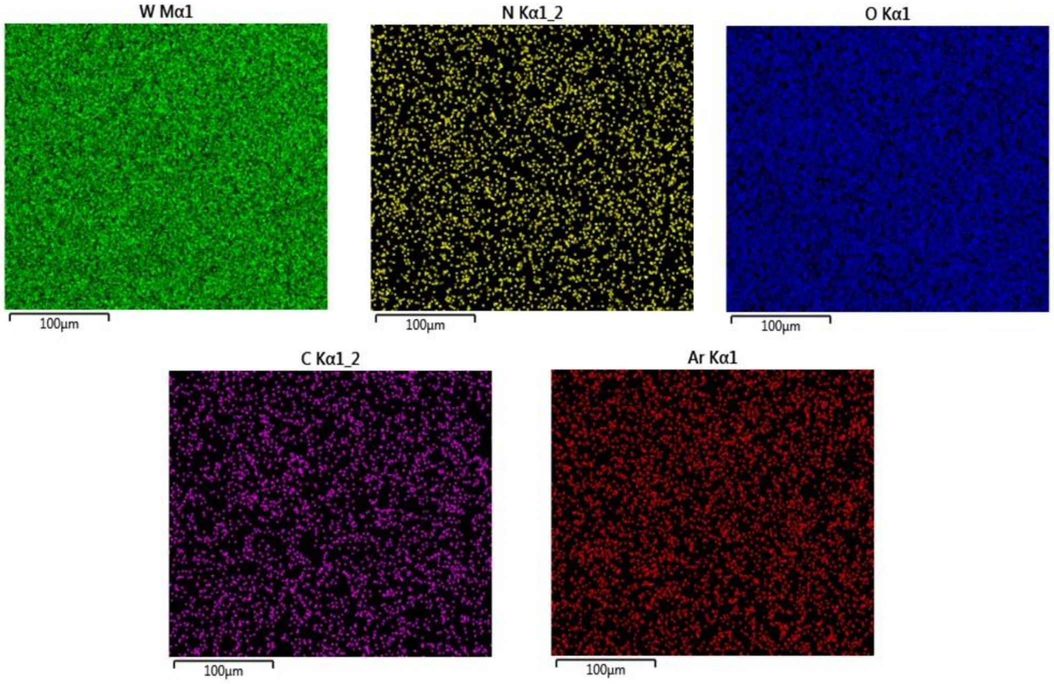

Figure 5.26 EDS mapping of conductive silicon coated with tungsten nitride after the electrochemical test.

5.2.6 Thin film adherence and buffer layers.

Due to the prevailing adherence problems, explained in chapter 4, and the recurrent corrosion points of the thin films deposited on AISI D2 steel, four different buffer layers were explored. Each type of buffer layer was deposited on the AISI D2 substrates prior to the deposition of the tungsten nitride coatings. The buffer layers thickness was about 10 nm, the elected materials were tungsten, platinum, silicon, and platinum. The tungsten was used as buffer layer since it is the base metal for the nitride, the use of the base metal of hard coatings deposited by sputtering has been reported to help enhance the adherence. Silicon, platinum and carbon are materials known to have good corrosion resistance; hence *a priori* they could help to protect the substrate surface from potential corrosion.

Tungsten, silicon, and carbon layers were deposited by rf sputtering magnetron. As for platinum, a DC sputtering metallizer was used. After the buffer layer was deposited the tungsten nitride thin film was deposited by rf magnetron sputtering at 150W and 0.5 Pa, furthermore the thin films where heat treated at 500°C for 90 min under nitrogen atmosphere. Finally, a region of the sample was put in contact with a 10^{-4} M aqueous citric acid solution. The changes over the surface were investigated by SEM and EDS using as a guide some notable mark in the sample surface. As a reference SEM and EDS measurements were performed before the deposition for each sample.

Tungsten buffer

The tungsten buffer layer was sputter deposited at 150 W and 0.5 Pa using pure Ar for 2 min, followed by the deposition of the tungsten nitride thin film by simple replacing the Ar with a mixture of N_2 12% in Ar. Figure 5.27 shows the SEM images of AISI D2 uncoated and the EDS mapping of the region in the right-handed micrography. The EDS reveled the composition and distribution of the elements in the

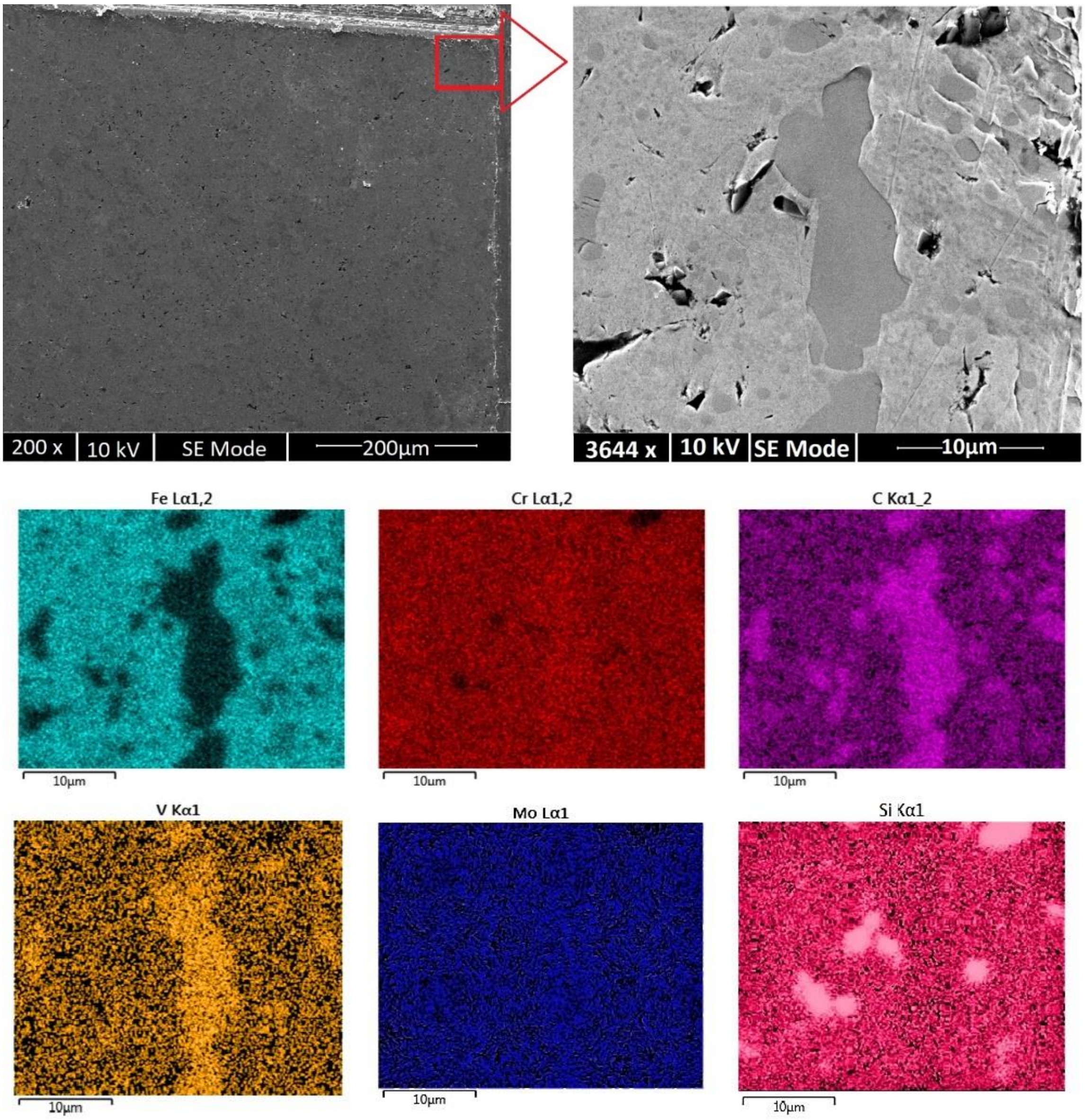

Figure 5.27 Top SEM images of uncoated AISI D2, bottom EDS mapping of the sample.

analyzed region. The elements and their percentages were Fe 76.5 %, Cr 15.5%, C 4.5%, V 1.4%, Si 1.5%, and Mo 0.7%. The distribution showed iron deficiency (less intensity color) regions; moreover, such regions were rich in vanadium and carbon indicating the probable presence of carbides in such regions.

After the deposition of the tungsten nitride coatings, SEM images of the sample were acquired. Figure 5.28 shows a smooth and uniform surface of the samples. Moreover, EDS tests were performed to identify the main elements, with their percentages found to be for W 88%, O 7.5%, for N 4.5%.

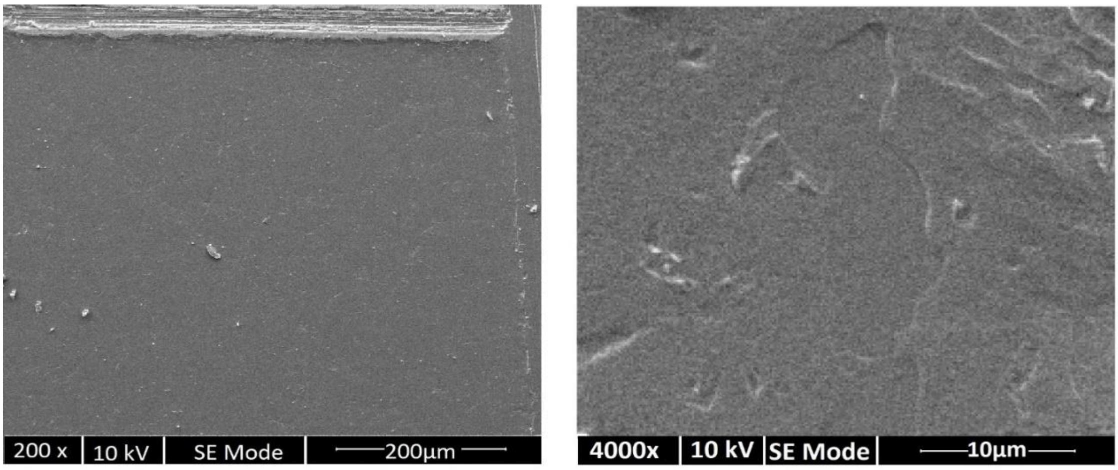

Figure 5.28 SEM images of AISI D2 coated with tungsten buffer layer + tungsten nitride.

Finally, the sample was put in contact with the aqueous solution of citric acid for five hours. Subsequently, SEM images and EDS tests were performed. Figure 5.29 shows the images and mapping EDS of the sample. In the left-handed image it is possible to distinguish a small, damaged region, a close up to this region is given in the right-handed image. The EDS maps show the distribution of each detected element. The elements that correspond to the thin film are virtually absent from the region where a change in the texture is notable. The zones where the thin film was removed correspond to the areas of carbon.

As a way to comparison, similar experiments were performed using a substrate of AISI 431 steel., Figure 5.30 shows the SEM images of the uncoated sample, coated and after being in contact with the citric acid solution. In the first image one can see a reasonably uniform surface on the nearby of the mark, some small dark points (valleys on the surface) can be identified as a part of the surface texture. EDS measurements of the uncoated substrate detected the following elements Fe 78%, 17% Cr, 3% Ni and 2% C.

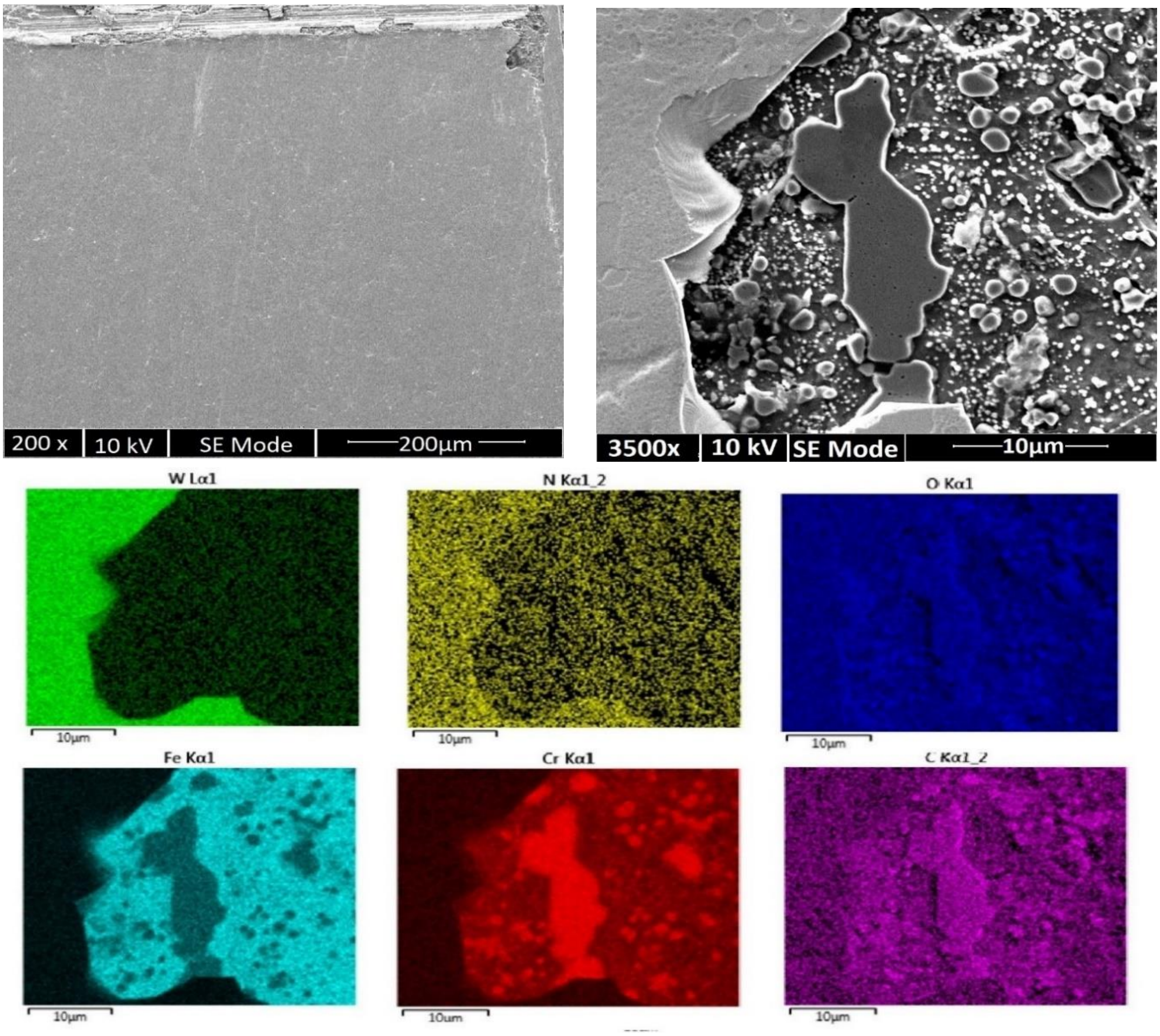

Figure 5.29 SEM images and EDS mapping results of AISI D2 coated with a tungsten buffer layer followed by tungsten nitride after being exposed to a 10^{-4} citric acid aqueous solution.

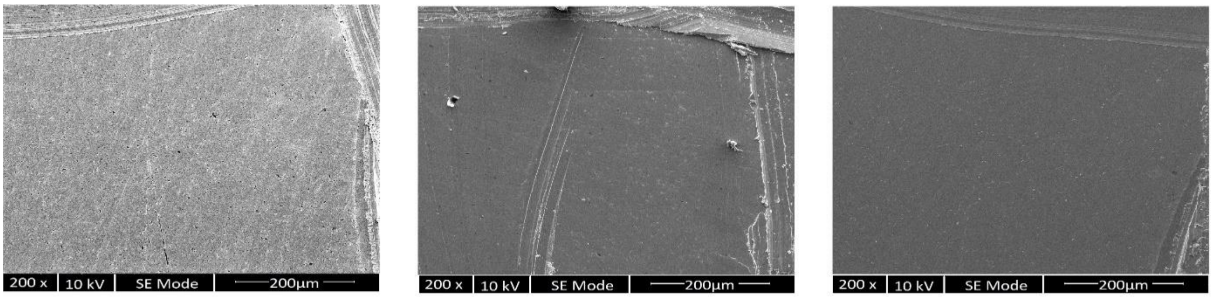

Figure 5.30 SEM images for AISI 431, left to right, uncoated, as coated and coated after being exposed to citric acid solution.

For the AISI 431 sample coated with the tungsten buffer layer and the tungsten nitride thin film, the EDS test gave a composition of W 89%, O 7%, and N 4%. The same elements at similar percentages were found for the sample after being exposed to citric acid. Hence, for this sample the use of the buffer layer of tungsten and the tungsten nitride film effectively protected the substrate's surface from corrosion, moreover, one can confirm that the presence of the buffer layer does not produce the delamination of the tungsten nitride layer seen in the AISI D2 substrate.

Silicon buffer over AISI D2

Since the thin films deposited over silicon had good electrochemical characteristics the use of a silicon layer as buffer between the substrate and the thin film was explored. The silicon layer was deposited by rf magnetron at 1Pa and 200W using pure Ar in the Plasyss system, immediately followed by the sputtering of the tungsten nitride thin film. Figure 5.31 contains the SEM images of AISI D2 sample coated with the silicon buffer the tungsten nitride thin film before and after being in contact with the citric acid solution. The left-handed side image is of the thin film as deposited, the sample has a and smooth surface with no large visible defects. However, for the sample after contact with the acid, one can see a change on the surface texture in some regions. EDS measurements of these parts (Figure 5.32) showed the presence of iron from the substrate indicating that the thin film had been partially. The average weight percentage of each element on the corroded sample were 76% W, 12% O, 2% N, 4% C and 6% Fe. The EDS maps show again corrosion regions, in such corrosion regions the elements of the buffer layer and tungsten were not detected, once again the presence of carbon an iron from the substrate was detected.

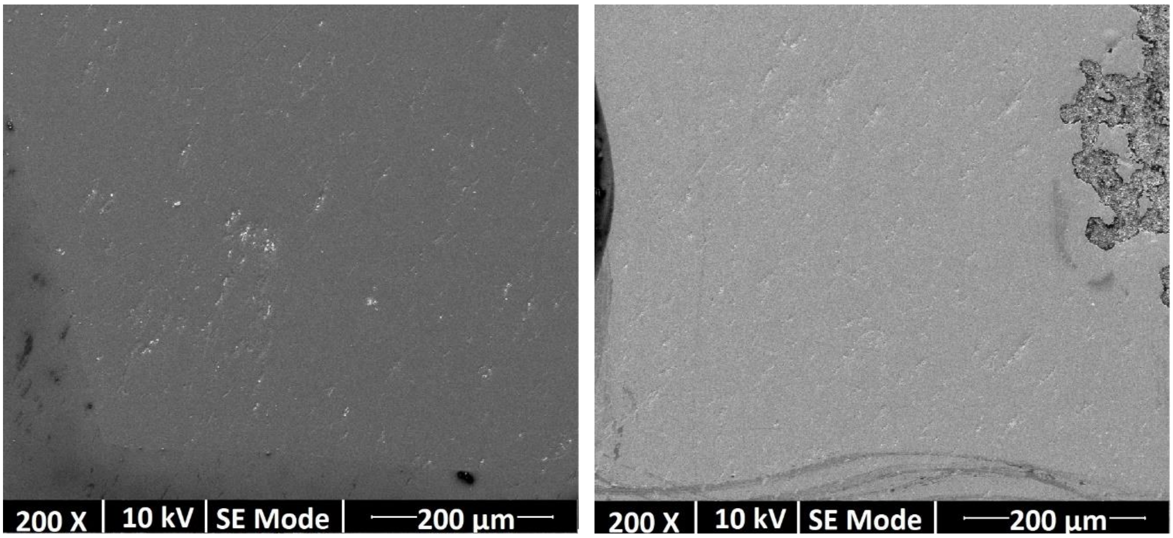

Figure 5.31 SEM image for AISI D2 coated with a silicon buffer layer and tungsten nitride (left)as coated an (right) after exposed to 10^{-4} citric acid aqueous solution.

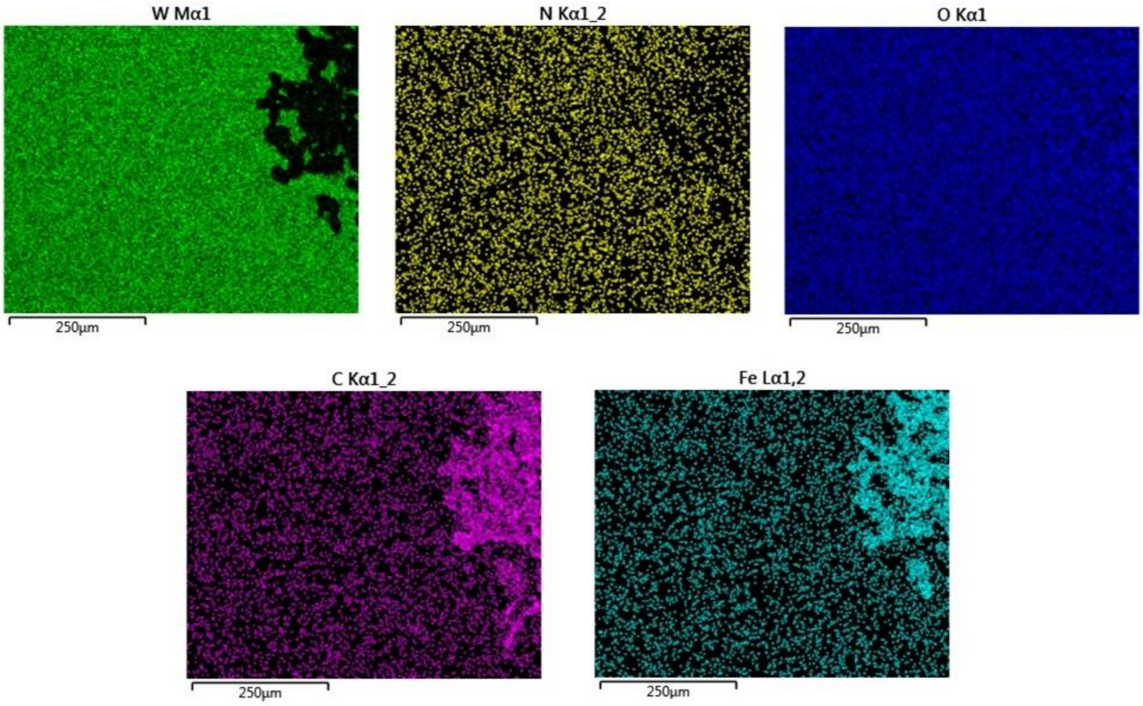

Figure 5.32 Mapping EDS for AISI D2 coated with a silicon buffer layer and tungsten nitride after contact with 10^{-4} citric acid aqueous solution.

Platinum buffer over AISI D2

Additionally, the use of a platinum buffer layer was investigated. As for the previous cases SEM images were acquired, and EDS data was acquired for the uncoated and coated samples. Figure 5.33 shows the SEM images for the sample as coated and after being in contact with the citric acid solution. The left-handed image shows a smooth surface for the AISI D2 coated with a platinum buffer layer and a

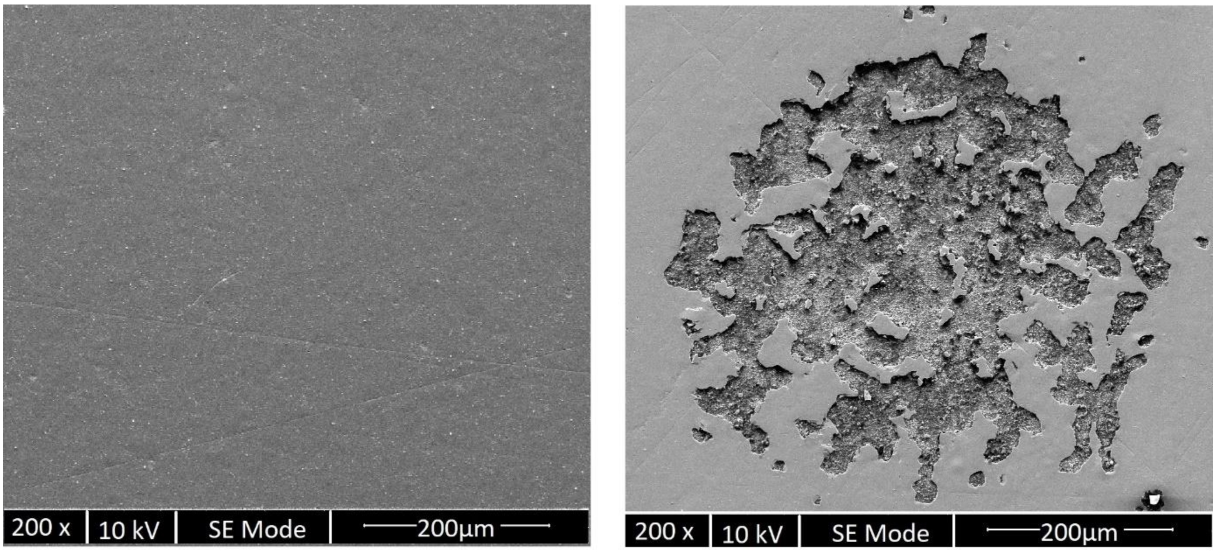

Figure 5.33 SEM image for AISI D2 coated with a platinum buffer layer and tungsten nitride (left)as coated an (right) after exposed to 10^{-4} citric acid aqueous solution.

tungsten nitride film. The EDS analysis gave an average composition of W 84%, O 12%, N 3%, and Ar 1%.

After exposition to the citric acid solution the surface was considerable damaged as shown in the right-handed image of Figure 5.31. The Figure 5.34 shows the EDS maps of the damaged region, as before each image is the distribution of each detected element. The detected elements and their average percentages were W 45%, Fe 24%, 11 O%, C 10%, Cr 6%, N 3%, and Pt 2%.

The EDS maps for W, Fe, Pt, C and Cr demonstrate that the acid treatment removed the tungsten nitride film and the buffer layer.

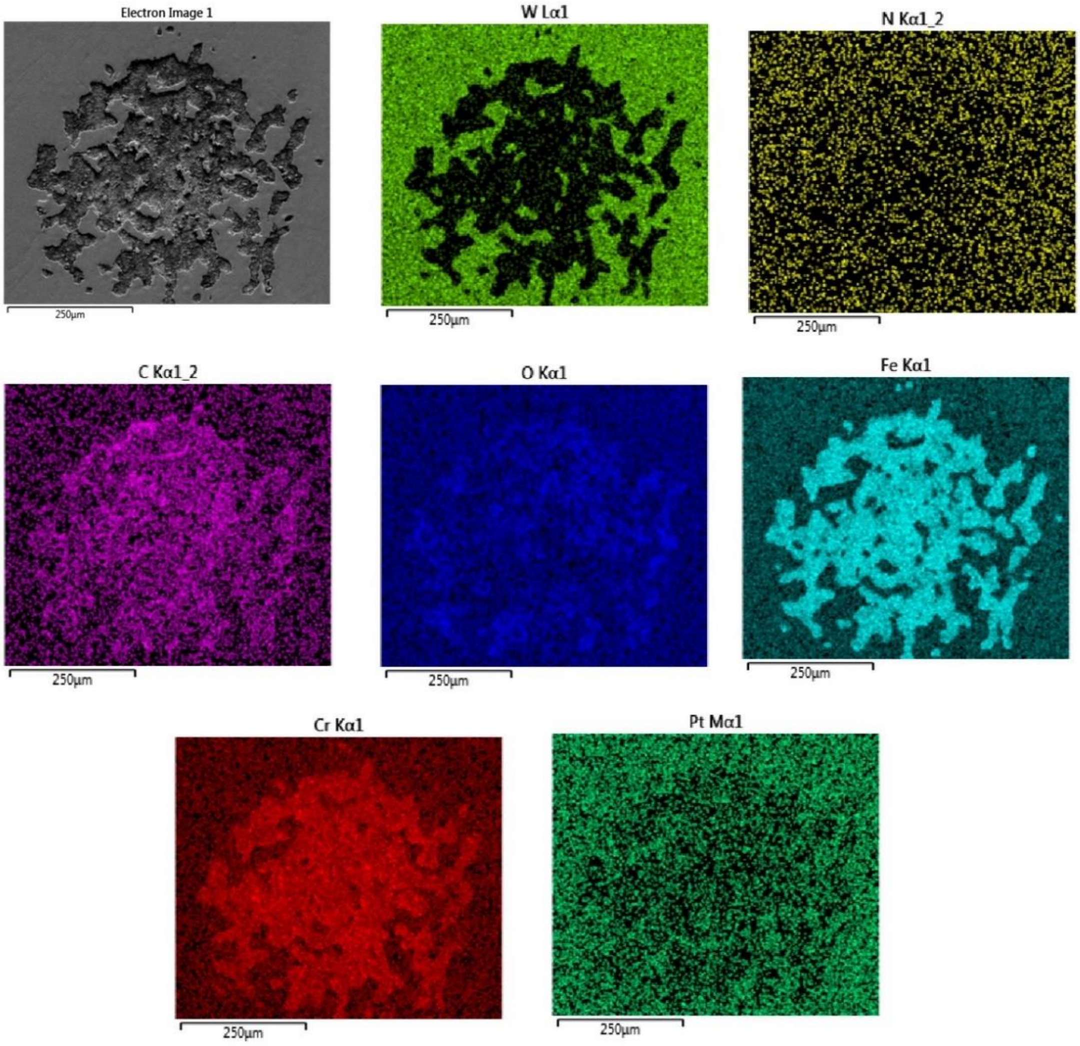

Figure 5.34 Mapping EDS for AISI D2 steel coated with a platinum buffer layer and tungsten nitride at 150 W and 0.5 Pa after contact with 10^{-4} citric acid aqueous solution.

Carbon buffer layer

Finally, AISI D2 substrates were coated with a buffer carbon layer by rf magnetron sputtering using pure argon at 0.5 Pa and 250W using the Plasyss system, immediately followed by the sputtering of the tungsten nitride film at the same condition of the previous samples. In between deposits (buffer and tungsten nitride) the coatings were keep inside the same vacuum chamber. Once both deposits were finished the samples were taken off the vacuum chamber and the coatings delaminates instantly in contact with air. Figure 5.35 shows an example of a coated samples just after the deposition process had finished. As one can see the sample suffered generalized delamination of the tungsten nitride coatings due to the presence of the carbon coating. This helped to corroborate that when the tungsten nitride film is in contact with high carbon concentrations the thin film delaminates.

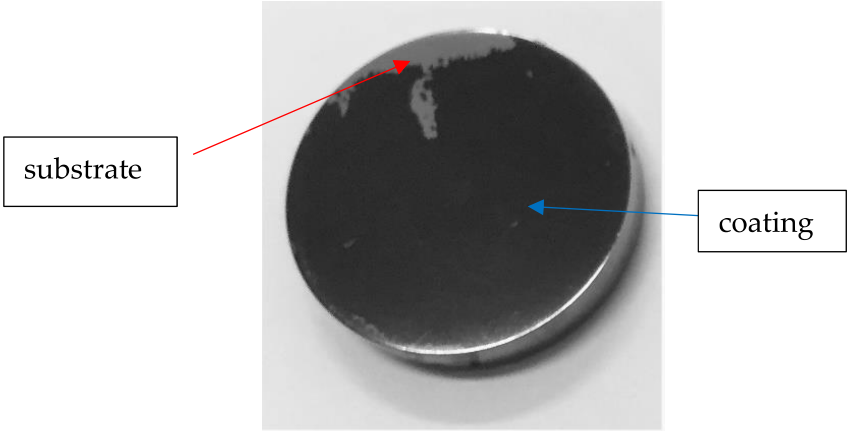

Figure 5.35 AISI D2 steel coated with a buffer layer of carbon and tungsten nitride at 150W and 0.5 Pa.

5.2.7 Tribocorrosion evaluation

5.2.7.1 Continuous sliding

The measurements were carried out on samples coated with tungsten nitride deposited by rf magnetron sputtering at 0.5 Pa and 150 W were under continuous sliding test conditions at 1.5N of load and 0.02 m/s, in contact with 10^{-4} M citric acid aqueous solution.

For the thin films sputtered over AISI D2 the influence of the electrolyte pin on disc test was evaluated, however, the tribocorrosion synergy could not be evaluated because of the dominant localized corrosion regions. Hence, to evaluate the influence of the electrolyte in the wear of the AISI D2 steel coated with tungsten nitride, pin on disc tests were performed. Figure 5.36 shows an example of a wear track profile. Here is not evident to identify the wear track region due to severe damage over the samples.

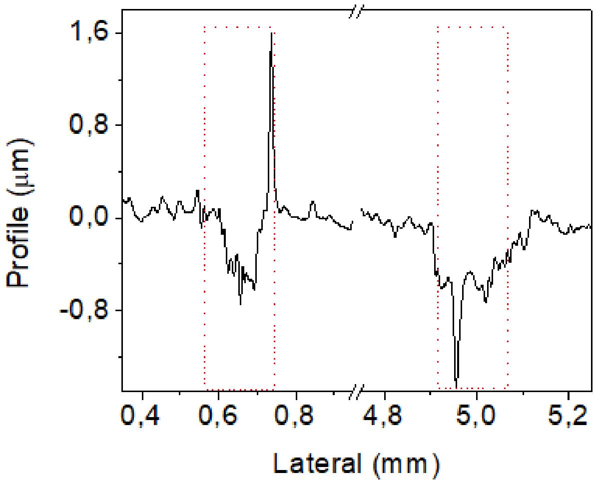

Figure 5.36 Profile of the wear track region after AISI D2 steel coated with tungsten nitride after a pin on disc at 1.5 N test in contact with citric acid 10^{-4} M.

The estimated material loss was 2.2x10^{-3} mm^3, a value two magnitude's order larger than for the dry test (1.9$10^{-5}$ mm^3) and one magnitude's order larger than for the uncoated steel (4.91x10^{-4} mm^3). Such large increment is probably due a galvanic effect between the thin film and the steel[Diomidis et al. 2009; López-Ortega, Arana, and Bayón 2018]. The galvanic effect occurs when two conductive materials (in general metals) are in contact with an electrolyte and one of the materials corrodes preferentially[Bagotsky 2006]. In this case, when the thin film presents delamination and fractures due the mechanical wear and corrosion points, caused by the incompatibility of the thin film with the rich in carbon regions the AISI D2 steel. Then the areas where the coating has failed will be exposed to accelerated corrosion.

As for the AISI 431 coated samples, the combined electrochemical measurements and pin on disc tests were performed. The OCP was measured before and during the pin on disc test. Figure 5.37 shows the temporal evolution of the COF. Such a curve presents significant changes during the first minutes of the test which corresponded to the breaking in of the passivation layer before a steady state was established. The average COF during the steady state was 0.04 ±0.01, a significantly smaller value than that found for the pin on disc test without electrolyte (0.28 ± 0.07). This reduction in the COF can be attributed to the aqueous solution acting as a lubricant and the formation of a good passive layer.

Furthermore, the resulting Nyquist diagram for the test under continuous sliding is presented in Figure 5.38, such a diagram has two semi circles as for the previously analyzed systems. The obtained results were modeled using the equivalent circuit shown in Figure 3.28 composing of two parallel RC circuits connected in series. Here the second resistance (R_2) corresponds to the polarization resistance R_{ps} of the system, which is considered to be the combination of two polarization resistances, R_{act} associated with the area that corrodes and R_{pass} the area that passivates. The estimated of R_{ps} value was 154.1 ±2.2 kΩ. Such value, along with the specific passivation resistance (r_{pass}) obtained from the static EIS tests, was employed to estimate the specific corrosion resistance of the active region or wear track (r_{act}). The r_{act} was calculated as described in Chapter 3. The estimated r_{act} value was 9.3 kΩcm² which corresponds to a corrosion current of about 2.6×10^{-6} A/cm².

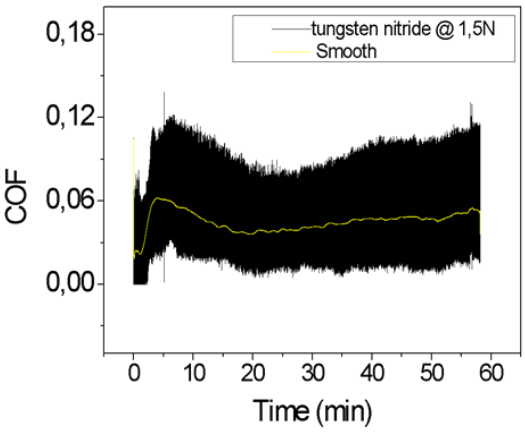

Figure 5.37 Temporal evolution of the COF for the system AISI 431 steel coated with tungsten nitride-Al_2O_3 at 1.5N when in contact with the citric acid 10^{-4} M solution.

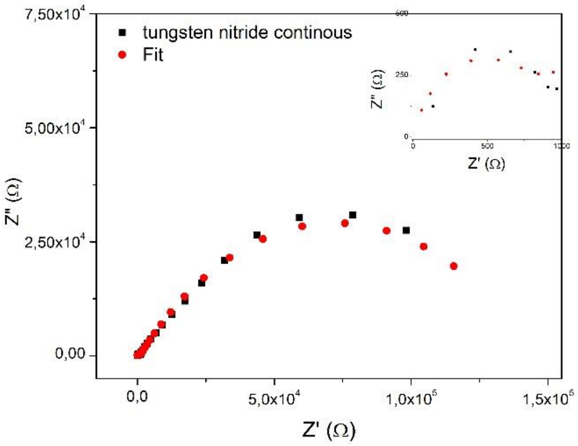

Figure 5.38 Nyquist diagram for of AISI431 steel coated with tungsten nitride in contact with the citric acid 10^{-4} M solution while in continuous sliding at 1.5 N.

Furthermore, profilometry mapping was performed over the sample surface after the coupled test. Figure 5.39 presents an example of a wear track profile; the wear track region is highlighted with the red rectangles to assist on the wear tack detection.

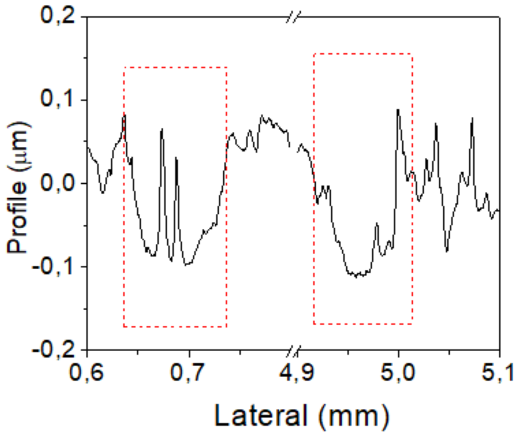

Figure 5.39 Profile of the wear track region for AISI 431 steel coated with tungsten nitride in contact with the citric acid 10^{-4} M solution while in continuous sliding at 1.5 N.

The estimated wear loss was $5.1\times10^{-4} \pm 4.0\times10^{-7}$ mm³ one order of magnitude larger than the one found for substrate without coating ($1.8\times10^{-3} \pm 4.0\times10^{-7}$ mm³). Hence, the thin film increased the tribocorrosion resistance.

5.2.7.2 *Latency tests*

During the latency tests, pin on disc test were performed with the sample in contact with the electrolyte. For such tests, successive identical cycles of rotation(1s)-latency (20s) were repeated until a total sliding distance of 72 m was reached.

The resulting wear track was measured by contact profilometry as for the previous experiments. Figure 5.40 shows a wear track profile. Such results were used to calculate the total volume loss in the wear track giving a value of $7\times10^{-4} \pm 4.0\times10^{-7}$ mm³.

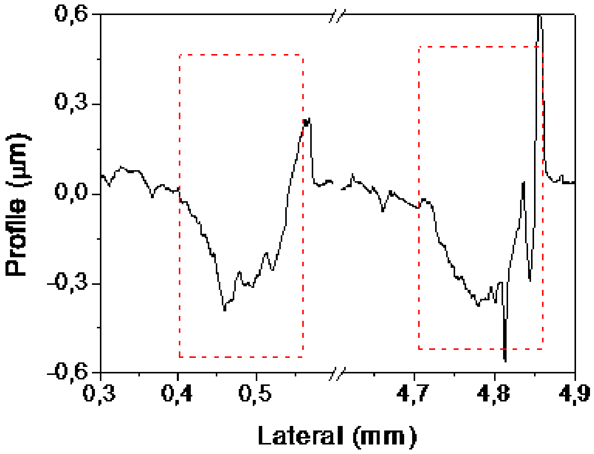

Figure 5.40 Profile of the wear track region for AISI 431 coated with tungsten nitride in contact with the citric acid 10^{-4} M solution while in latency sliding at 1.5 N.

The volume loss value measured after the latency tests along with the EIS the coated sample were used to calculate K_c and K_m as described in 1.2.2. The estimated K_c ratio was 5.1×10^{-1}, and as mentioned earlier when Kc <<1 one can consider that corrosion is virtually not affected by the presence of the tribological test. Hence the system was dominated by the mechanical wear of the thin film. Furthermore, the estimated K_m value was 6.1×10^{-3}, and such a value indicates that the mechanical removal was accelerated by the formation of the passive layer of the thin film.

5.3 Chapter's conclusions

In this chapter the results of tribological and electrochemical studies of the tungsten nitride coated steel substrates has been reported. Additionally, an estimation of the tribocorrosion behavior of the coating deposited over AISI 431 was performed.

The coatings proved to diminish the mechanical wear for both substrates with wear rates typically an order of magnitude smaller than that obtained for the uncoated steel samples (AISI D2 2.1x10^{-4} mm^3, AISI 431 1.6x10^{-4} mm^3. Nevertheless, the coatings deposited on AISI D2 presented adhesion problems and such problems resulted in localized corrosion. To overcome this problem the use of different buffer layers was explored. Unfortunately, the proposed buffer layers did not reduce the localized corrosion. In particular, the adherence problems were found to be associated to high carbon concentrations in the substrate in some localized regions of the substrate

The EIS tests revealed an increment in the corrosion resistance for the thin films deposited over AISI D2 steel. Nevertheless, the increment was not enough to achieve passivity.

The thin films deposited over AISI 431 steel increased the corrosion resistance of the sample surface.

Comparing the specific corrosion resistance from the thin films obtained on conductive silicon and AISI 431 steel, it was possible to estimate that the specific resistance corrosion value for the tungsten nitride thin film was about 242 ± 35 kΩcm^2. Hence the tungsten nitride thin film was corrosion resistant on this substrate.

The tribocorrosion of the thin film deposited on AISI 431steel was studied. After the pin on disc test under room temperature and relative humidity, the thin film presented a total material accumulation of 7.1x10^{-6} ±1.8x10^{-7} mm^3 a significantly lower value than the one obtained for the uncoated substrate, 1.6x10^{-4} ±1.0x10^{-4} mm^3. Hence the thin film protected the surface against mechanical wear. Moreover, the specific corrosion of the coated sample (207 ±25 kΩcm^2) was found to be larger than the one for the uncoated AISI 431 steel (160±5 kΩcm^2). Additionally, when exposed to tribocorrosion the volume loss over the wear track was smaller for the coated sample (5.1x10^{-4} for continuous sliding and. 7.0 x10^{-4} mm^3 for latency), than for the uncoated sample with (1.8x10^{-3}mm^3 for continuous sliding and.8x10^{-3} mm^3 for latency). Finally, the estimated K_c and K_m values were 3.6x10^{-1}, 3.0x10^{-3} for AISI 431 steel and 5.1x10^{-1}, 6.1x10^{-3} for the tungsten nitride thin film. Hence the tribocorrosion mechanism was for the uncoated and coated AISI 431 steel samples. This indicated that the acceleration of the corrosion due to the destruction of the passive film was low and that the formation of the passive film accelerates the mechanical removal of the material.

Chapter 6

General conclusion and perspectives

This thesis presents a tribo-electrochemical study (tribocorrosion) of thin tungsten nitride films aimed for protective thin films against tribocorrosion concerning tools used in the food industry. Tribocorrosion is a complex wear phenomenon that occurs when a mechanical action takes place on a metal surface in a corrosive environment. It depends on both; the used tribological system, in terms of the mechanical properties and geometry of the bodies constituting the contact, and on the chemical and electrochemical properties of the medium in which the wear process takes place. Therefore, when studying tribocorrosion, it is crucial to highlight the mechanisms at work and to identify the relevant parameters to better understand tribocorrosion. With this in mind, a methodology has been put in place to determine the various contributions to the total wear by isolating mechanical wear, corrosion, and synergy between both, the substrates, and the tungsten nitride film.

In order to satisfactorily perform the tribo-electrochemical measurements, a custom-made cell was created. This cell had an appropriate geometry for the tribometer used, allowed the proper arrangement of electrodes for electrochemical tests, avoided electrolyte leaks and allowed the adequate isolation of the electrical contact of the sample.

For the substrates it was found that the AISI D2 steel resists the mechanical wear but corrodes when in contact with citric acid. Since it spontaneously corrodes if exposed to simultaneous mechanical wear and corrosion the material loss will be dominated by the material corrosion. As for AISI 431 steel it was found that it exhibits good wear and corrosion resistances when in contact with citric acid. Both steels wear by third body abrasion with aluminum oxide as counter body.

Moreover, when exposed to tribocorrosion it was found that the general damage was significantly larger than when exposed to wear or corrosion independently. Furthermore, the destruction of the passive film does not affect in a significative way the corrosion speed. Nevertheless, the formation of the passive film accelerates the mechanical material removal. Hence, if relative movement between the steel surface and the counter body is slow enough to allow the regrowth of the passive film, the amount of damage due to the tribocorrosion process is larger.

The AISI D2 steel and the AISI 431 were coated with tungsten nitride towards the improvement of the tribological, electrochemical and tribo-electrochemical properties of the material surface. The obtained thin films presented a combination of two crystalline structures, a fcc as the structure found for tungsten nitride and a monoclinic as the one found on tungsten oxide (WO_3).

The tungsten nitride thin films proved to diminish the mechanical wear for both substrates with wear rates one magnitude order smaller than the one obtained for the uncoated steel samples. Nevertheless, the thin films obtained over AISI D2 steel presented localized corrosion. Different deposition conditions were attempted to improve the corrosion resistance. It turned out that denser thin films deposited at low pressures and high powers presented the best corrosion resistance. However, even for the optimized films the surface corrosion was not completely eliminated due to persistent delamination problems in carbon rich regions on AISI D2 steel. Hence, tungsten nitride will protect from corrosion only in certain systems with less carbon content.

When exposed to tribocorrosion, the AISI 431 steel coated with tungsten nitride lose less material than the uncoated substrate, indicating that the thin film protects against tribocorrosion. Moreover, it was found that the corrosion speed is not affected by the mechanical removal of the passive film, nevertheless, the formation of such passive film accelerates the mechanical removal of material.

The results found in this thesis provides a new approach on the use of metallic nitrides as tribocorrosion resistant materials, leaving the door open to study the influence of the pH in the corrosion and tribocorrosion process towards the use of the thin film in different applications. As for a tungsten nitride as a protective film in construction material for the food industry, the present work gives a first approach highlighting the resistance against tribocorrosion at room temperature, nevertheless, additional studies at higher temperatures (up to 60°C) should be carried out along with toxicity panels of the resulting products of the tribocorrosion.

Furthermore, the influence of the composition of the tungsten nitride thin films and their corrosion and tribocorrosion resistance should be studied to cross with the extensive literature on their tribological properties. Such type of studies can help to better understand the factors that affects the tribocorrosion of tungsten nitride and its limitations.

References

Abadias, Grégory, Eric Chason, Jozef Keckes, Marco Sebastiani, Gregory B. Thompson, Etienne Barthel, Gary L. Doll, Conal E. Murray, Chris H. Stoessel, and Ludvik Martinu. 2018a. "Review Article: Stress in Thin Films and Coatings: Current Status, Challenges, and Prospects." *Journal of Vacuum Science & Technology A: Vacuum, Surfaces, and Films* 36 (2): 020801. https://doi.org/10.1116/1.5011790.

———. 2018b. "Review Article: Stress in Thin Films and Coatings: Current Status, Challenges, and Prospects." *Journal of Vacuum Science & Technology A: Vacuum, Surfaces, and Films* 36 (2): 020801. https://doi.org/10.1116/1.5011790.

Abdul Rahim, Mohd Aidil Shah Bin, Mohamad Bin Minhat, Nur Izan Syahriah Binti Hussein, and Mohd Shukor Bin Salleh. 2018. "A Comprehensive Review on Cold Work of AISI D2 Tool Steel." *Metallurgical Research and Technology* 115 (1): 1–12. https://doi.org/10.1051/metal/2017048.

Addonizio, M L, A Castaldo, A Antonaia, E Gambale, and L Iemmo. 2012. "Influence of Process Parameters on Properties of Reactively Sputtered Tungsten Nitride Thin Films." *Journal of Vacuum Science & Technology A* 30 (2012): 031506. https://doi.org/10.1116/1.3698399.

Aguilera, José Miguel, and Peter Lillford. 2008. *Food Materials Science*. *Food Materials Science: Principles and Practice*. Springer, Boston, MA. https://doi.org/10.1007/978-0-387-71947-4.

Aliofkhazraei, Mahmood. 2011. *Nanocoatings*. Vol. 91. Berlin Heidelberg New York: Springer. https://doi.org/10.1007/978-3-642-17966-2.

Amemiya, Shigeru, Melisa D. Arning, John E. Baur, Adam J. Bergren, Shaowei Chen, Madalina Ciobanu, David E. Cliffel, et al. 2007. "Corresponding Authors." In *Handbook of Electrochemistry*, xix–xx. Las Cruces: Elsevier. https://doi.org/10.1016/B978-044451958-0.50001-X.

Arunkumar, S. 2018. "A Review of Indentation Theory." *Materials Today: Proceedings* 5 (11): 23664–73. https://doi.org/10.1016/j.matpr.2018.10.156.

ASTM. 2015. "C1624 - 05(2015), Standard Test Method for Adhesion Strength and Mechanical Failure Modes of Ceramic Coatings by Quantitative Single Point Scratch Testing." West Conshohocken, PA: ASTM International. https://doi.org/10.1520/C1624-05R15.

ASTM G119-93. 1998. "Standard Guide for Determining Synergism between Wear and Corrosion." *ASTM Handbook*, 529–34.

Bagotsky, V. S. 2006. *Fundamentals of Electrochemestry. Fundamentals of Electrochemistry*. Hoboken, New Jersey: JOHN WILEY & SONS, INC. http://link.springer.com/10.1385/1-59259-877-3:003.

Bailey, D M, and R S Sayles. 1991. "Effect of Roughness and Sliding Friction on Contact Stresses." *Journal of Tribology* 113 (4): 729–38. https://doi.org/10.1115/1.2920686.

Baker, Colin C, and S Ismat Shah. 2002. "Reactive Sputter Deposition of Tungsten Nitride Thin Films." *Journal of Vacuum Science & Technology A* 20 (5): 1699–1703. https://doi.org/doi:http://dx.doi.org/10.1116/1.1498278.

Baptista, Andresa, Francisco Silva, Jacobo Porteiro, José Míguez, and Gustavo Pinto. 2018. "Sputtering Physical Vapour Deposition (PVD) Coatings: A Critical Review on Process Improvement and Market Trend Demands." *Coatings* 8 (11): 402. https://doi.org/10.3390/coatings8110402.

Beitz, W., and K.-H. Kuttner. 1994. *Handbook of Mechanical Engineering*. Springer - Verlag. https://doi.org/10.1007/978-1-4471-3566-1.

Berthout, Guillaume, Nicholas X Randall, and Nicholas X Randall. 2017. "Tests de Rayure." *Techniques de l'ingénieur* 33 (0).

Bourithis, L., G. D. Papadimitriou, and J. Sideris. 2006. "Comparison of Wear Properties of Tool Steels AISI D2 and O1 with the Same Hardness." *Tribology International* 39 (6): 479–89. https://doi.org/10.1016/j.triboint.2005.03.005.

Brett, Christopher M A, and Crina-Maria Nimigean. 1997. "Corrosion of Sputtered W–Ni–N Hard Coatings in Chloride Media." *Thin Solid Films* 311 (1): 1–6. https://doi.org/https://doi.org/10.1016/S0040-6090(97)00294-0.

Broitman, Esteban. 2017. "Indentation Hardness Measurements at Macro-, Micro-, and Nanoscale: A Critical Overview." *Tribology Letters* 65 (1): 1–18. https://doi.org/10.1007/s11249-016-0805-5.

Bruker. 2011. "DektakXT User Manual." Bruker Corporation.

Cao, Shoufan, and Stefano Mischler. 2018a. "Current Opinion in Solid State & Materials Science Modeling Tribocorrosion of Passive Metals – A Review." *Current Opinion in Solid State & Materials Science* 22 (4): 127–41. https://doi.org/10.1016/j.cossms.2018.06.001.

———. 2018b. "Modeling Tribocorrosion of Passive Metals – A Review." *Current Opinion in Solid State and Materials Science* 22 (4): 127–41. https://doi.org/10.1016/j.cossms.2018.06.001.

Castillejo, F. E., D. M. Marulanda, J. J. Olaya, and J. E. Alfonso. 2014. "Wear and Corrosion Resistance of Niobium-Chromium Carbide Coatings on AISI D2 Produced through TRD." *Surface and Coatings Technology* 254: 104–11. https://doi.org/10.1016/j.surfcoat.2014.05.069.

Celis, J-P, and P. Ponthiaux, eds. 2012. *Testing Tribocorrosion of Passivating Materials*

Supporting Research and Industrial Innovation : Handbook. 1st ed. European Federation Of Corrosion.

Chen, B. F., W. L. Pan, G. P. Yu, J. Hwang, and J. H. Huang. 1999. "On the Corrosion Behavior of TiN-Coated AISI D2 Steel." *Surface and Coatings Technology* 111 (1): 16–21. https://doi.org/10.1016/S0257-8972(98)00710-5.

Ching, Hee Ay, Dipankar Choudhury, Md Julker Nine, and Noor Azuan Abu Osman. 2014. "Effects of Surface Coating on Reducing Friction and Wear of Orthopaedic Implants." *Science and Technology of Advanced Materials* 15 (1): 014402. https://doi.org/10.1088/1468-6996/15/1/014402.

Cho, Kyun Taek, Young Kook Lee, and Won Beom Lee. 2015. "Wear Behavior of AISI D2 Steel by Enhanced Ion Nitriding with Atomic Attrition." *Tribology International* 87: 82–90. https://doi.org/10.1016/j.triboint.2015.02.020.

Clyne, T.W. 2001. "Residual Stresses in Coated and Layered Systems." *Encyclopedia of Materials: Science and Technology*, 8126–34. https://doi.org/10.1016/b0-08-043152-6/01458-3.

Cruz Garcia, Carlos de la, Gloria Sánchez Moragas, and David Nordqvist. 2014. "Food Contact Materials." *Food Safety Management*, 397–419. https://doi.org/10.1016/B978-0-12-381504-0.00016-0.

Depla, D, S Mahieu, and Je Greene. 1991. "Sputter Deposition Processes." In *Handbook of Deposition Technologies for Films and Coatings*, 281:253–96. http://books.google.com/books?hl=en&lr=&id=owMVeiPmQaAC&oi=fnd&pg=PA177&dq=Sputter+deposition+processes&ots=L4r5OnYaVv&sig=yN2iwxGU5Y11BArgoAH14zMydUw.

Díaz-Guillén, J. C., J. A. Díaz-Guillén, E. E. Granda-Gutiérrez, M. R. Díaz-Guillén, and M. A. González-Albarrán. 2013. "Electrochemical Corrosion Performance of AISI D2 Tool Steel Surface Hardened by Pulsed Plasma Nitriding." *International Journal of Electrochemical Science* 8 (1): 973–82.

Diomidis, N., J. P. Celis, P. Ponthiaux, and F. Wenger. 2010. "Tribocorrosion of Stainless Steel in Sulfuric Acid: Identification of Corrosion-Wear Components and Effect of Contact Area." *Wear* 269 (1–2): 93–103. https://doi.org/10.1016/j.wear.2010.03.010.

Diomidis, N, J. P. Celis, P Ponthiaux, and F Wenger. 2009. "A Methodology for the Assessment of the Tribocorrosion of Passivating Metallic Materials." *Lubrication Science* 21 (2): 53–67. https://doi.org/10.1002/ls.73.

Edgar Alfonso, Jairo Olaya, and Gloria Cubillos. 2012. "Thin Film Growth Through Sputtering Technique and Its Applications." In *Crystallization - Science and Technology*, edited by Marcello Rubens Barsi Andreeta, 397–432. https://doi.org/DOI: 10.5772/2395.

Edwards, D. D., J. H. Hwang, S. J. Ford, and T. O. Mason. 1997. "Experimental

Limitations in Impedance Spectroscopy: Part V. Apparatus Contributions and Corrections." *Solid State Ionics* 99 (1–2): 85–93. https://doi.org/10.1016/s0167-2738(97)00206-3.

Ekaterina Karamfilova. 2016. "Food Contact Materials - Regulation (EC) 1935/2004." European Parliament. http://www.europarl.europa.eu/RegData/etudes/STUD/2016/581411/EPRS_STU(2016)581411_EN.pdf.

Fathollahzade, N., and K. Raeissi. 2014. "Electrochemical Evaluation of Corrosion and Tribocorrosion Behaviour of Amorphous and Nanocrystalline Cobalt-Tungsten Electrodeposited Coatings." *Materials Chemistry and Physics* 148 (1–2): 67–76. https://doi.org/10.1016/j.matchemphys.2014.07.013.

FDA/Center for Food Safety & Applied Nutrition. 2008. "Approximate PH of Foods and Food Products." http://www.foodscience.caes.uga.edu/extension/documents/fdaapproximatephoffoodslacf-phs.pdf.

Featherstone, Susan, and Susan Featherstone. 2015. "Canning Operations." *A Complete Course in Canning and Related Processes*, January, 187–202. https://doi.org/10.1016/b978-0-85709-677-7.00010-4.

Fenker, M., M. Balzer, and H. Kappl. 2006. "Corrosion Behaviour of Decorative and Wear Resistant Coatings on Steel Deposited by Reactive Magnetron Sputtering - Tests and Improvements." *Thin Solid Films* 515 (1): 27–32. https://doi.org/10.1016/j.tsf.2005.12.020.

Fernandez-Solis, Christian D, Ashokanand Vimalanandan, Abdulrahman Altin, Jesus S Mondragon-Ochoa, Katharina Kreth, Patrick Keil, and Andreas Erbe. 2016. "Fundamentals of Electrochemistry, Corrosion and Corrosion Protection." In . Vol. 917. https://doi.org/10.1007/978-3-319-24502-7.

Findik, Fehim. 2014. "Latest Progress on Tribological Properties of Industrial Materials." *Materials and Design* 57: 218–44. https://doi.org/10.1016/j.matdes.2013.12.028.

Gauvent, M., E. Rocca, P. J. Meausoone, and P. Brenot. 2006. "Corrosion of Materials Used as Cutting Tools of Wood." *Wear* 261 (9): 1051–55. https://doi.org/10.1016/j.wear.2006.03.036.

Godet, M., Y. Berthier, L. Vincent, and L. Flamand. 1991. "Hard Coatings for Tribological Applications: A Pluridisciplinary Approach." *Surface and Coatings Technology* 45 (1–3): 1–8. https://doi.org/10.1016/0257-8972(91)90199-7.

Gonohe, N. 2002. "Tungsten Nitride Deposition by Thermal Chemical Vapor Deposition as Barrier Metal for Cu Interconnection." *Materials Transactions* 43 (7): 1585–92. https://doi.org/DOI 10.2320/matertrans.43.1585.

Gracia-Escosa, E., I. García, J. C. Sánchez-López, M. D. Abad, A. Mariscal, M. A.

Arenas, J. de Damborenea, and A. Conde. 2015. "Tribocorrosion Behavior of TiBxCy/a-C Nanocomposite Coating in Strong Oxidant Disinfectant Solutions." *Surface and Coatings Technology* 263: 78–85. https://doi.org/10.1016/j.surfcoat.2014.12.047.

Grand View Research. 2018. "U . S . Canned Foods Market Size , Share & Trends Analysis Report , By Type (Seafood , Vegetables , Meat Products , Fruits , Ready Meals), Competitive Landscape , And Segment Forecasts , 2018 - 2025." https://www.grandviewresearch.com/industry-analysis/us-canned-foods-market.

Güttler, D., B. Abendroth, R. Grötzschel, W. Möller, and D. Depla. 2004. "Mechanisms of Target Poisoning during Magnetron Sputtering as Investigated by Real-Time in Situ Analysis and Collisional Computer Simulation." *Applied Physics Letters* 85 (25): 6134–36. https://doi.org/10.1063/1.1835002.

Hamidzadeh, M. A., M. Meratian, and M. Mohammadi Zahrani. 2012. "A Study on the Microstructure and Mechanical Properties of AISI D2 Tool Steel Modified by Niobium." *Materials Science and Engineering A* 556: 758–66. https://doi.org/10.1016/j.msea.2012.07.061.

Han, Jeon G. n.d. "Magnetron Sputtering Technology." *Surface Technology*.

Han, Xuesong. 2014. "An Investigation into the Tribological Property of Coatings on Micro- and Nanoscale." *Anti-Abrasive Nanocoatings: Current and Future Applications*, 24–55. https://doi.org/10.1016/B978-0-85709-211-3.00002-9.

Heilmann, P., and D. S. Rigney. 1982. *Running-in Processes Affecting Friction and Wear. THE RUNNING-IN PROCESS IN TRIBOLOGY: Proceeding of the 8th Leeds–Lyon Symposium on Tribology, Held in the Institue National Des Science Appliquées de Lyon, France, 8–11 September 1981*. Butterworth & Co (Publishers) Ltd. https://doi.org/10.1016/B978-0-408-01226-3.50009-3.

Heldman, Dennis R. 2013. *Food Science*. Edited by springer. *Food Science Texts Series Series*. https://doi.org/10.1007/978-1-4615-4985-7.

Henry, P., M. J. Pac, C. Rousselot, and M. H. Tuilier. 2013. "Wear Mechanisms of Titanium and Aluminium Nitride Coatings: A Microtribological Approach." *Surface and Coatings Technology* 223: 79–86. https://doi.org/10.1016/j.surfcoat.2013.02.033.

Henry, P., J. Takadoum, and P. Berçot. 2011. "Depassivation of Some Metals by Sliding Friction." *Corrosion Science* 53 (1): 320–28. https://doi.org/10.1016/j.corsci.2010.09.038.

Hones, P., R. Consiglio, N. Randall, and F. Leacutevy. 2000. "Mechanical Properties of Hard Chromium Tungsten Nitride Coatings." *Surface and Coatings Technology* 125 (1–3): 179–84. https://doi.org/10.1016/S0257-8972(99)00541-1.

Hones, Peter, Nicolas Martin, Manfred Regula, and Francis L vy. 2003. "Structural and

Mechanical Properties of Chromium Nitride, Molybdenum Nitride, and Tungsten Nitride Thin Films.” *Journal of Physics D: Applied Physics* 36 (8): 1023–29. https://doi.org/10.1088/0022-3727/36/8/313.

Hsieh, G., T. O. Mason, E. J. Garboczi, and L. R. Pederson. 1997. “Experimental Limitations in Impedance Spectroscopy: Part III. Effect of Reference Electrode Geometry/Position.” *Solid State Ionics* 96 (3–4): 153–72. https://doi.org/10.1016/s0167-2738(97)00073-8.

IFIC, International Food Information Council Foundation, and Food and Drug Administration US FDA. 2010. “Food Ingredients & Colors.” *U.S Food and Drug Administration*. http://www.fda.gov/downloads/Food/IngredientsPackagingLabeling/ucm094249.pdf.

Igual Muoz, A., and N. Espallargas. 2011. “Tribocorrosion Mechanisms in Sliding Contacts.” In *Tribocorrosion of Passive Metals and Coatings*, 5:118–52. https://doi.org/10.1016/B978-1-84569-966-6.50005-1.

Imeta Srl. 2018. “Chucks and Rolls Catalogue.” 2018. http://www.imetasrl.com/modules/Download/files/dwn-chucks_and_rolls_in_english_and_spanish-1466756369.pdf.

Inkson, B J. 2016. “Scanning Electron Microscopy (SEM) and Transmission Electron Microscopy (TEM) for Materials Characterization.” In *Materials Characterization Using Nondestructive Evaluation (NDE) Methods*, 17–43. Elsevier Ltd. https://doi.org/10.1016/B978-0-08-100040-3.00002-X.

Ionescu, Claudiu Constantin, Claudiu Constantin, and Ionescu Caract. 2013. “Erisation Des m ´ Ecanismes d ′ Usure Par Tribocorrosion d ′ Alliages Mod ` To Cite This Version : Caractérisation Des Mécanismes d ′ Usure Par Tribocorrosion d ′ Alliages Modèles Ni - Cr.”

ISO, E N. 1997. “4287–Geometrical Product Specifications (GPS)–Surface Texture: Profile Method–Terms, Definitions and Surface Texture Parameters.” *International Organization for Standardization: Geneva, Switzerland*.

Jiang, Jiaren, and M M Stack. 2006. “Modelling Sliding Wear: From Dry to Wet Environments.” *Wear* 261: 954–65. https://doi.org/10.1016/j.wear.2006.03.028.

Jiménez, A.-E., and M.-D. Bermúdez. 2011. “2 - Friction and Wear.” In , edited by J Paulo B T - Tribology for Engineers Davim, 33–63. Woodhead Publishing. https://doi.org/https://doi.org/10.1533/9780857091444.33.

Karakaş, Mustafa Serdar. 2020. “Tribocorrosion Behavior of Surface-Modified AISI D2 Steel.” *Surface and Coatings Technology* 394: 125884. https://doi.org/10.1016/j.surfcoat.2020.125884.

Kelly, P.J J, and R.D D Arnell. 2000. “Magnetron Sputtering: A Review of Recent Developments and Applications.” *Vacuum* 56 (3): 159–72.

https://doi.org/10.1016/S0042-207X(99)00189-X.

Kempf, M., M. Göken, and H. Vehoff. 1998. "Nanohardness Measurements for Studying Local Mechanical Properties of Metals." *Applied Physics A: Materials Science and Processing* 66 (SUPPL. 1): 843–46. https://doi.org/10.1007/s003390051253.

Kenneth, G. 2007. "Guide to Friction , Wear , and Erosion Testing." West Conshohocken, PA: ASTM International. https://doi.org/doi.org/10.1520/MNL56-EB.

Kral, C., W. Lengauer, D. Rafaja, and P. Ettmayer. 1998. "Critical Review on the Elastic Properties of Transition Metal Carbides, Nitrides and Carbonitrides." *Journal of Alloys and Compounds* 265 (1–2): 215–33. https://doi.org/10.1016/S0925-8388(97)00297-1.

Landolt, D., S. Mischler, and M Stemp. 2001. "Electrochemical Methods in Tribocorrosion: A Critical Appraisal D." *Electrochimica Acta* 46 (7): 3913–29. ww.

Landolt, Dieter, and Stefano Mischler. 2011. *Tribocorrosion of Passive Metals and Coatings*. *Tribocorrosion of Passive Metals and Coatings*. https://doi.org/10.1533/9780857093738.

Lesage, J., A. Pertuz, E.S. Puchi-Cabrera, and D. Chicot. 2006. "A Model to Determine the Surface Hardness of Thin Films from Standard Micro-Indentation Tests." *Thin Solid Films* 497 (1–2): 232–38. https://doi.org/10.1016/j.tsf.2005.09.194.

Lesyk, D. A., S. Martinez, B. N. Mordyuk, V. V. Dzhemelinskyi, Lamikiz, G. I. Prokopenko, Yu V. Milman, and K. E. Grinkevych. 2017. "Microstructure Related Enhancement in Wear Resistance of Tool Steel AISI D2 by Applying Laser Heat Treatment Followed by Ultrasonic Impact Treatment." *Surface and Coatings Technology* 328: 344–54. https://doi.org/10.1016/j.surfcoat.2017.08.045.

Levy, Karl, Junghwan Sung, Kaihan Ashtiani, Joshua Collins, and Juwen Gao. 2006. DEPOSITION OF TUNGSTEN NITRIDE. US 7,005,372 B2, issued 2006.

Levy, Karl, Junghwan Sung, Kaihan Ashtiani, Joshua Collins, Juwen Gao, Electrochemical Measurements, Polarization Measurements, et al. 2016. "ASTM G119-09: Guide for Determining Synergism Between Wear and Corrosion." *Annual Book of ASTM Standards* 05 (Reapproved 2016): 1–6. https://doi.org/10.1520/G0099-17.Copyright.

Long, Qian, Linqing Wang, Weijie Yu, Weijiu Huang, and Li Wang. 2021. "Structural and Mechanical Properties of Amorphous Si–C-Based Thin Films Deposited by Pulsed Magnetron Sputtering under Different Sputtering Powers." *Vacuum* 191 (May): 110319. https://doi.org/10.1016/j.vacuum.2021.110319.

López-Ortega, A., J. L. Arana, and R. Bayón. 2018. "Tribocorrosion of Passive Materials: A Review on Test Procedures and Standards." *International Journal of Corrosion* 2018. https://doi.org/10.1155/2018/7345346.

Louro, C., and A. Cavaleiro. 1999. "Hardness versus Structure in W-Si-N Sputtered Coatings." *Surface and Coatings Technology* 116–119: 74–80. https://doi.org/10.1016/S0257-8972(99)00277-7.

Mathew, M. T., P. Srinivasa Pai, R. Pourzal, A. Fischer, and M. A. Wimmer. 2009a. "Significance of Tribocorrosion in Biomedical Applications: Overview and Current Status." *Advances in Tribology*, no. December. https://doi.org/10.1155/2009/250986.

———. 2009b. "Significance of Tribocorrosion in Biomedical Applications: Overview and Current Status." *Advances in Tribology* 2009. https://doi.org/10.1155/2009/250986.

Mathew, M T, T Uth, N J Hallab, R Pourzal, A Fischer, and M A Wimmer. 2011. "Construction of a Tribocorrosion Test Apparatus for the Hip Joint: Validation, Test Methodology and Analysis." *Wear* 271 (9): 2651–59. https://doi.org/https://doi.org/10.1016/j.wear.2011.01.085.

Menezes, Pradeep L., Michael Nosonovsky, Sudeep P. Ingole, Michael Lovell, and Satish V. Kailas Michael. 2013. *Tribology for Scientists and Engineers From Basics to Advanced Concepts*. Edited by Pradeep L. Menezes, Sudeep P. Ingole, Michael Nosonovsky, Satish V. Kailas, and Michael R. Lovell. New York: Springer. https://doi.org/10.1007/978-1-4614-1945-7.

Mischler, S. 2008. "Triboelectrochemical Techniques and Interpretation Methods in Tribocorrosion: A Comparative Evaluation." *Tribology International* 41 (7): 573–83. https://doi.org/10.1016/j.triboint.2007.11.003.

Moerman, Frank, and Eric Partington. 2014. "Materials of Construction for Food Processing Equipment and Services : Requirements , Strengths and Weaknesses." *Journal of Hygenic Engineering and Design*, 10–37.

Montemor, M. F., and M. G.S. Ferreira. 2007. "Electrochemical Study of Modified Bis-[Triethoxysilylpropyl] Tetrasulfide Silane Films Applied on the AZ31 Mg Alloy." *Electrochimica Acta* 52 (27 SPEC. ISS.): 7486–95. https://doi.org/10.1016/j.electacta.2006.12.086.

Moore, C.A. 2017. *Automation in the Food Industry*. *Automation in the Food Industry*. C.A. MOORE. Vol. 91. New York: avi.

Mubarak, A, E Hamzah, and M R M Toff. 2005. "Review of Physical Vapour Deposition (PVD) Techniques for Hard Coating." *Jurnal Mekanikal* 20 (20): 42–51.

Murry, Guy. 2020. "Désignation Normalisée Des Aciers Désignation Normalisée Des Aciers" 33 (0).

Musil, J., P. Novák, M. Hromádka, R. Čerstvý, Z. Soukup, and J. Savková. 2013. "Mechanical and Tribological Properties of Sputtered Mo-O-N Coatings." *Surface and Coatings Technology* 215: 386–92. https://doi.org/10.1016/j.surfcoat.2012.06.090.

Nakajima, Hitoshi, Tetsuichi Kudo, and Noritaka Mizuno. 1999. “Reaction of Metal, Carbide, and Nitride of Tungsten with Hydrogen Peroxide Characterized by 183 W Nuclear Magnetic Resonance and Raman Spectroscopy.” *Chemistry of Materials* 11 (3): 691–97. https://doi.org/10.1021/cm980544o.

Ningshen, S, U Kamachi Mudali, G Amarendra, P Gopalan, R K Dayal, and H S Khatak. 2006. “Hydrogen Effects on the Passive Film Formation and Pitting Susceptibility of Nitrogen Containing Type 316L Stainless Steels.” *Corrosion Science* 48 (5): 1106–21. https://doi.org/https://doi.org/10.1016/j.corsci.2005.05.003.

Nix, William D. 1989. “Mechanical Properties of Thin Films.” *Metallurgical Transactions A* 20 (11): 2217–45. https://doi.org/10.1007/BF02666659.

Novak, R., and T. Polcar. 2014. “Tribological Analysis of Thin Films by Pin-on-Disc: Evaluation of Friction and Wear Measurement Uncertainty.” *Tribology International* 74: 154–63. https://doi.org/10.1016/j.triboint.2014.02.011.

Obadele, Babatunde Abiodun, Anthony Andrews, Mxolisi Brendon Shongwe, and Peter Apata Olubambi. 2015. “Tribocorrosion Behaviours of AISI 310 and AISI 316 Austenitic Stainless Steels in 3.5% NaCl Solution.” *Materials Chemistry and Physics* 171: 239–46. https://doi.org/10.1016/j.matchemphys.2016.01.013.

Orazem, MARK E., and Bernard Tribollet. 2008. *Electrochemical Impedance Spectroscopy*. Hoboken, NJ, USA: John Wiley & Sons, Inc. https://doi.org/10.1002/9780470381588.

Parreira, N.M.G., N.J.M. Carvalho, and A. Cavaleiro. 2006. “Synthesis, Structural and Mechanical Characterization of Sputtered Tungsten Oxide Coatings.” *Thin Solid Films* 510 (1–2): 191–96. https://doi.org/10.1016/j.tsf.2005.12.299.

Paxton, Harry. 2004. “Steel.” *Kirk-Othmer Encyclopedia of Chemical Technology*, Major Reference Works, , October. https://doi.org/10.1002/0471238961.1920050516012420.a01.pub2.

Polcar, T., N. M G Parreira, and A. Cavaleiro. 2007a. “Tribological Characterization of Tungsten Nitride Coatings Deposited by Reactive Magnetron Sputtering.” *Wear* 262 (5–6): 655–65. https://doi.org/10.1016/j.wear.2006.07.010.

———. 2008. “Structural and Tribological Characterization of Tungsten Nitride Coatings at Elevated Temperature.” *Wear* 265 (3–4): 319–26. https://doi.org/10.1016/j.wear.2007.10.011.

Polcar, T, N M G Parreira, and A Cavaleiro. 2007b. “Tribological Characterization of Tungsten Nitride Coatings Deposited by Reactive Magnetron Sputtering.” *Wear* 262: 655–65. https://doi.org/10.1016/j.wear.2006.07.010.

Pourbaix, M. 1974. *Atlas of Electrochemical Equilibria in Aqueous Solutions*. National Association of Corrosion Engineers. https://books.google.fr/books?id=QjxRAAAAMAAJ.

Prakash, Ravi, R. Jayaganthan, and Davinder Kaur. 2016. "Structural, Corrosion and Mechanical Properties of Sputtered Deposited Chromium Tungsten Nitride (Cr1-XWxN) Nanocomposite Thin Films." *Advanced Materials Letters* 7 (9): 723–29. https://doi.org/10.5185/amlett.2016.6362.

Puchi-Cabrera, E. S. 2002. "A New Model for the Computation of the Composite Hardness of Coated Systems." *Surface and Coatings Technology* 160 (2–3): 177–86. https://doi.org/10.1016/S0257-8972(02)00394-8.

Puchi-Cabrera, E. S., M. H. Staia, and A. Iost. 2015. "Modeling the Composite Hardness of Multilayer Coated Systems." *Thin Solid Films* 578: 53–62. https://doi.org/10.1016/j.tsf.2015.01.070.

Ramírez, G., A. Mestra, B. Casas, I. Valls, R. Martínez, R. Bueno, A. Góez, A. Mateo, and L. Llanes. 2012. "Influence of Substrate Microstructure on the Contact Fatigue Strength of Coated Cold-Work Tool Steels." *Surface and Coatings Technology* 206 (13): 3069–81. https://doi.org/10.1016/j.surfcoat.2011.12.012.

Ratner, Buddy D. 2007. "Properties of Materials." In *Biomaterials Science: An Introduction to Materials in Medicine*, Third Edit, 34–55. Elsevier. https://doi.org/10.1016/B978-0-08-087780-8.00005-X.

Richard, Caroline, and Jean Geringer. 2019. "Tribocorrosion" 33 (0).

Roberts, EW, and BJ Williams. 1992. "The Effect of Substrate Surface Roughness on the Friction and Wear of Sputtered MoS2 Films." *Journal of Physics D:* 65 (25): A65–70. https://doi.org/10.1088/0022-3727/25/1A/012.

Roussak. n.d. *Applied Chemistry A Textbook for Engineers and Technologists*. Springer. https://doi.org/10.1007/978-1-4614-4262-2.

Ruste, Jacky. 2013. "Microscopie Électronique à Balayage. Principe et Équipement." *Techniques de l'ingénieur Techniques d'analyse Par Imagerie* 33 (0): 21. http://www.techniques-ingenieur.fr/base-documentaire/mesures-analyses-th1/techniques-d-analyse-par-imagerie-42387210/microscopie-electronique-a-balayage-p865/.

Safi, I. 2000. "Recent Aspects Concerning DC Reactive Magnetron Sputtering of Thin Films: A Review." *Surface and Coatings Technology* 127 (2–3): 203–18. https://doi.org/10.1016/s0257-8972(00)00566-1.

Samano, E. C., A. Clemente, J. A. Díaz, and G. Soto. 2010. "Mechanical Properties Optimization of Tungsten Nitride Thin Films Grown by Reactive Sputtering and Laser Ablation." *Vacuum* 85 (1): 69–77. https://doi.org/10.1016/j.vacuum.2010.04.004.

Scharf, T. W., and S. V. Prasad. 2013. "Solid Lubricants: A Review." *Journal of Materials Science* 48 (2): 511–31. https://doi.org/10.1007/s10853-012-7038-2.

Seshan, Krishna, ed. 2002. *Handbook of Thin-Film Deposition Processes and Techniques*.

Handbook of Thin-Film Deposition Processes and Techniques. 2nd ed. Vol. 31. WILLIAM ANDREW. https://doi.org/10.1016/S0026-2692(99)00122-6.

Shan, Yang. 2016. *Canned Citrus Processing Techniques, Equipment, and Food Safety*. Edited by Yang Shan. *Canned Citrus Processing*. Academic Press - Elsevier. https://doi.org/10.1016/B978-0-12-804701-9.00004-6.

Shen, Y. G., Y. W. Mai, Q. C. Zhang, D. R. McKenzie, W. D. McFall, and W. E. McBride. 2000. "Residual Stress, Microstructure, and Structure of Tungsten Thin Films Deposited by Magnetron Sputtering." *Journal of Applied Physics* 87 (1): 177–87. https://doi.org/10.1063/1.371841.

Shen, Y G, and Y W Mai. 2000. "Effect of Oxygen on Residual Stress and Structural Properties of Tungsten Nitride Films Grown by Reactive Magnetron Sputtering." *Materials Science and Engineering: B* 76 (2): 107–15. https://doi.org/10.1016/S0921-5107(00)00424-4.

Sista, V., O. Kahvecioglu, O. L. Eryilmaz, A. Erdemir, and S. Timur. 2011. "Electrochemical Boriding and Characterization of AISI D2 Tool Steel." *Thin Solid Films* 520 (5): 1582–88. https://doi.org/10.1016/j.tsf.2011.07.057.

Sokolowski, Evelyn, Carl Nordling, and Kai Siegbahn. 1958. "Chemical Shift Effect in Inner Electronic Levels of Cu Due to Oxidation." *Physical Review* 110 (3): 776.

Sørensen, P. A., S. Kiil, K. Dam-Johansen, and C. E. Weinell. 2009. "Anticorrosive Coatings: A Review." *Journal of Coatings Technology Research* 6 (2): 135–76. https://doi.org/10.1007/s11998-008-9144-2.

Soto, G., W. De la Cruz, F. F. Castillón, J. A. Díaz, R. Machorro, and M. H. Farías. 2003. "Tungsten Nitride Films Grown via Pulsed Laser Deposition Studied in Situ by Electron Spectroscopies." *Applied Surface Science* 214 (1–4): 58–67. https://doi.org/10.1016/S0169-4332(03)00343-X.

Stansbury, E E, and Robert M Condra. 2000. *Electrochemical Corrosion*.

Stojadinović, J., D. Bouvet, M. Declercq, and S. Mischler. 2009. "Effect of Electrode Potential on the Tribocorrosion of Tungsten." *Tribology International* 42 (4): 575–83. https://doi.org/10.1016/j.triboint.2008.04.009.

Street, Lower Abbey. 2010. *Guidance on Food Additives*.

Sun, Xilian, Zhimin Liu, and Hongtao Cao. 2010. "Effects of Film Density on Electrochromic Tungsten Oxide Thin Films Deposited by Reactive Dc-Pulsed Magnetron Sputtering." *Journal of Alloys and Compounds* 504 (SUPPL. 1): S418–21. https://doi.org/10.1016/j.jallcom.2010.03.155.

Swann, S. 1988. "Magnetron Sputtering." *Physics in Technology* 19 (6): 67–75. https://doi.org/10.1088/0305-4624/19/2/304.

Tang, Linhu, Chengxiu Gao, Jianlong Huang, Hongyan Zhang, and Wenchun Chang. 2013. "Tribology International Dry Sliding Friction and Wear Behaviour of

Hardened AISI D2 Tool Steel with Different Hardness Levels." *Tribiology International* 66 (October): 165–73. https://doi.org/10.1016/j.triboint.2013.05.006.

Taylor, Publisher. 2011. "Canned Food A Review on Acidifying Treatments," no. December 2014: 37–41. https://doi.org/10.1080/10408398.2010.491163.

Tesfamichael, Tuquabo, Masashi Arita, Thor Bostrom, and John Bell. 2010. "Thin Film Deposition and Characterization of Pure and Iron-Doped Electron-Beam Evaporated Tungsten Oxide for Gas Sensors." *Thin Solid Films* 518 (17): 4791–97. https://doi.org/10.1016/j.tsf.2010.01.037.

Thornton, John A., and D. W. Hoffman. 1989a. "Stress-Related Effects in Thin Films." *Thin Solid Films* 171 (1): 5–31. https://doi.org/10.1016/0040-6090(89)90030-8.

Thornton, John A, and D. W. Hoffman. 1989b. "Stress-Related Effects in Thin Films." *Thin Solid Films* 171 (1): 5–31. https://doi.org/10.1016/0040-6090(89)90030-8.

Toboła, Daniel, Witold Brostow, Kazimierz Czechowski, and Piotr Rusek. 2017. "Improvement of Wear Resistance of Some Cold Working Tool Steels." *Wear* 382–383: 29–39. https://doi.org/10.1016/j.wear.2017.03.023.

Uhlenhaut, D. I., J. Kradolfer, W. Püttgen, J. F. Löffler, and P. J. Uggowitzer. 2006. "Structure and Properties of a Hypoeutectic Chromium Steel Processed in the Semi-Solid State." *Acta Materialia* 54 (10): 2727–34. https://doi.org/10.1016/j.actamat.2006.02.021.

Verhoeven, John. 2016. "Steel Metallurgy for the Non-Metallurgist," no. January 2007.

Verhoeven, John D. 2007. "Steel Metallurgy for the Non-Metallurgist." *ASM International*, no. January 2007: 203. https://doi.org/10.1361/smnm2007p001.

Villaseca, L., B. Moreno, I. Lorite, J. R. Jurado, and E. Chinarro. 2015. "Synthesis and Characterization of Tungsten Nitride (W2N) from WO3 and H2WO4 to Be Used in the Electrode of Electrochemical Devices." *Ceramics International* 41 (3): 4282–88. https://doi.org/10.1016/j.ceramint.2014.11.114.

Walter, G W. 1986. "A Review of Impedance Plot Methods Used for Corrosion Performance Analysis of Painted Metals." *Corrosion Science* 26 (9): 681–703. https://doi.org/10.1016/0010-938X(86)90033-8.

Wasa, Kiyotaka. 2012. "Preface." In *Handbook of Sputtering Technology (Second Edition)*, edited by Kiyotaka Wasa, Isaku Kanno, and Hidetoshi Kotera, Second Edi, xi–xii. Oxford: William Andrew Publishing. https://doi.org/https://doi.org/10.1016/B978-1-4377-3483-6.00013-9.

Wen, M., Q. N. Meng, W. X. Yu, W. T. Zheng, S. X. Mao, and M. J. Hua. 2010. "Growth, Stress and Hardness of Reactively Sputtered Tungsten Nitride Thin Films." *Surface and Coatings Technology* 205 (7): 1953–61. https://doi.org/10.1016/j.surfcoat.2010.08.082.

Wood, Robert J K. 2007. "Tribo-Corrosion of Coatings: A Review." *Journal of Physics*

D: Applied Physics 40 (18): 5502–21. https://doi.org/10.1088/0022-3727/40/18/S10.

Wood, Robert J K, Stephen Herd, and Mandar R Thakare. 2018. "Tribology International A Critical Review of the Tribocorrosion of Cemented and Thermal Sprayed Tungsten Carbide." *Tribology International* 119 (June 2017): 491–509. https://doi.org/10.1016/j.triboint.2017.10.006.

Yam, K. L. 2009. *Encyclopedia of Packaging Technology*. *Wiley, A John Wiley & Sons, Inc.* https://doi.org/10.1017/S2042169900004284.

Yasavol, Noushin, and Amilcar Ramalho. 2015. "Wear Properties of Friction Stir Processed AISI D2 Tool Steel." *Tribology International* 91: 177–83. https://doi.org/10.1016/j.triboint.2015.07.001.

Résumé étendu

Le processus de tribocorrosion se manifeste lorsque la dégradation d'une surface se produit en raison de l'interaction de l'usure mécanique et de la corrosion, c'est-à-dire lorsque deux matériaux solides en contact et en mouvement relatif sont exposés à un environnement corrosif. Le présent travail explore l'utilisation d'une couche mince de nitrite de tungstène comme protection contre le processus de tribocorrosion des aciers utilisés pour des outils de production de l'industrie alimentaire.

Le phénomène de tribocorrosion est activement étudié depuis la fin des années 1980 en raison d'une demande croissante dans divers domaines : implants biomédicaux, production d'électricité, d'industries marines et offshore. Cependant, la présence du procédé de tribocorrosion n'est pas limitée à ces applications.

A ce titre, la tribocorrosion dépend d'une grande variété de paramètres liés à l'environnement corrosif et aux matériaux en contact. *Néanmoins, le contact mécanique joue un rôle important dans la détermination de l'effet de la corrosion sur l'usure de la surface.* Pour cela, il existe actuellement deux protocoles reconnus pour la détermination de l'usure par tribocorrosion et de la synergie entre usure mécanique et corrosion. Celui proposé par [ASTM G119-93 1998] basé sur des mesures potentiodynamiques et mécaniques pour l'estimation de l'usure et le protocole proposé par [Celis and Ponthiaux 2012]. L'estimation du taux de corrosion par EIS et la quantité de matière enlevée lors des tests mécaniques dans différentes conditions sont utilisées pour estimer les dommages de tribocorrosion et l'effet de synergie.

Pour le présent travail, la méthodologie utilisée comprend : (1) l'adaptation et l'optimisation du système de synthèse de couche minces (pulvérisation cathodique RF) et du système de mesure de la tribocorrosion, (2) la caractérisation électrochimique et tribologique des substrats (acier AISI 431 et acier AISI D2), (3) et la réalisation, l'optimisation et la caractérisation de couches minces de nitrure de tungstène et de leurs propriétés tribo-électrochimiques (tribocorrosion).

Afin d'effectuer des mesures de tribocorrosion, une cellule faite sur mesure a été conçue. Ladite cellule et le montage expérimental sont présentés sur la Figure i. La cellule a fonctionné comme une couverture pour un support existant auparavant. Le niveau inférieur a été conçu pour contenir un contact électrique glissant composé par un « électrolyte de pont » et un fil conducteur tandis que le niveau supérieur a été utilisé pour l'échantillon et l'électrolyte pour le test électrochimique (solution aqueuse 10^{-4} M d'acide citrique). L'électrolyte de pont utilisé pour le contact électrique coulissant était une solution aqueuse 1,0 M de chlorure de potassium. L'échantillon a été attaché à un fil d'argent, les extrémités du fil ont été immergées dans l'électrolyte. Pour établir le contact électrique entre le contact électrique glissant et le potentiostat, un deuxième fil d'argent a été immergé dans le chlorure de potassium puis connecté au potentiostat.

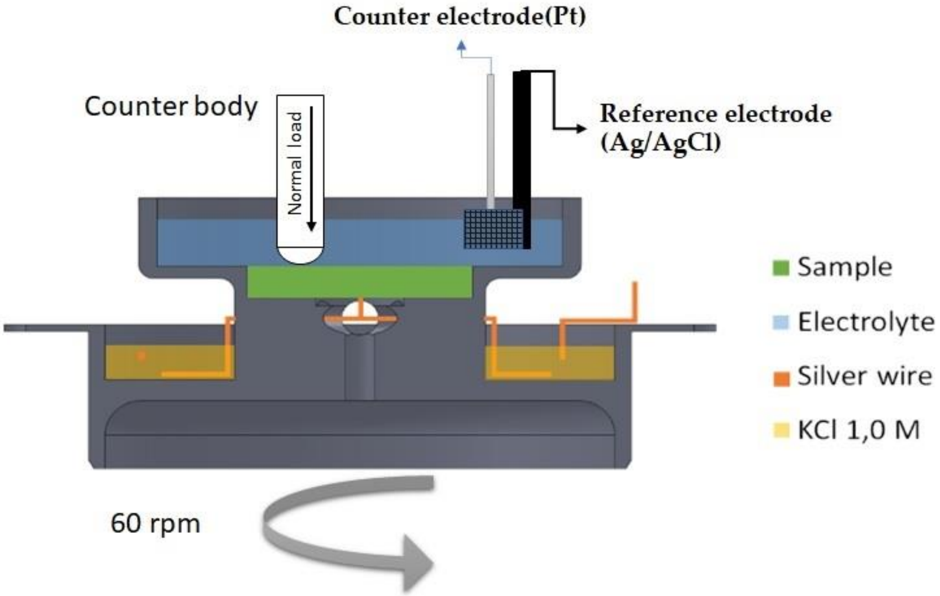

Figure i Schéma de la cellule de tribocorrosion et du montage expérimental

Figure i Schéma de la cellule de tribocorrosion et du montage expérimental

Etude des substrats.

L'usure mécanique, la corrosion et le processus de tribocorrosion des aciers utilisés comme substrats ont été analysés. Pour les tests tribologiques, un contre-corps en oxyde d'aluminium d'un diamètre de 12 mm a été utilisé. Lesdits tests ont été effectués à 1,5 N de charge normale, 0,02 m/s de vitesse (équivalent à 60rmp) et une distance parcourue de 72 m. D'autre part, les tests électrochimiques ont été réalisés à l'aide d'un potentiostat

PalmSens 4 dans une configuration à trois électrodes, avec une électrode de platine comme contre-électrode et une électrode argent/chlorure d'argent comme électrode de référence. Dans le cadre des mesures électrochimiques effectuées, le potentiel en circuit ouvert (OPC, acronyme en anglais) a été mesuré. De plus, pour estimer la résistance à la corrosion, des tests de spectroscopie d'impédance électrochimique (EIS, acronyme en anglais) ont été effectués dans un intervalle de 10^{5} Hz à 10^{-2} Hz et une amplitude de ± 10 mV vs le potentiel a circuit ouvert tandis que pour les essais de tribocorrosion, mesures électrochimiques et mécaniques ont été effectuées simultanément.

Les tests mécaniques sur acier ont révélé des quantités de matériau enlevé comparables avec respectivement 2,1x10^{-4} ±4,2x10^{-5} mm^{3} pour l’acier AISI D2 et 1,6x10^{-4} ±1,0x10^{-4} mm^{3} pour l’acier AISI 431. Les deux matériaux ont montré des traces d'usure avec un mélange de zones comportant du matériel accumulé et d'autres avec du matériel enlevé. Ces traces d'usure ont montré des lignes dans le sens de rotation (Figure ii). De plus des restes de matériau provenant de l'acier ont été trouvés dans la bille d’oxyde d'aluminium. La combinaison de ces résultats indique que l'usure s'est produite en raison d'un processus d'usure par abrasion.

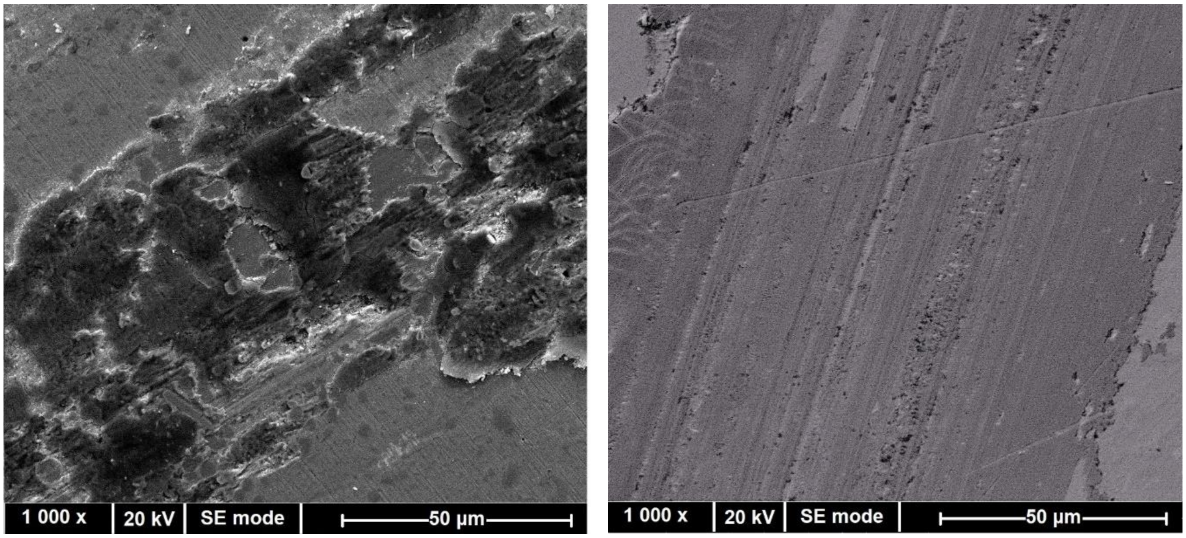

Figure ii Image de la trace d’usure sur acier AISI D2 et acier AISI 431 après le test 'pin on disc' à 1.5N de charge normale et à température ambiante et humidité ambiante.

Figure ii Image de la trace d’usure sur acier AISI D2 et acier AISI 431 après le test 'pin on disc' à 1.5N de charge normale et à température ambiante et humidité ambiante.

De plus, les tests électrochimiques (EIS) ont révélé qu'au contact de la solution d'acide citrique, l'acier AISI D2 se corrode avec une valeur de résistance spécifique de 3,3 ±0,1 $k\Omega cm^2$, tandis que l'acier AISI 431 est passivé avec une résistance à la corrosion de 160,6 ±5,0 $k\Omega cm^2$. Puisque l'acide citrique corrode l'acier AISI D2, la synergie dans le processus de tribocorrosion n'a pas pu être évaluée.

Afin d'évaluer le comportement de tribocorrosion de l'acier AISI 431, des mesures couplées de pin on disc et de EIS ont été effectuées. Deux tests différents ont été réalisés. Tout d'abord, des tests EIS ont été effectués sous glissement continu. Ces tests ont permis d'estimer la résistance à la corrosion du matériau sous usure active (la trace d'usure) et la quantité de matière arrachée. Les expériences de tribocorrosion ont été complétés par un test de pin on disc sous glissement latente, cela signifie que des cycles identiques successifs de glissement actif ont été effectués jusqu'à ce qu'une longueur de glissement totale de 72 m soit atteinte. La première partie du cycle correspond à l'usure mécanique active de la surface tandis que la seconde (latence) permet aux surfaces d'usure de se passiver.

Les tests de tribocorrosion sur glissement continu ont abouti à une résistance à la corrosion de la piste d'usure de 3,5 $k\Omega cm^2$ avec un volume d'usure de $4,1x10^{-3}$ $\pm 4,0x10^{-7}$ mm^3. Tandis que pour le test de latence le volume d'usure a été $2,8x10^{-3}$ $\pm 4,0x10^{-7}$ mm^3. Les valeurs trouvées sur le test électrochimique et le test de tribocorrosion ont été utilisées pour estimer les rapports K_c et K_m définies par [Celis and Ponthiaux 2012].

La valeur estimée de K_c était de 3,6 $x10^{-1}$, cette valeur représente un système où la contribution à la tribocorrosion, due à l'accélération de la corrosion induite par la destruction du film passif est faible par rapport à l'usure totale. De plus, K_m a été estimé à $3,0x10^{-3}$. Cette valeur montre que la formation du film passif accélère l'élimination mécanique du matériau. Par conséquent, lorsque le film passif a le temps de repousser, l'usure mécanique enlève une plus grande quantité de matière que lorsque le film passif n'est pas présent.

Synthèse du film de nitrure de tungstène

Des couches minces de nitrure de tungstène ont été déposées par pulvérisation cathodique RF. Les dépôts ont été effectués avec l'aide d'un Plassys MP300S dans un intervalle de puissance de 35 à 200 W et un intervalle de pression de 0,5 à 1,0 Pa, en utilisant une cible de tungstène à 99,99 % et un mélange d'argon (88%) et d'azote (12 %). Les revêtements ont été recuits à 500 °C dans une atmosphère d'azote. L'épaisseur du film mince était d'environ 1 μm.

La Figure iii présente le spectre survey de XPS, où parmi les échantillons obtenus à 1,0Pa et à différentes puissances de dépôt, de tels spectres montrent la présence d'oxygène, d'azote et du tungstène. De plus, des tests à différentes profondeurs d'une couche mince (0-160nm) ont montré que les pourcentages atomiques de chaque élément étaient similaires tout au long de la région testée. La moyenne des pourcentages atomiques trouvés était : 51,1 ± 3,5 % de W, 35,4 ± 3,4 % de O et 13,3 ± 2,1 % de N.

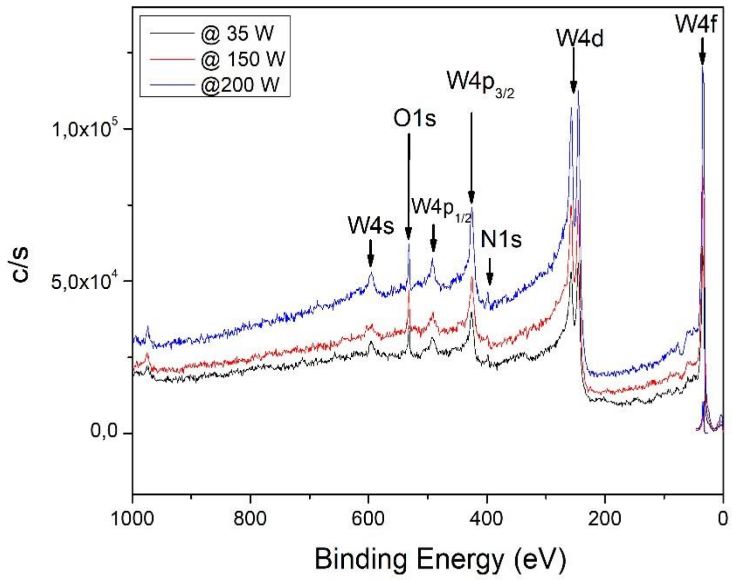

Figure iii Spectre de vue d'ensemble de XPS, où parmi les échantillons obtenus à 1,0Pa et à différentes puissances de dépôt

Des tests XRD ont été également effectués. De tels tests ont trouvé une combinaison de deux structures cristallines ; une structure fcc, comme celle du nitrure de tungstène et une monoclinique comme celle trouvée sur l'oxyde de tungstène (WO_3).

Les films déposés sur l'acier AISI D2 présentaient des problèmes d'adhésion récurrents, des expérimentations avec différents films tampons ont montré que les problèmes d'adhésion étaient dus à l'existence de petites zones riches en carbone à la surface de ce type d'acier. De plus, l'incompatibilité du film avec de grandes quantités de carbone a été confirmée en utilisant un film tampon de carbone, qui a produit un délaminage spontané du film mince de nitrure de tungstène.

Le Tableau i présente un résumé des résultats trouvés de volume d’usure et résistance à la corrosion pour chacun des films analysés. Des tests de pin on disc ont montré que le film mince diminue l'usure de surface sur les deux aciers.

En outre, la protection contre la corrosion donnée par des couches minces déposées sur l'acier AISI D2 est très faible en raison de problèmes de délaminage. Cependant, les revêtements obtenus sur acier AISI 431 ont montré une bonne résistance à la corrosion.

Tableau i Synthèse des résultats volume d’usure et de résistance à la corrosion des aciers AISI D2 et 431 nus et revêtus de nitrure de tungstène obtenus à différentes conditions de dépôt

Substrat	**Conditions de dépôt**		**Volume d'usure (mm^3)**	**Résistance à la corrosion ($k\Omega cm^2$)**
	Puissance (W)	Pression (Pa)		
AISI D2	35	1,0	$3{,}3 \times 10^{-5}$	3,9 ± 0,2
	150		$1{,}9 \times 10^{-5}$	7,6 ±0,6
	200		$1{,}9 \times 10^{-5}$	12,1 ±0,3
		0,7	$1{,}8 \times 10^{-5}$	10,1 ±0,3
		0,5	$2{,}4 \times 10^{-5}$	7,2 ± 0,5
	--	--	$2{,}1 \times 10^{-4}$	3,3 ± 1,0
AISI 431	---	---	$1{,}6 \times 10^{-4}$	160,6 ±5,0
	150	0,5	7.1×10^{-6}	207,0 ±22,0

Puisque l'acide citrique corrode aux couches minces déposées sur l’acier corrode, la synergie dans le processus de tribocorrosion n'a pas pu être évaluée.

La Figure iv montre des images SEM de l’acier AISI D2 et de l’acier AISI 431 recouverts avec une couche de nitrure de tungstène après le pin on disc test. Chaque image montre une partie de la piste d'usure où on peut observer une différence de contraste entre la trace d'usure et le reste du revêtement. La raison d'une telle disparité de contraste est une hauteur différente, la région la plus foncée (la piste d'usure) correspond à une partie plus profonde de l'échantillon confirmant que du matériau a été retiré. La piste d'usure présentait également des lignes dans le sens de la rotation et de l'accumulation de matériau indiquant l'usure par abrasion, cela a été confirmé lorsque le matériau de la piste d'usure était présent dans la bille d’oxyde d’aluminium.

Finalement, afin d'évaluer le comportement de tribocorrosion de la couche mince déposé sur l'acier AISI 431, des mesures couplées de pin on disc et de EIS ont été effectuées. Ces essais étaient les mêmes que ceux effectués sur l'acier nu.

Les tests de tribocorrosion sur glissement continue ont abouti à une résistance à la corrosion de la piste d'usure de 3,5 $k\Omega cm^2$ avec un volume d'usure de $5{,}1 x 10^{-4} \pm 4{,}0 x 10^{-7}$ mm^3, valeur était supérieure de deux ordres de grandeur à celle trouvée pour le même test en l'absence de l'électrolyte. Pour le test de latence le volume d'usure a été $7{,}0 x 10^{-4}$ $\pm 4{,}0 x 10^{-7}$ mm^3. Les valeurs trouvées dans le test électrochimique et le test de tribocorrosion ont été utilisées pour estimer les rapports K_c et K_m définies par [Celis and Ponthiaux 2012]

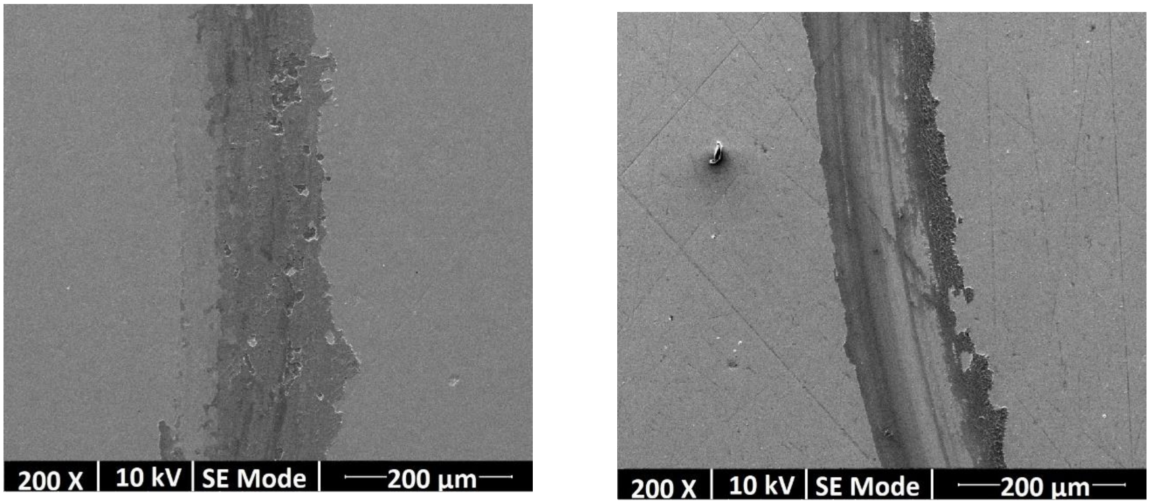

Figure iv Image de la trace d’usure sur nitrure de tungstène déposée a 150W and 0.5 Pa sur acier AISI D2 (à gauche) et acier AISI 431 (à droit) après le test 'pin on disc' à 1.5N de charge normale et à température ambiante et humidité ambiante.

Figure iv Image de la trace d’usure sur nitrure de tungstène déposée a 150W and 0.5 Pa sur acier AISI D2 (à gauche) et acier AISI 431 (à droit) après le test 'pin on disc' à 1.5N de charge normale et à température ambiante et humidité ambiante.

La valeur estimée de K_c était de $5{,}1 x 10^{-1}$, cette valeur montre que la contribution à la tribocorrosion, due à l'accélération de la corrosion induite par la destruction du film passif est faible par rapport à l'usure totale. De plus, K_m a été estimé à $6{,}1 x 10^{-3}$. Cette valeur montre que la formation du film passif accélère l'élimination mécanique du matériau. Par conséquent, lorsque le film passif a le temps de repousser, l'usure mécanique enlève une plus grande quantité de matière que lorsque le film passif n'est pas présent.

Le présent travail a abouti à l'adaptation du UTM-tribolab pour l'évaluation de la tribocorrosion par 'pin on disc'. De plus, des couches minces de nitrite de tungstène ont été déposées avec succès par pulvérisation cathodique rf. Cette couche mince s'est avérée être une option viable pour protéger des matériaux tels que l'acier AISI 431 contre la tribocorrosion. En revanche son utilisation comme film protecteur sur des matériaux à haute teneur en carbone tels que l'AISI D2 ne peut pas être validée, en raison de délaminations récurrentes qui exposent la surface du substrat.

Les résultats obtenus présentent une première approche à l'exploration de l'utilisation du nitrite de tungstène comme film résistant à la tribocorrosion. Il reste à explorer l'utilisation d'additifs dans le film pour améliorer l'usure survenue lors du processus de tribocorrosion ainsi qu'à étudier le comportement sur d'autres types de substrats ; sans oublier la recherche d'autres alternatives de films tampons pour éviter le délaminage lorsque le film est déposé sur des substrats riches en carbone.

Résumé

Le travail présenté ici a pour objet la synthèse de couches minces de nitrure de tungstène ainsi que l'étude de leurs propriétés par rapport à la tribocorrosion. La méthodologie utilisée comprend : (1) l'adaptation et l'optimisation du système de synthèse de couche minces (pulvérisation cathodique RF) et du système de mesure de la tribocorrosion, (2) la caractérisation électrochimique et tribologique des substrats (acier AISI 431 et acier AISI D2), (3) et la réalisation, l'optimisation et la caractérisation de couches minces de nitrure de tungstène et de leurs propriétés tribo-électrochimiques (tribocorrosion).

Le revêtement obtenu a amélioré la résistance à l'usure et à la corrosion des deux substrats. Néanmoins, seul pour le cas de l'AISI 431, la vitesse de corrosion s'est révélée suffisamment faible, le système est donc considéré comme passif et relativement plus résistant à la tribocorrosion. La meilleure réponse a été trouvée pour les revêtements obtenus à une puissance de dépôt élevée et à de faibles pressions de dépôt, suggérant qu'une densité plus élevée de la couche mince améliore ses réponses tribologiques et électrochimiques. Enfin la synergie entre l'usure mécanique et la corrosion de la couche mince de nitrure de tungstène a été évaluée. Avec un rapport K_c d'environ $5,1x10^{-1}$, l'accélération de la corrosion induite par l'usure mécanique est négligeable, et le rapport K_m de $6,14x10^{-3}$ suggère que l’usure mécanique est accélérée par la formation du film passif.

Les résultats obtenus présentent une première approche à l'exploration de l'utilisation du nitrite de tungstène comme couche mince résistant à la tribocorrosion. Ceci ouvre la porte à une étude plus approfondie et plus complète de ce type de couches minces comme couches protectrices contre la tribocorrosion en contact avec différents électrolytes.

Mots clés : tribocorrosion, pulvérisation cathodique, couches minces

Abstract

The present work is focused on the synthesis and tribocorrosion study of tungsten nitride as a tribocorrosion resistant thin film. The methodology used comprised: (1) the adaptation and optimization of the synthesis system (radio frequency magnetron sputtering) and the tribocorrosion evaluation system, (2) the electrochemical and tribological evaluation of the substrates (AISI 431 steel and AISI D2 steel) and (3) the synthesis, optimization and tribo-electrochemical (tribocorrosion) evaluation of the tungsten nitride thin film.

The obtained thin film improves the wear and corrosion resistance of both, AISI 431 steel and AISI D2 steel. Nevertheless, only for AISI 431 the corrosion speed is low enough to be considered as a passive system and a suitable tribocorrosion resistant system. The best response was found for the thin films obtained at high deposition power and low deposition pressures, suggesting that a higher film density enhance the tribological and electrochemical responses. Moreover, the tribocorrosion synergism between wear and corrosion of the tungsten nitride thin film was evaluated finding a K_c ratio of about $5.1x10^{-1}$, indicating that the corrosion acceleration induced by the mechanical wear is negligible, and a K_m ratio of $6.14x10^{-3}$, revealing that the mechanical material removal is accelerated by the formation of the passive film.

The obtained results represent an initial approach to the exploration of the tungsten nitrite thin film as a protective film against tribocorrosion. Such results open the path towards more extensive and comprehensive studies of such type of thin films as protection against tribocorrosion when in contact with different electrolytes.

Key words: tribocorrosion, sputtering, thin films